The Laser Cooling and Magneto-Optical Trapping of the YO Molecule

by

Mark Yeo

B.S., University of Michigan, 2006

A thesis submitted to the

Faculty of the Graduate School of the

University of Colorado in partial fulfillment

of the requirements for the degree of

Doctor of Philosophy

Department of Physics

2015

This thesis entitled:
The Laser Cooling and Magneto-Optical Trapping of the YO Molecule
written by Mark Yeo
has been approved for the Department of Physics

_____

Prof. Jun Ye

_____

Prof. Deborah S. Jin

Date _____

The final copy of this thesis has been examined by the signatories, and we find that both the content and the form meet acceptable presentation standards of scholarly work in the above mentioned discipline.

Yeo, Mark (Ph.D., Physics)

The Laser Cooling and Magneto-Optical Trapping of the YO Molecule

Thesis directed by Prof. Jun Ye

Laser cooling and magneto-optical trapping of neutral atoms has revolutionized the field of atomic physics by providing an elegant and efficient method to produce cold dense samples of ultracold atoms. Molecules, with their strong anisotropic dipolar interaction promises to unlock even richer phenomenon. However, due to their additional vibrational and rotational degrees of freedom, laser cooling techniques have only been extended to a small set of diatomic molecules.

In this thesis, we demonstrate the first magneto-optical trapping of a diatomic molecule using a quasi-cycling transition and an oscillating quadrupole magnetic field. The transverse temperature of a cryogenically produced YO beam was reduced from 25 mK to 10 mK via doppler cooling and further reduced to 2 mK with the addition of magneto-optical trapping forces.

The optical cycling in YO is complicated by the presence of an intermediate electronic state, as decays through this state lead to optical pumping into dark rotational states. Thus, we also demonstrate the mixing of rotational states in the ground electronic state using microwave radiation. This technique greatly enhances optical cycling, leading to a factor of 4 increase in the YO beam fluorescence and is used in conjunction with a frequency modulated and chirped continuous wave laser to longitudinally slow the YO beam. We generate YO molecules below 10 m/s that are directly loadable into a three-dimensional magneto-optical trap. This mixing technique provides an alternative to maintaining rotational closure and should extend laser cooling to a larger set of molecules.

Dedication

To Teow.

Acknowledgements

There are many people who made this work possible. First and foremost is Jun Ye for taking me on in his group and providing such a great science environment and providing support at every level.

I also had great team working on the YO experiment. Matt Hummon was the senior post-doc and has overseen the experiment from the empty optics table phase to what it is today. Yong Xia was instrumental in the initial building of the experiment. Alejandra Collopy, was instrumental in building up the 3D MOT apparatus. Bo Yan is a magician with the lasers. Also I must thank visiting students Max Kuhnert from TU Wien and Maurice Petzold from the University of Hanover. Also I would like to welcome Yewei Wu who has just joined the crew in recent months and with Alejandra, will take this experiment to dizzying heights.

This experiment was done in collaboration with John Doyle's group at Harvard University. Their group shared their expertise which let us build our own advanced cryogenic buffer gas beam source. Thanks to Boerge Hemmerling, Chae Eunmi, Garrett Drayna, Aakash Ravi, David Patterson, Hsin-I Lu and John Doyle for all their help and for letting me visit their lab..

In my time at JILA, I also spent time on the OH stark deceleration experiment and I must thank the great people I worked with on this project, Brian Sawyer, Benjamin Stuhl, Benjamin Lev, Dajun Wang, Hao Wu, David Reens and Timothy Langen.

The Ye group has been a great font of knowledge and great friendships, whether it is sharing equipment or more importantly sharing knowledge, I have never wanted in either

aspect from this great group. In particular I must thank Florian Adler and Kevin Cossell for their help in setting up the frequency comb. Thanks to everyone who provided great advice and letting me borrow stuff at various points.

I must also thank the great support staff here in JILA. Thanks to the great machinists, Hans Green, Todd Asnicar, Blaine Horner, Kim Hagen, David Alchenberger and Kels Detra. Thanks to the electronics shop staff, Terry Brown, Carl Sauer, Chris Ho, James Fung-A-Fat, Mike Whitmore and Paul Beckingham. Also, I must say thanks to JILA computing for maintaining our computer systems, especially J.R. Raith for fixing countless computers and being a great concert buddy.

I also want to thank Chris Monroe and the group at the University of Michigan (now at JQI), for giving me my first experience in cutting edge AMO research.

Outside of JILA, I made many friends but in particular I must shout out to the most aptly named band, Cryogen (please see Chapter 4) for the time I played in the band and for letting me be a member of the extended family. It was a great experience recording CDs and playing shows all over Colorado. Thanks go to Brian Sawyer (again) for recruiting me into the band and for inspiring my love for the more extreme side of metal. Ryan "Darkness" Conner, vocalist and recording extraordinaire. for making my drums sound like trapped thunder and all of my other bandmates, Mike Papajohn, Greg Burgess, Chris Gugglioti and Aaron Lande, my predecessor. The band is no more but I hope our legacy lives on.

Back in Singapore, my parents, Khee Leng and Margaret, raised me in an environment that always emphasized the importance of learning and gave me all the opportunities to pursue my dreams. Thanks to my brother Shaun for all the good times growing up wrestling and bowling and is himself graduating in a month.

Here in Colorado, my wife, Teow Lim Goh has been my rock from the very beginning, thank you for all the support and understanding. Also thanks to my two personal assistant cats, Gingertoes and DaFuzz.

Contents

Chapter

Tables

Table

Figures

Figure

Chapter 1

Introduction

Laser cooling and trapping is one of the great cornerstones of modern atomic physics. These techniques have facilitated the efficient creation of cold and dense samples of atoms [1] and have been extended to about twenty atomic species. This abundance of species makes ultracold atomic systems a powerful tool for studying various phenomena, from quantum-degenerate gases [2, 3], physics beyond the Standard Model [4], and strongly correlated systems [5], to applications in quantum information [6, 7] and simulation [8, 9], quantum sensing [10], and ultraprecise optical clocks [11, 12].

Polar molecules have additional features over atoms, most notably the permanent body-fixed electric dipole moment. This leads to a range of tantalizing applications that have motivated the demonstration of several cold and ultracold molecular production techniques.

1.1 Why polar molecules

Polar molecules possess a strong anisotropic interaction potential due to their body fixed electric-dipole moment. This leads to the possibility of controlling collision dynamics [13, 14] and cold and ultracold chemical reaction rates [15–17]. Electric field controllable cross sections have been shown in collisions between magnetically trapped OH with 5 K ND_3 molecules [18]. Here, a 40% increase in collision cross section was observed upon the application of an electric field large enough to polarize both species. In addition, the inelastic collision cross section for magnetically trapped OH was shown to exhibit a quadratic dependence

on their effective dipole moment [19]. Also, experiments in the ultracold KRb have shown electric field controllable chemical reaction rates in the single partial wave regime [20, 21].

Cold molecules have found great utility in precision measurements. Due to the enormous internal electric fields in heavy polar molecules on the order of 100 GV/cm, huge enhancements in constraining the electron electric dipole moment can be gained [22, 23]. This has been exploited to improve measurements of the electron electric dipole moment in ThO [24] and YbF [25] and have placed further constraints on physics beyond the Standard Model. In addition, the rich internal structure of molecules promises improvements in measurements of physical constants such as the proton to electron mass ratio and time variations of the fine-structure constant [26–28].

Due to the dipolar interaction, polar molecules have been identified as potential qubits [29–31] and promise to give rise to novel many-body quantum systems and to further advance condensed matter simulations. [32, 33]

1.2 Molecule production techniques

The techniques used to generate cold and ultracold molecules are generally separated into "indirect" and "direct" methods [34]. Indirect methods have come to mean the assembly of pre-cooled atoms into molecules using the methods of photoassociation [35,36] or magneto-association via a Feshbach resonance [37]. To date the ^{40}K^{89}Rb samples formed by magneto-association and stimulated Raman adiabatic passage (STIRAP) [37,38] is the only such polar molecular with sub μK temperatures. However, there has been much effort to extend these techniques to other molecules including RbCs [39, 40], NaK [41], LiCs [42], LiYb [43, 44] and NaCs [45]. A clear limitation to this class of methods is that the constituent atoms are limited to readily laser cooled ones, thus limiting the chemical diversity of the molecules.

The so called direct methods take preexisting molecules and cool them down. Such molecules can be initially produced via photodissociation, electric arc discharge, laser ablation or even straight out of a gas bottle. The first step involves forming a molecular beam for

which two methods have gained prominence. The first is the supersonic expansion [46, 47], where the internal degrees of freedom of the molecule are cooled at the expense of a high forward velocity (several 100 m/s). The second is buffer gas cooling [48], which was refined in the Doyle group in Harvard [49]. Here, the molecule species is thermalized via a helium buffer gas to a cold cell at a temperature on the order of 1 K. Beams with velocities of 50-200 m/s, depending on source configuration [49], are routinely produced.

One of the most prominent techniques to further slow these beams is Stark deceleration [46, 50]. Weak electric field seeking molecules ride up a potential hill generated from a pair of electrodes. Fields are switched off before the molecules cross the other side of the hill, which removes kinetic energy. In addition to crossed beam experiments [51], this technique can decelerate molecules all the way to rest and can therefore be used to load conservative traps [50]. Zeeman deceleration using switched magnetic fields have also been demonstrated [52, 53]. Such systems have been used to load conservative traps, and have been used to probe both atom-molecule and atom-atom collisions [18, 50, 54–56] as well as measuring diatomic molecular properties [57, 58].

These deceleration and trapping techniques are conservative implying that phase space density cannot be increased. However, recent work, using the rf evaporation of OH [59, 60] has shown evidence of increasing the phase space density by several orders of magnitude. In addition, the polyatomic CH_3F molecule was cooled down to 29 mK using a Sisyphus-type cooling scheme on a vibrational transition [61, 62].

1.3 Laser cooling of molecules

Extending laser cooling to polar molecules was known to be very difficult due to the plethora of dark rovibrational branching paths that would stop the required optical cycling [63]. While there was some initial optimism in the idea of cavity-mediated laser cooling [64], where the Purcell effect [65] would enhance the coherent Rayleigh scattering for only the cooling transitions, it turned out that collective effects were also required to ensure

optical cycling [66], this however requires a prohibitively high initial phase space density to initiate and therefore still remains a dream.

However, it turns out that there is a way to free-space laser cool polar molecules. Di Rosa was able to identify several laser cooling candidates,for example CaH, based on their very diagonal vibrational branching [67]. A theoretical proposal in our group using a so called Type II MOT transition [68] further showed the way for the closure of rotational branching. This technique uses a transition whose total angular momentum J in the ground state is larger than in the excited state, i.e. $J'' \rightarrow J' = J'' - 1$, which is the opposite of typical atomic laser cooling transitions [1]. This eliminates rotational branching because the electric dipole selection rule, $\Delta J = \pm 1$ will only allow decays back to the original rotational state. This idea inspired the DeMille group at Yale to perform the first demonstration of optical cycling [69] and doppler cooling [70] of a polar molecule, SrF. The first magneto-optical trap was demonstrated on the YO molecule in our group [71] on a beam of YO. The full realization of a full three dimensional MOT for SrF was realized very recently in [72] and a further improvement on the SrF MOT, based on a MOT beam polarization scheme derived from a detailed calculation by Mike Tarbutt [73] was realized [74].

In addition, the advent of optical cycling in polar molecules allows for radiation pressure slowing in molecules which was demonstrated in Hind's group at Imperial college which slowed the longidtudinal velocity of CaF by 30 m/s [75]. For SrF, broadband laser radiation was used to slow molecules to be loaded directly into a 3D MOT [72].

1.4 Why YO?

The Yttrium Monoxide (YO) molecule was chosen for several reasons. The $X^2\Sigma^+ \rightarrow A^2\Pi_{1/2}$ transition is strong, with a linewidth of $\Gamma = 2\pi \times 4.8 \times 10^6$ MHz. YO also has very diagonal vibrational branching, such that addressing the 3 lowest vibrational levels allows for more than 10^6 photon scatters, which is sufficient for demonstrating MOT action. The electronic structure is also favorable for shutting down rotational branching as described

above.

In addition, as YO has been detected in main sequence stars including the sun [76, 77], much of its molecular structure is well characterized [77–88]. YO has an intermediate electronic state between the two states used for optical cycling. In this thesis we found a method to circumvent the losses due to branching through this state [89] but this intermediate state may also be used to create a narrow line MOT, which could lead to temperatures 100 times smaller than previously observed [90] in laser cooled molecules.

The remainder of the thesis is structured as follows: In Chapter 2 we will describe the salient molecular structure for the laser cooling of YO. Chapter 3 describes the various laser systems used to address the complicated YO structure, and the stabilization scheme to a self referenced frequency comb. Chapter 4 describes the 2 stage cryogenic buffer gas YO beam source that was developed in collaboration with the Doyle group at Harvard University. In Chapter 5 we present the first magneto-optical trap (MOT) for a molecule [71]. Here, the YO beam is doppler cooled and confined transversely by MOT forces. Chapter 6 demonstrates the microwave mixing of rotational states in the electronic ground state. This technique addresses losses to dark rotational states due to decays through the intermediate $A'^2\Delta_{3/2}$ state and allows us to radiation pressure slow YO to 10 m/s, which is loadable into a 3D MOT [89]. The microwave mixing presents an alternative method to close off rotational branching and opens the door to the laser cooling and trapping of a larger set of molecules. Chapter 7 discusses the next technical steps to demonstrating a 3D MOT in YO as as well as discussing the prospects for the narrow-line MOT.

Chapter 2

YO molecular structure

In this chapter, we will present some general concepts in diatomic molecular structure and specify this for the YO molecule. We begin with the relevant Hund's angular momentum coupling cases for the three electronic states for YO that are engaged in the optical cycling. We will then derive the hyperfine structure in the ground state of YO as well as its Zeeman structure. Then we will calculate the vibrational structure and show how this is favourable for laser cooling. With these pieces in place, we describe the method by which rotational closure is maintained during the optical cycling. Finally we present branching ratio calculations for various transitions that which will be used in later chapters.

2.1 Angular Momentum Coupling

Diatomic molecules with their rotational degrees of freedom have far more complicated angular momentum structure than atomic species. In addition, the internuclear axis breaks the spherical symmetry and thus the good quantum numbers are different from that of atoms. To help understand this mess of angular momenta coupling, Friedrich Hund came up with idealized angular coupling schemes [91] now known as the Hund's coupling cases. We will present the two most common coupling cases, which also describe the states of the YO molecule that are encountered during optical cycling.

2.1.1 Case (a)

In Hund's case (a), the electron orbital angular momentum **L** is strongly coupled to the internuclear axis as shown in Fig. 2.1. The electron spin **S** is in turn strongly coupled to **L** via spin-orbit coupling. Their projection onto the internuclear axis are denoted as Λ and Σ and the sum of these two components is denoted as Ω. The rotation of the nuclei is denoted by the vector **R** and couples to $\mathbf{\Omega}$ to form the total angular momentum **J**.

As **L** may precess about the internuclear axis in a clockwise or anti-clockwise sense, the projection can take on values of $\pm\Lambda$. This leads to a two-fold degeneracy for a given value of $|\Omega|$ that is known as Λ-type doubling and this degeneracy is lifted due to molecular rotation. The good quantum numbers for a case (a) state can be summed in ket notation as

$$|\eta, \Lambda; S, \Sigma; J, \Omega, M_J\rangle \tag{2.1}$$

where η denotes the electronic, vibrational or any other quantum number required to define the molecular state, M_J is the projection of **J** on some space fixed axis and is used when considering the effects of external fields on the molecule.

The rotational energy is given by

$$H_{rot} = B\mathbf{R}^2 = B(\mathbf{J} - \mathbf{L} - \mathbf{S})^2 \tag{2.2}$$

where B is the rotational constant.

We note that case (a) is a good approximation for states where the spin-orbit coupling is much larger than the rotational energy, i.e. $\gamma_{SO}\Lambda \gg BJ$ where γ_{SO} is the spin-orbit coupling constant. The relative rotational energies to first order have the form

$$E_{rot} = BJ(J+1) \tag{2.3}$$

where B can expressed as

$$B = \frac{\hbar^2}{2\mu R_{nuc}^2} \tag{2.4}$$

where R_{nuc} is the internuclear separation and μ is the reduced mass given by

$$\mu = \frac{m_1 m_2}{m_1 + m_2} \tag{2.5}$$

and m_1 and m_2 are the masses of the two nuclei. For a given electronic state, the lowest rotational level has $J = \Omega$.

States that are well approximated in this coupling scheme are labelled as $^{2S+1}\Lambda_{|\Omega|}$ where the value of Λ is denoted by the Greek letters Σ, Π, Δ, Φ... for $|\Lambda| = 0, 1, 2, 3....$ Note that there is an unfortunate naming degeneracy between the electron spin projection quantum number and $|\Lambda| = 0$ but the context should always make it clear which is which.

2.1.2 Case (b)

Hund's case (b) occurs most often when $\Lambda = 0$. In such a case, $\mathbf{S}$ is not coupled to the internuclear axis as spin-orbit coupling is zero. In some light molecules, for $\Lambda \neq 0$ the spin-orbit coupling is sufficiently weak that $\mathbf{S}$ is not coupled to the internuclear axis and such cases are also appropriately described by this coupling scheme. The angular momenta couple as follows, $\mathbf{\Lambda}$ couples to $\mathbf{R}$ to form $\mathbf{N}$. For $\Lambda = 0$ (which is indeed the case for ground state of YO), $\mathbf{N}$ and $\mathbf{R}$ are equivalent and as such the former can be correctly referred as the rotational angular momentum. $\mathbf{N}$ then couples to $\mathbf{S}$ to form $\mathbf{J}$, the total angular momentum. Basis functions are written as

$$|\eta, \Lambda; N, S; J, M_J\rangle \tag{2.6}$$

and the rotational Hamiltonian is given by

$$H_{rot} = B\mathbf{R}^2 = B(\mathbf{N} - \mathbf{L})^2. \tag{2.7}$$

Relative rotational energies are given by

$$E_{rot} = BN(N + 1) \tag{2.8}$$

States with $\Lambda = 0$ are denoted by the spectroscopic symbol $^{2S+1}\Sigma^{\pm}$ where $\pm$ denotes the parity of rotational states with even N with the parity alternating with each successive rotational level.

Additional Hund's cases, i.e. (c)-(e) coupling cases are presented in section of Brown and Carrington [92], and in [91] but are outside the scope of this work.

2.2 Electronic Structure

The YO molecule has one abundant naturally occurring isotopologue, $^{89}Y^{16}O$ and has three electronic states of interest, the ground $X^2\Sigma^+$ state, the excited $A^2\Pi_{1/2}$ state and the metastable intermediate state $A'^2\Delta_{3/2}$. For the ground state, $\Lambda = 0$ hence it is well described with the Hund's case (b) coupling scheme. Rotational states with even (odd) N have even (odd) parity.

The $A^2\Pi_{1/2}$ ($|\Lambda| = 1|$) and $A'^2\Delta_{3/2}$ ($|\Lambda| = 2|$) are good Hund's case (a) states. The quasi-cycling laser transition occurs between the lowest vibrational levels of the $X^2\Sigma^+$ and $A^2\Pi_{1/2}$ states where the transition energy is 488.492 THz or 614 nm. The radiative lifetime of the $A^2\Pi_{1/2}$ state is $\gamma^{-1} = 33$ ns [93], which allows for fast optical cycling. As we shall see in chapter 6, on out of every ≈3000 optical cycles, the molecule falls into the $A'^2\Delta_{3/2}$ intermediate state and removes itself from the optical cycling, which is a most undesirable outcome. In chapter 6, we will describe how to avoid this loss via microwave rotation state remixing.

While the ground state is a Hund's case (b), it is a pathological case because its hyperfine splitting is much larger than the spin rotation coupling. We will treat this in the following section.

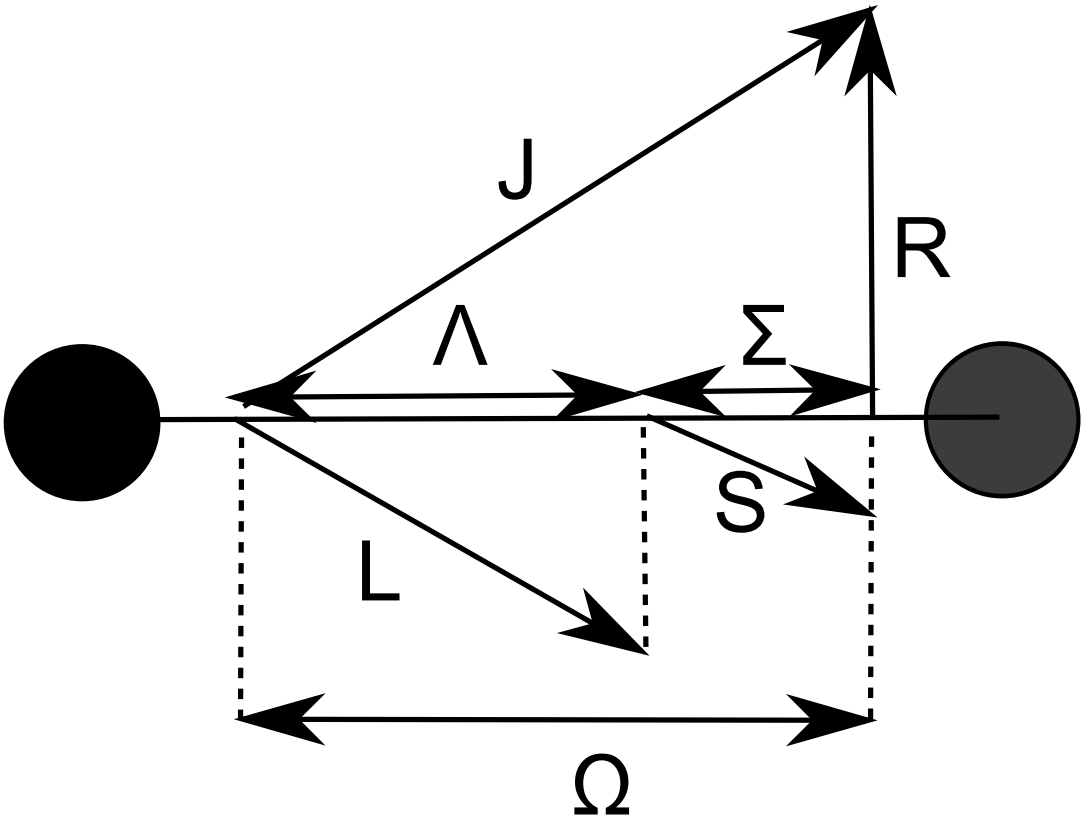

Figure 2.1: Angular momentum coupling diagram for Hund's case (a)

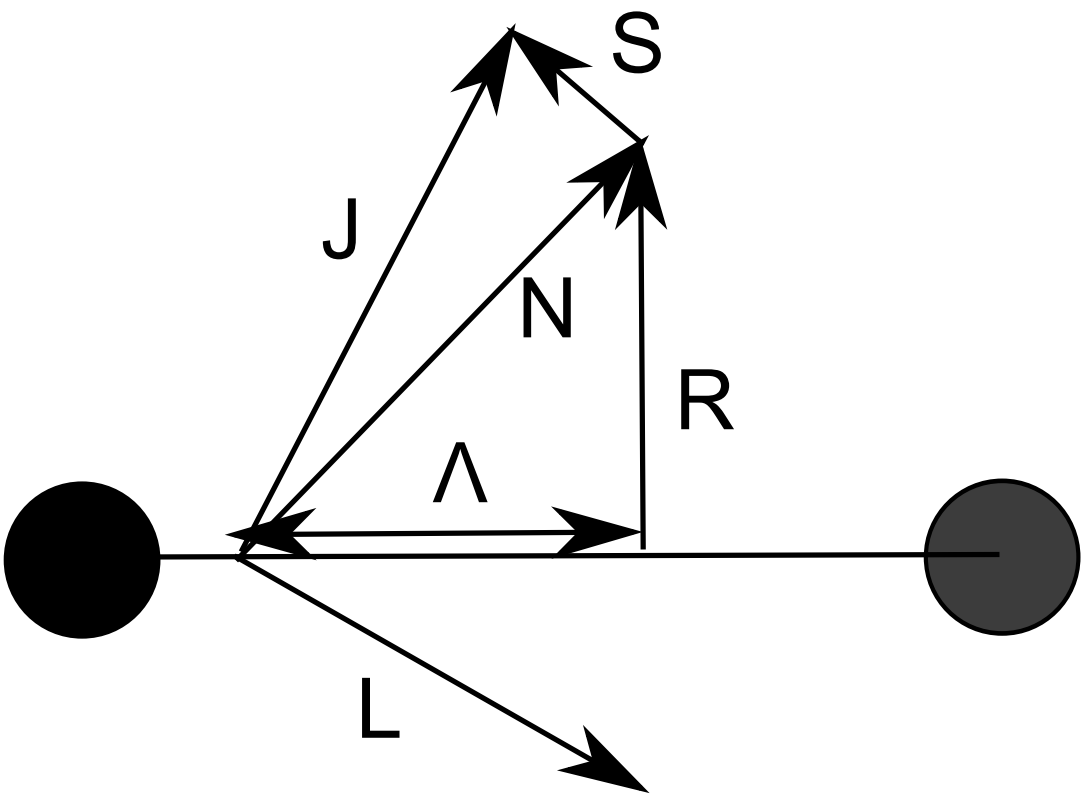

Figure 2.2: Angular momentum coupling diagram for Hund's case (b)

2.3 Hyperfine and Zeeman structure of the ground state

The Frosch-Foley effective Hamiltonian [94] for the YO ground state is given by

$$H_{ds} = B\mathbf{N^2} - D\mathbf{N^4} + \gamma_{SO}\mathbf{S}\cdot\mathbf{N} + b\mathbf{I}\cdot\mathbf{S} + cI_zS_z + C_I\mathbf{I}\cdot\mathbf{N} \tag{2.9}$$

where B is the rotational constant, D is the centrifugal distortion constant, γ_{SO} is the spin-rotation coupling constant, and C_I the nuclear spin rotation term. The constants b and c are related to the electron-nuclear dipole and Fermi contact interactions and will be discussed in further detail shortly. The numerical values of these constants are tabulated in Table 2.1

Parameter	v = 0	v = 1	v = 2	v = 3	v = 4
B [GHz]	11.6336(2)	11.5818(3)	11.5302(4)	11.4782(5)	11.4258(5)
D [kHz]	9.581(15)	9.533(54)	9.69(13)	9.71(15)	9.67(15)
γ_0 [MHz]	−9.2254(1)	−7.8465(1)	−6.3256(1)	−4.9905(3)	−3.514
b_0 [MHz]	−762.976(2)	−763.054(2)	−763.104(2)	−763.118(4)	
c [MHz]	−28.236(5)	−28.349(2)	−28.461(5)	−28.586(8)	
C_I [MHz]	$2.57(3)\times10^{-3}$	$2.30(3)\times10^{-3}$	$1.83(7)\times10^{-3}$		
γ_1 [MHz]	$1.7738(5)\times10^{-4}$	$1.8288(4)\times10^{-4}$	$1.8858(7)\times10^{-4}$	$1.946(5)*10^{-4}$	
b_1 [MHz]	$-3.09(5)\times10^{-5}$	$-2.76(4)*10^{-5}$	$-2.34(5)\times10^{-5}$		
γ_2 [MHz]	$5.96(6)\times10^{-10}$	$6.07(6)\times10^{-10}$	$6.49(8)\times10^{-10}$		

Table 2.1: Rotational [81]and hyperfine constants [95] for the $X^2\Sigma^+$ state of YO.

The rotational energy levels are given by

$$E_{rot} = BN(N+1) - D(N(N+1))^2. \tag{2.10}$$

Note that this includes the small centrifugal distortion. The spin-rotation (γ_{SO}) and the

$\mathbf{I} \cdot \mathbf{S}$ term b do also have small rotational dependence given by

$$\gamma_{SO} = \gamma_0 + \gamma_1 N(N+1) + \gamma_2 N^2 (N+1)^2 \tag{2.11}$$

$$b = b_0 + b_1 N(N+1) \tag{2.12}$$

$$\tag{2.13}$$

To interpret the meaning of the coupling terms b and c, Brown and Carrington [92] gives the following expressions

$$\begin{aligned} b &= g_S \mu_B g_N \mu_N (\mu_0/4\pi) \Big(\frac{8\pi}{3} \langle \eta, \Lambda | \, \delta(\mathbf{r}) \, | \eta, \Lambda \rangle - \frac{1}{2} \langle \eta, \Lambda | \, 3(\cos^2\theta - 1) \, | \eta, \Lambda \rangle \Big) \\ c &= g_S \mu_B g_N \mu_N (\mu_0/4\pi) \frac{3}{2} \langle \eta, \Lambda | \, 3(\cos^2\theta - 1) \, | \eta, \Lambda \rangle \, . \end{aligned} \tag{2.14}$$

here $g_s = 2.0023$ is the absolute value of the electron g-factor, μ_B is the Bohr magneton, g_N and μ_N are the nuclear g-factor and nuclear magneton respectively and θ is the relative angle between the nuclear and electron spins. We thus see that c is proportional to the electron-nuclear dipolar interaction and b is a linear combination of c and the Fermi contact interaction. Thus, we define two new parameters: b_F, the Fermi contact term and t, the axial dipolar hyperfine term as

$$b_F = b + \frac{c}{3} \tag{2.15}$$

$$t = \frac{c}{3} \tag{2.16}$$

The effective Hamiltonian can now be rewritten in tensor notation as

$$H_{eff} = \gamma_{SO} \mathbf{S} \cdot \mathbf{N} + b_F T^1(\mathbf{I}) \cdot T^1(\mathbf{S}) - \sqrt{30} t T^2(\mathbf{C}) \cdot T^2(\mathbf{S}, \mathbf{I}) \tag{2.17}$$

While a "typical" Hund's case (b) case molecule first couples $\mathbf{S}$ and $\mathbf{N}$ to form $\mathbf{J}$ via spin orbit coupling, our $X^2\Sigma^+$ state has an unusual angular momentum coupling scheme due to the large Fermi contact interaction. First, $\mathbf{I}$ and $\mathbf{S}$ couple to form the angular momentum $\mathbf{G}$. Then $\mathbf{G}$ couples with $\mathbf{N}$ to form the total angular momentum $\mathbf{F}$. The angular momentum states are written as $|((I,S)G,N)F\rangle$ and this is known as the $b_{\beta S}$ basis.

Section 10.3.1 pages 745-749 of [92] gives the matrix elements for each of the terms of the Hamiltonian. The electron spin-rotation is given by

$$\begin{aligned}
&\langle I,S,G,N,F,M_F|\,\gamma_{SO}\mathrm{T}^1(\boldsymbol{S})\cdot\mathrm{T}^1(\boldsymbol{N})\,|I',S',G',N',F',M_F'\rangle\\
=&\gamma_{SO}\delta(F,F')\delta(M_F,M_F')\delta(N,N')\\
&(-1)^{G'+F+N}((2G'+1)(2G+1))^{1/2}\begin{Bmatrix} N' & G' & F\\ G & N & 1\end{Bmatrix}\\
&(-1)^{G+I+1+S}\begin{Bmatrix} G & S & I\\ S & G' & 1\end{Bmatrix}(S(S+1)(2S+1)N(N+1)(2N+1))^{1/2}
\end{aligned}\tag{2.18}$$

the Fermi-contact interaction is independent of N

$$\begin{aligned}
&\langle I,S,G,N,F,M_F|\,b_F\mathrm{T}^1(\boldsymbol{I})\cdot\mathrm{T}^1(\boldsymbol{S})\,|I',S',G',N',F',M_F'\rangle\\
=&b_F(-1)^{I+G+S}\begin{Bmatrix} S & I & G\\ I & S & 1\end{Bmatrix}(I(I+1)(2I+1)S(S+1)(2S+1))^{1/2}
\end{aligned}\tag{2.19}$$

and the most complicated term, the Dipolar Hyperfine Interaction,

$$\begin{aligned}
&\langle I,S,G,N,F,M_F|\,\sqrt{6}g_s\mu_B g_N\mu_N(\mu_0/4\pi)\mathrm{T}^2(\boldsymbol{S},\boldsymbol{I})\cdot\mathrm{T}^2(\mathbf{C})\,|I',S',G',N',F',M_F'\rangle\\
=&t\sqrt{30}\delta(F,F')\delta M_F,M_F'\\
&(-1)^{G'+F+N}\begin{Bmatrix} N' & G' & F\\ G & N & 2\end{Bmatrix}\\
&\left((2G'+1)(2G+1)I(I+1)(2I+1)S(S+1)(2S+1)\right)^{1/2}\\
&\begin{Bmatrix} G & G' & 2\\ I & I & 1\\ S & S & 1\end{Bmatrix}(-1)^N\left((2N+1)(2N'+1)\right)^{1/2}\begin{pmatrix} N & 2 & N'\\ 0 & 0 & 0\end{pmatrix}
\end{aligned}\tag{2.20}$$

In zero field and ignoring matrix elements off diagonal in N, we obtain the reduced Hamiltonian for each rotational state.

	(G', F')			
(G, F)	$(1, N+1)$	(1, N)	(0, N)	(1,N-1)
(1, N+1)	$\frac{\gamma_{SO}N}{2} + \frac{b_F}{4} - t\frac{N}{4N+6}$	0	0	0
(1, N)	0	$-\frac{\gamma_{SO}}{2} + \frac{b_F}{4} + \frac{t}{2}$	$\frac{\gamma_{SO}}{2}\sqrt{N(N+1)}$	0
(0, N)	0	$\frac{\gamma_{SO}}{2}\sqrt{N(N+1)}$	$-\frac{3b_F}{4}$	0
(1, N-1)	0	0	0	$-\frac{\gamma_{SO}(N+1)}{2} + \frac{b_F}{4} - t\frac{N+1}{4N-2}$

Diagonalizing Equation 2.17, we obtain the hyperfine structure for $N = 0, 1, 2$ as depicted in Fig. 2.3. The large Fermi contact interaction, b_F, creates a ∼760 MHz splitting between the $G = 0, 1$ states. For $N > 0$, the coupling of N with G further splits the $G = 1$ state into states with total angular momentum $F = G \pm 1$.

To calculate the Zeeman structure, we add the following Hamiltonian to Equation. 2.17 by only consider the coupling of electron spin $\boldsymbol{S}$ to the magnetic field B_z (see Brown and Carrington [92] sections 9.5 and 5.5.4).

$$
\begin{aligned}
H_{Zeeman} =& \langle((I,S)G,N),F,m_F|\, g_S\mu_B B_z T^1_0(\boldsymbol{S})\,|((I,S)G',N),F',m'_F\rangle \\
=& g_S\mu_B B_z(-1)^{F-m_F}
\begin{pmatrix} F & 1 & F' \\ -m_F & 0 & m'_F \end{pmatrix} \\
& (-1)^{F+N+1+G}
\begin{Bmatrix} G' & F' & N \\ F & G & 1 \end{Bmatrix} \\
& (-1)^{G+I+1+S}
\begin{Bmatrix} S & G' & I \\ G & S & 1 \end{Bmatrix} \\
& (S(S+1)(2S+1)(2G'+1)(2G+1)(2F'+1)(2F+1))^{1/2}
\end{aligned}
\tag{2.21}
$$

We thus obtain the Zeeman structure as shown in Figure 2.4. A salient feature of the Zeeman spectrum is that at low fields, the energy splitting for the $G = 0$ states is almost zero, for example, at a magnetic field of 1 G the Zeeman splitting between the $m_F = \pm 1$ states is

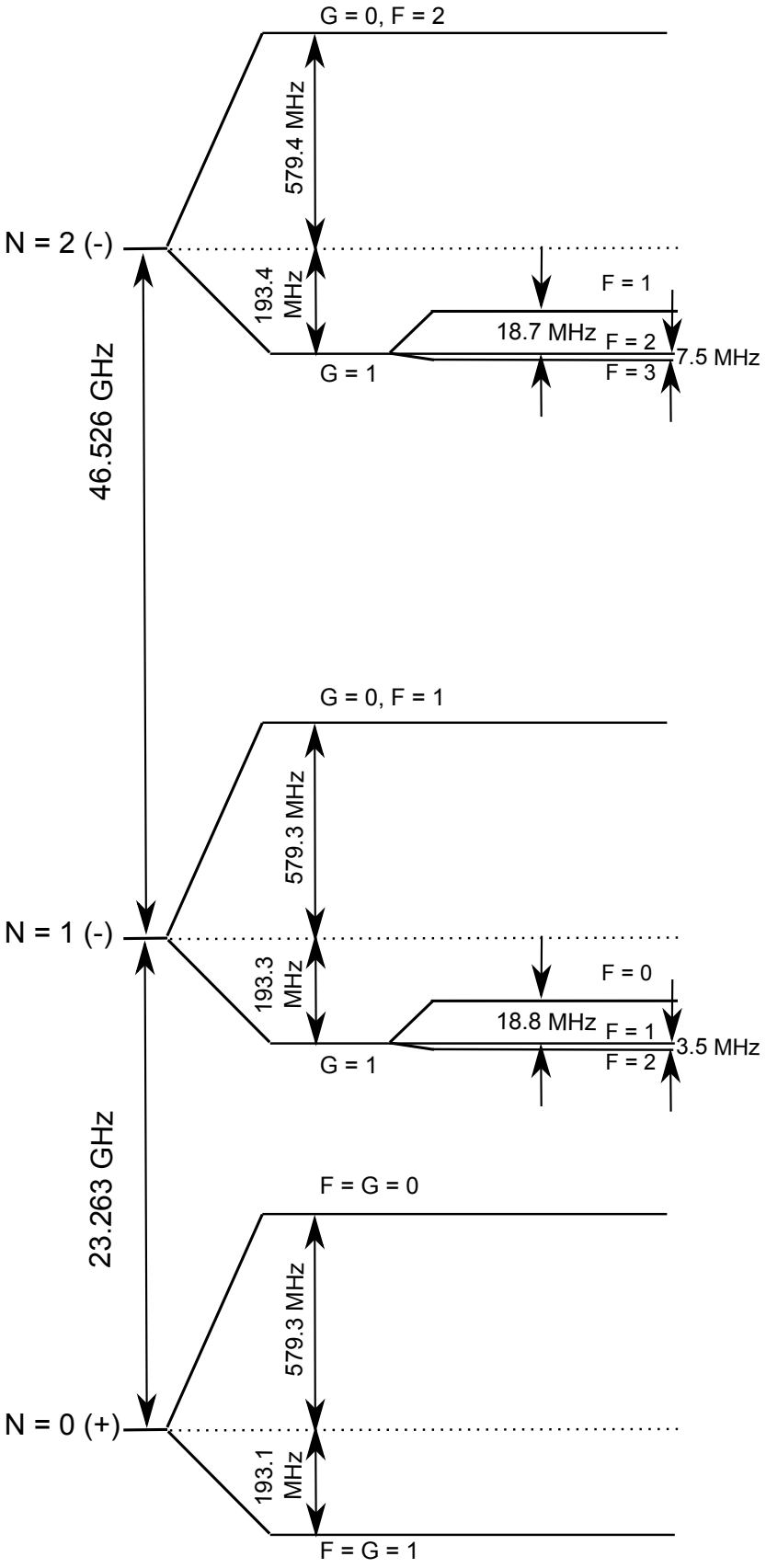

Figure 2.3: Hyperfine structure of the $^2\Sigma_{1/2}$ state of YO.

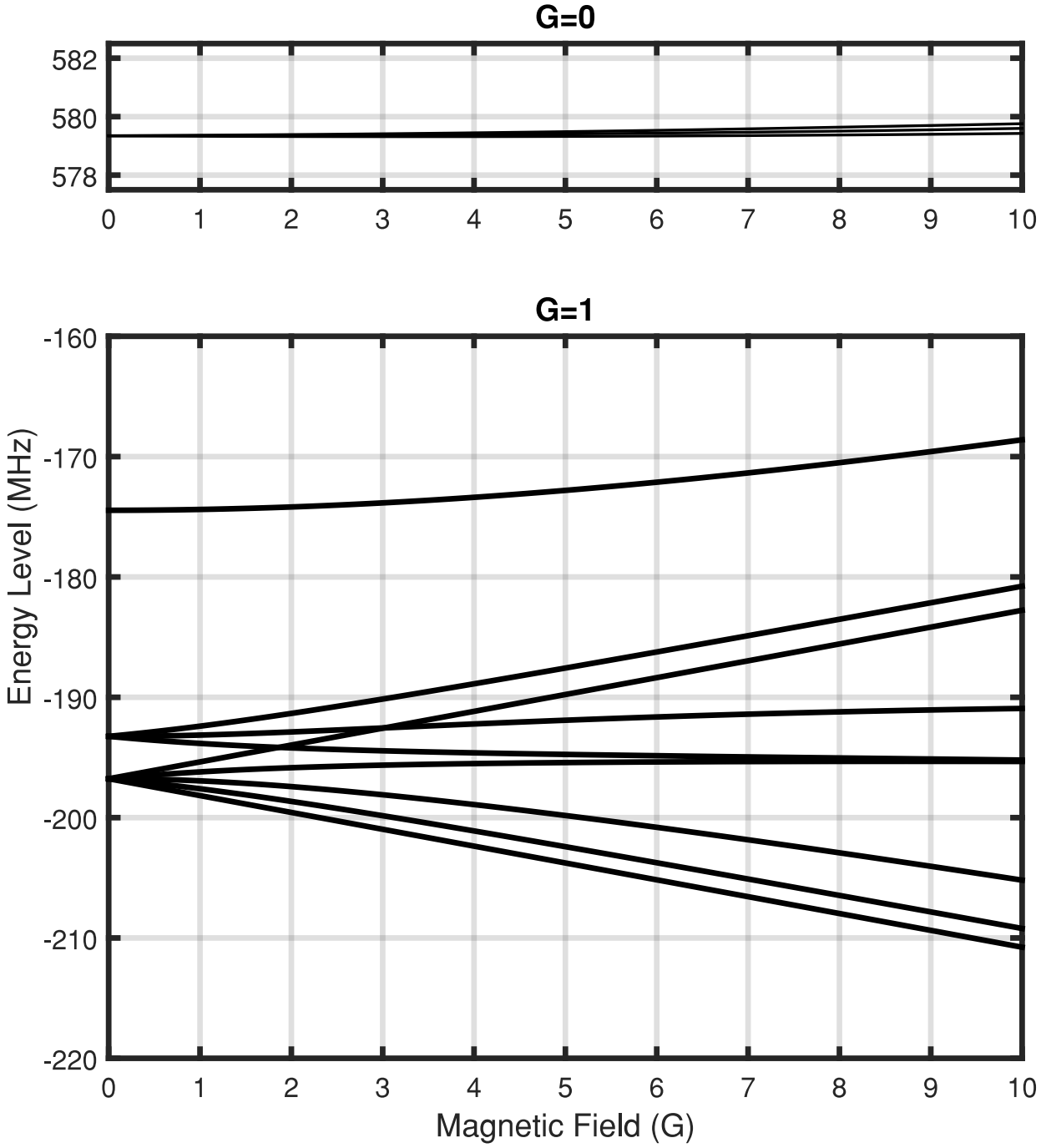

Figure 2.4: Zeeman structure of the $X^2\Sigma^+, N = 1$ state of YO.

≈30 kHz. Because of this low Larmor frequency, using an off-axis magnetic field to remix the Zeeman sub-levels [69] becomes dreadfully slow and would limit the maximum optical cycling rate. We will discuss how we address this issue in Chapter 5.

For the G = 1 states, from Equation 2.21 we can calculate the low-field effective magnetic moment to be $\frac{g_s}{4}\mu_B m_F$. This a good approximation for magnetic fields up to 2 G. This is when the Zeeman interaction energies become roughly comparable to the spin rotation (γ_{SO}) and the dipolar interaction (t). From 10 to 50 G, the Zeeman shift is again close to linear and can be approximated with an effective moment of $\frac{g_s}{2}\mu_B m_G$ where m_G is the projection of **G** on the lab frame. Finally, the third linear regime occurs when the Zeeman interaction becomes much larger than the Fermi contact b_F, i.e for fields greater than 1000 G. The effective magnetic moment is that of the unpaired electron and reverts to the familiar form of $g_s m_s$ where m_s is the lab projection of the electron spin. It is in this regime where the $G = 0$ state finally picks up an appreciable Zeeman shift. While we never subject YO molecules to such strong fields in this work, this regime can be of importance if we were to attempt magnetic guiding.

2.4 Hyperfine and Zeeman Structure of the $A^2\Pi_{1/2}$ state.

The state that we excite to in our optical cycling transition is the $A^2\Pi_{1/2}, J = 1/2$ state. It is a Hund's case (a) state with $|\Lambda| = 1$, $|\Sigma| = 1/2$ and $|\Omega| = \frac{1}{2}$. The lowest rotational state has $J = |\Omega| = \frac{1}{2}$. **J** combines with nuclear spin **I** to form the total angular momentum **F**. F can take on values of 0 or 1 but is spectroscopically unresolved. In zero field, the state is split into two parity states via Λ- type doubling. Mulliken and Christy's Λ-doubling p and q parameters [96] were measured in Bernard and Gravina [81] to be $p = -0.150343\ cm^{-1}$ and $q = -0.1331 \times 10^{-3}\ cm^{-1}$. This yields the zero field lambda doublet splitting frequency of

$$\Delta\nu_{ef} = -(p + 2q) = 4.51\ GHz. \tag{2.22}$$

A general form for the Λ-type doubling frequency for higher J levels can be found in [97] but is beyond the scope of this thesis.

For Hund's case (a) states, the effective magnetic moment is given by [98]

$$\mu_{eff} = \mu_B \frac{(g_L\Lambda + g_s\Sigma)\Omega}{J(J+1)} M_F \tag{2.23}$$

Where $g_L = 1$. For the $A^2\Pi_{1/2}, J = 1/2$ state, $\Lambda = 1$ and $\Sigma = -1/2$, which implies that the first term in the numerator vanishes to first order. However, a small mixing of the nearby $B^2\Sigma_{1/2}$ state creates a Zeeman shift [73]. This Zeeman shift can be calculated by diagonalizing the full Zeeman Hamiltonian (Eq. 9.71 of [92]) and turns out to be

$$E_{Zeeman,\pm} = \pm\frac{1}{3}(g_l' - g_r^{e'})\mu_B B_z M_F \tag{2.24}$$

where ± refers to the parity of the Λ-doublet. The Zeeman parameters g_l' and $g_r^{e'}$ depend on Mulliken and Christy's Λ-doubling p and q parameters as follows [99], [100]

$$\begin{aligned} g_l' &= \frac{p}{2B_\Pi} \\ g_r^{e'} &= -\frac{q}{B_\Pi} \end{aligned} \tag{2.25}$$

where B_Π is the rotational constant for the $A^2\Pi_{1/2}$ state. Bernard and Gravina measured this to have value of 0.385785 cm^{-1} [81] which yields a magnetic moment of $-0.065\mu_B m_F$. The maximum Zeeman shift in the $A^2\Pi_{1/2}, J = 1/2$ occurs for the $F = 1, |m_F| = 1$ state and is a factor of 15 smaller than the largest Zeeman in the $X^2\Sigma^+$ state.

2.5 Vibrational structure of YO

As was pointed by Di Rosa [67], laser cooling molecules requires very diagonal vibrational branching in order to laser cool. As such, we need to calculate the Franck-Condon factors, i.e. the vibrational state overlap

$$q_{eg} = |\langle \psi_g | \psi_e \rangle|^2 \tag{2.26}$$

where e and g are the vibrational quantum numbers of the excited state and ground state respectively. The rovibrational energy for YO can be expressed as quadratic in terms of $(v + 1/2)$ [98], i.e.

$$E = \omega_e(v + \frac{1}{2}) - \omega_e x_e(v + \frac{1}{2})^2 + B_e J(J+1) + D_e(J^2(J+1)^2) - \alpha_e J(J+1)(v + \frac{1}{2}) \quad (2.27)$$

A method used to calculate the vibrational wave functions from spectroscopically derived equilibrium rovibrational molecular parameters was developed by Rydberg [101], Klein [102] and Rees [103] and is known as the RKR method. For each vibrational energy U, we can calculate the classical turning points,

$$r_{1,2} = (f/g + f^2)^{\frac{1}{2}} \pm f \quad (2.28)$$

where the parameters f and g in units of cm and cm^{-1} respectively are given by

$$f[cm] = \sqrt{\frac{h}{8\pi^2 c\mu\omega_e x_e}} \ln\left(\frac{l^2 - 4mA}{l - \sqrt{4mA}}\right) \quad (2.29)$$

$$g[cm^{-1}] = \sqrt{\frac{2\pi^2\mu c}{h(\omega_e x_e)^3}}[\alpha_e\sqrt{4mA} + (2mB_e h + 4mD_e J(J+1) - \alpha_e l)\ln\left(\frac{l^2 - 4mA}{l - \sqrt{4mA}}\right)] \quad (2.30)$$

Here, h, c are expressed in CGS units and the molecular parameters defined in Equation 2.27 are in cm^{-1}. Here μ is the reduced mass in grams and the parameters A, l and m are defined by

$$A = h(U - B_e J(J+1) - D_e(J^2(J+1)^2) \quad (2.31)$$

$$l = \omega_e - \alpha_e J(J+1) \quad (2.32)$$

$$m = \frac{\omega_e x_e}{h} \quad (2.33)$$

The molecular parameters were measured by Bernard and Gravina [81] and relevant parameters are tabulated in Table 2.2

We can then calculate the vibrational potential using the RKR method for the $X^2\Sigma^+$ and $A^2\Pi_{1/2}$ states. For this calculation, we step U in increments of 0.01 cm^{-1} and calculate

Parameter	$X^2\Sigma^+$	$A^2\Pi_{1/2}$
T_e	0	16315.57
ω_e	861.472	820.095
$\omega_e x_e$	2.843	3.346
B_e	0.38892	0.38680
α_e	0.00173	0.00201
D_e	0.318×10^{-6}	0.344×10^{-6}

Table 2.2: Equlibrium rovibrational molecular parameters as measured in [81]. All quantities in cm^{-1}.

the classical turning points $r_{1,2}$ as defined in Eq. 2.28 and thus obtain the potential curves shown in Fig.2.5

With the potentials we can then numerically calculate the vibrational eigen-functions. The time-independent Schrödinger equation is:

$$-\frac{h^2}{2\mu}\frac{d^2}{dr^2}\psi(r) + U(r)\psi(r) = E\psi(r) \tag{2.34}$$

We resample the vibrational potential along a regular grid in r with an increment $d = 2 \times 10^{-3}$ Å. We can then approximate Eq. 2.35 with the discrete equation

$$-\frac{h^2}{2\mu d^2}(\psi(r-d) - 2\psi(r) + \psi(r+d)) + U(r)\psi(r) = E\psi(r) \tag{2.35}$$

Writing ψ as a column vector whose index indicates r, we can then solve the resulting eigen-value problem and obtain the vibrational wave functions shown in Fig. 2.6. We can see that the $v = 0$ state for the $X^2\Sigma^+$ and $A^2\Pi_{1/2}$ states are very similar. The calculated Franck-Condon factors are tabulated in Table 2.3.

The most striking feature is that the $q_{00} = .995$, therefore without any vibrational repumps, the YO molecule can endure 200 optical cycles before falling into higher vibrational state. Furthermore, by repumping the $v = 1$ and 2 levels, we can obtain more than 10^6 scatters, which is sufficient for slowing and trapping.

Since it turns out that J is not a good quantum number in the relevant $X^2\Sigma^+, N'' = 1$ state (see Section 2.7), we calculate the Franck-Condon factors for $J = 1/2$ and $3/2$ and

	J" = 1/2 (RKR)	$J''3/2$ (RKR)	Morse
q_{00}	0.9951	0.9951	.9944
q_{01}	4.672×10^{-3}	4.680×10^{-3}	.0038
q_{02}	2.454×10^{-4}	2.453×10^{-4}	
q_{03}	4.282×10^{-7}	4.279×10^{-7}	-
q_{04}	5.633×10^{-8}	5.624×10^{-8}	-

Table 2.3: Columns 1 and 2: Franck-Condon (FC) factors calculated using the RKR method. Column 3: Franck-Condon factors calculated in [81] using a Morse potential.

we find negligible difference between the two. Also tabulated are Franck-Condon factors calculated using a crude Morse potential in reference [81]. We note that the q_{01} Franck-Condon calculated by RKR is twice as large as that calculated using a the Morse. This is because the high similarity of the two vibrational potentials makes the calculated values of off-diagonal Franck-Condon factors very sensitive to the shapes of the vibrational potential.

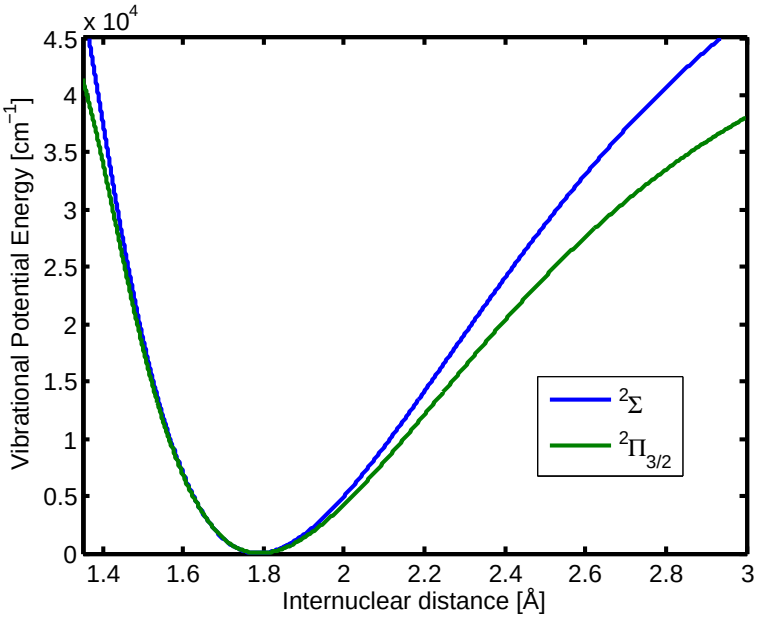

Figure 2.5: Vibrational energy curves for the $^2\Sigma$ and $^2\Pi_{1/2}$ states. The equilibrium internuclear distance for the states are similar, 1.788 Å and 1.793 Å , hence the diagonal FC factors. The 16000 cm^{-1} electronic energy offset is not shown for the $A^2\Pi_{1/2}$ state.

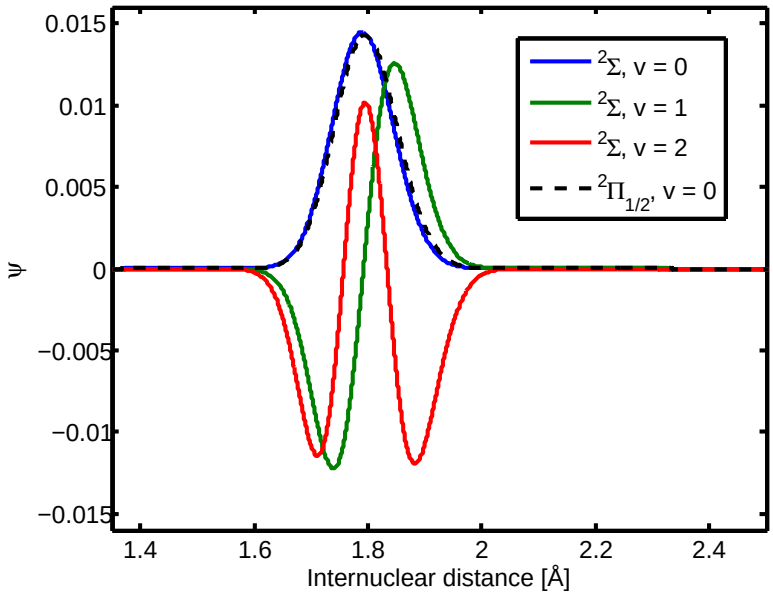

Figure 2.6: Vibrational wave functions of states used in optical cycling.

2.6 Rotational Closure.

As we have seen in section 2.5, by repumping on just the first two vibrational excited states, we can close the vibrational branching to better than 1 part in 10^6. Multiplying this by the photon recoil velocity

$$v_{recoil} = \frac{\hbar k}{m_{YO}} = 6\ mm/s \tag{2.36}$$

we can see that in the absence of other loss mechanisms, we would be able to slow 6000 m/s molecules. Hence this is not a limiting factor in our laser cooling. In this section, we will discuss how we address losses due to rotational branching. This method was inspired by our theoretical proposal [68] and the demonstration of optical cycling in SrF in the Yale group [104].

The ground state is a $X^2\Sigma^+$ as shown in Fig 2.7. The integer parity of N is also the state's parity, indicated by $p = \pm$. In panel (a), we show the way by which YO [71] can be made to optically cycle. Here, only the first excited rational state ($N = 1$) is excited to the $A^2\Pi_{1/2}$, $J = 1/2$ state. The electric dipole (E1) transition selection rules can only link states of opposite parity and so we may only excite to the $p = +$ in the Λ-type parity doublet. As we will see in Eq. 2.38a in Subsection 2.7.1, each excited rotational level ($N \geq 0$) in the $X^2\Sigma^+$ state is a superposition of $J = N \pm 1/2$. Therefore, by the $\Delta J = 0, \pm 1$ selection rule, the excited state with $J' = 1/2$ may only decay to $N < 3$. The same E1 parity selection rule prevents decays to $N = 0, 2$ and thus only decays to $N = 1$ are allowed. This closes off the rotational branching. Clearly, it would be most desirable to cool on the $N = 0$ rotational ground state. However, the same E1 transition selection rules show that rotational closure is not preserved as shown in Figure 2.7(b). For such a scheme, the $X^2\Sigma^+$, $N = 0, +$ state will be excited to the $A^2\Pi_{1/2}$, $J = 1/2, -$ state. While the $\Delta J = 0, \pm 1$ selection rule still restricts decays to states with $N < 3$, parity selection populates both the $N = 0$ and $N = 2$ levels and thus rotational branching opens up.

Finally, YO has an intermediate electronic state, $A'^2\Delta_{3/2}$. As we will see in Chapter

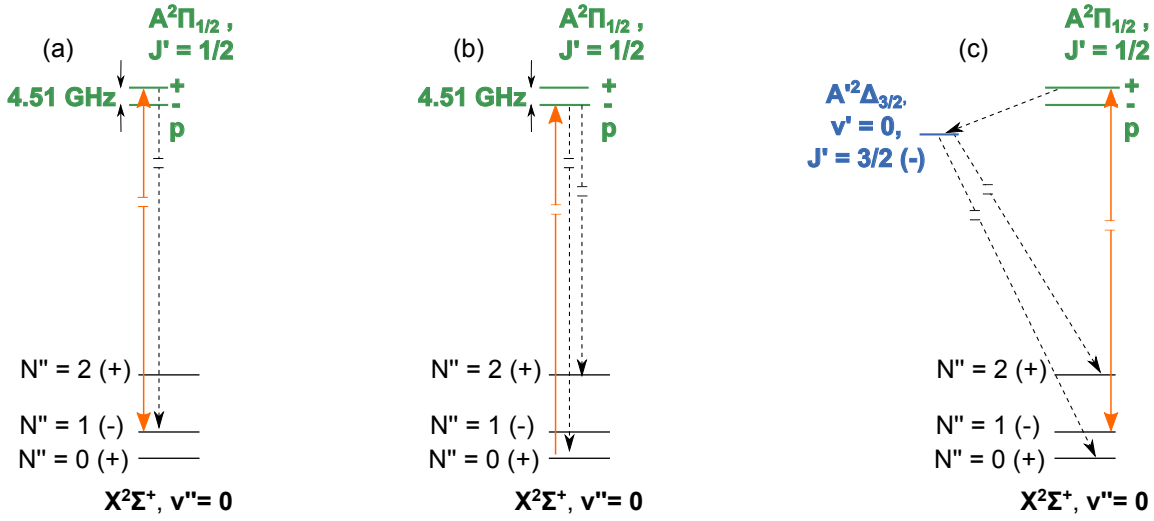

Figure 2.7: (a) Depiction of main optical cycling transition. Via angular momentum selection rules, the YO molecule can only decay back to the $X^2\Sigma^+$, $N = 1$ state. Hence preventing branching. (b) Depiction of the $X^2\Sigma^+$, $N = 0$ non rotationally closed transition. Selection rules allow decay to both $N = 0, 2$. The latter decay breaks the optical cycling. (c) Depiction of decay through intermediate electronic state. Selection rules allow decays into $N = 0, 2$, which breaks the optical cycling.

6, there is a small branching ($\approx 3 \times 10^{-4}$) to this state. This is a loss mechanism as the full cycle starting from and returning to the ground state is a three-photon (1 pump and 2 decay) (Fig .2.7 (c)), thus after this process, the ground state changes parity. On occasion, instead of decaying back to the $X^2\Sigma^+$, $N = 1$ state, the molecule relaxes to the $A'^2\Delta_{3/2}, J = 3/2, -$ state. The $J = 3/2$ is the lowest rotational level here and the ΔJ selection rules prevents decays to higher rotational levels. The ΔJ selection rules permits decays to states with $N < 4$ and from these permitted rotational levels, parity allows decays to only $N = 0, 2$. In sum, this process pumps the $N = 1$ to the $N = 0, 2$, thus shutting down optical cycling.

2.7 Calculating branching ratios.

2.7.1 Converting the $X^2\Sigma^+$ state to the Hund's case (a) basis.

To calculate branching ratios to each of the hyperfine states in molecules, it is necessary to convert all the states in question into one Hund's case. For the YO molecule, these calculations will be done in the (a) basis.

However, the $X^2\Sigma^+$ state is not only a Hund's case (b) state but due to the large Fermi contact, the YO molecule has the unusual $b_{\beta S}$ angular momentum coupling. For more conventional Hund's case $b_{\beta J}$ basis, the angular momentum coupling follows the form $|(I, (S, N)J)F\rangle$. Thus there is a 2 step process to transform to the (a) basis.

First, to transform from the $b_{\beta S}$ to the $b_{\beta J}$ basis, we need to apply Wigner 6-j symbols as specified in [92], p 156.

$$|((I, S)G, N)F\rangle = \sum_J [(2G+1)(2J+1)]^{1/2}(-1)^{I+S+F+N} \begin{Bmatrix} I & S & G \\ N & F & J \end{Bmatrix} |(I, (S, N)J)F\rangle \tag{2.37}$$

For the $N = 1$ state, the four hyperfine states are written as

$$|G = 0, F = 1\rangle = \sqrt{\frac{2}{3}}\left|J = \frac{3}{2}, F = 1\right\rangle - \sqrt{\frac{1}{3}}\left|J = \frac{1}{2}, F = 1\right\rangle \tag{2.38a}$$

$$|G = 1, F = 0\rangle = |J = 1/2, F = 0\rangle \tag{2.38b}$$

$$|G = 1, F = 1\rangle = \sqrt{\frac{1}{3}}\left|J = \frac{3}{2}, F = 1\right\rangle + \sqrt{\frac{2}{3}}\left|J = \frac{1}{2}, F = 1\right\rangle \tag{2.38c}$$

$$|G = 1, F = 2\rangle = \left|J = \frac{3}{2}, F = 2\right\rangle \tag{2.38d}$$

.

It turns out that in general, for other values of N,

$$\begin{aligned}|G = 0, F = N\rangle =& \sqrt{\frac{1}{2N+1}}\Big(\sqrt{N+1}\left|J = N + \frac{1}{2}, F = N\right\rangle \\ &- \sqrt{N}\left|J = N - \frac{1}{2}, F = N\right\rangle\Big)\end{aligned} \tag{2.39a}$$

$$|G = 1, F = N - 1\rangle = \left|J = N - \frac{1}{2}, F = N - 1\right\rangle \tag{2.39b}$$

$$\begin{aligned}|G = 1, F = N\rangle =& \sqrt{\frac{1}{2N+1}}\Big(\sqrt{N}\left|J = N + \frac{1}{2}, F = N\right\rangle \\ &+ \sqrt{N+1}\left|J = N - \frac{1}{2}, F = N\right\rangle\Big)\end{aligned} \tag{2.39c}$$

$$|G = 1, F = N + 1\rangle = \left|J = N + \frac{1}{2}, F = N + 1\right\rangle \tag{2.39d}$$

. where for the $N = 0$ case, only Eq. 2.39 a,d are to be used.

In Hund's case (a), the quantum numbers are Λ, S, Σ, J and Ω and following from p 230 of [92], the conversion is:

$$|\Lambda, N, S, J\rangle = \sum_{\Sigma=-S}^{+S}(-1)^{J-S+\Lambda}\sqrt{2N+1}\begin{pmatrix} J & S & N \\ \Omega & -\Sigma & -\Lambda \end{pmatrix}|\Lambda; S, \Sigma, J, \Omega\rangle \tag{2.40}$$

where the array in parentheses is a Wigner 3-j symbol. We see that from equation 2.39, for each rotational manifold, we have superpositions of states with $J = N \pm \frac{1}{2}$. Applying

Eq. 2.40, we get:

$$\left|N, J = N + \frac{1}{2}\right\rangle = \frac{1}{\sqrt{2}}\Big(\left|\Sigma = \frac{1}{2}, \Omega = \frac{1}{2}\right\rangle - \left|\Sigma = -\frac{1}{2}, \Omega = -\frac{1}{2}\right\rangle \Big) \tag{2.41a}$$

$$\left|N, J = N - \frac{1}{2}\right\rangle = \frac{1}{\sqrt{2}}\Big(\left|\Sigma = \frac{1}{2}, \Omega = \frac{1}{2}\right\rangle + \left|\Sigma = -\frac{1}{2}, \Omega = -\frac{1}{2}\right\rangle \Big) \tag{2.41b}$$

Finally, this lets us write out the all four of the hyperfine states in the $b_{\beta S}$ in terms of the a basis.

$$\begin{aligned}
|G = 0, F = N\rangle = &\sqrt{\frac{1}{2(2N+1)}} \\
&\Big(\sqrt{N+1}\left|J = N + \frac{1}{2}, \Sigma = \Omega = \frac{1}{2}, F = N\right\rangle \\
&- \sqrt{N+1}\left|J = N + \frac{1}{2}, \Sigma = \Omega = -\frac{1}{2}, F = N\right\rangle \\
&- \sqrt{N}\left|J = N - \frac{1}{2}, \Sigma = \Omega = \frac{1}{2}, F = N\right\rangle \\
&- \sqrt{N}\left|J = N - \frac{1}{2}, \Sigma = \Omega = -\frac{1}{2}, F = N\right\rangle \Big)
\end{aligned} \tag{2.42a}$$

$$\begin{aligned}
|G = 1, F = N - 1\rangle = &\sqrt{\frac{1}{2}}\Big(\left|J = N - \frac{1}{2}, \Sigma = \Omega = \frac{1}{2}, F = N - 1\right\rangle \\
&+ \left|J = N - \frac{1}{2}, \Sigma = \Omega = -\frac{1}{2}, F = N - 1\right\rangle \Big)
\end{aligned} \tag{2.42b}$$

$$\begin{aligned}
|G = 1, F = N\rangle = &\sqrt{\frac{1}{2(2N+1)}} \\
&\Big(\sqrt{N}\left|J = N + \frac{1}{2}, \Sigma = \Omega = \frac{1}{2}, F = N\right\rangle \\
&- \sqrt{N}\left|J = N + \frac{1}{2}, \Sigma = \Omega = -\frac{1}{2}, F = N\right\rangle \\
&+ \sqrt{N+1}\left|J = N - \frac{1}{2}, \Sigma = \Omega = \frac{1}{2}, F = N\right\rangle \\
&+ \sqrt{N+1}\left|J = N - \frac{1}{2}, \Sigma = \Omega = -\frac{1}{2}, F = N\right\rangle \Big)
\end{aligned} \tag{2.42c}$$

$$\begin{aligned}
|G = 1, F = N + 1\rangle = &\sqrt{\frac{1}{2}}\Big(\left|J = N + \frac{1}{2}, \Sigma = \Omega = \frac{1}{2}, F = N + 1\right\rangle \\
&- \left|J = N + \frac{1}{2}, \Sigma = \Omega = -\frac{1}{2}, F = N + 1\right\rangle \Big).
\end{aligned} \tag{2.42d}$$

Again for the special case of $N = 0$, we only use Eq. 2.42 a,d. Specifying for $N = 1$, the optical cycling ground state,

$$
\begin{aligned}
|G=0,F=1\rangle =& \sqrt{\frac{1}{3}}\left|J=\frac{3}{2},\Sigma=\Omega=\frac{1}{2},F=1\right\rangle - \sqrt{\frac{1}{3}}\left|J=\frac{3}{2},\Sigma=\Omega=-\frac{1}{2},F=1\right\rangle \\
& - \sqrt{\frac{1}{6}}\left|J=\frac{1}{2},\Sigma=\Omega=\frac{1}{2},F=1\right\rangle - \sqrt{\frac{1}{6}}\left|J=\frac{1}{2},\Sigma=\Omega=-\frac{1}{2},F=1\right\rangle \\
|G=1,F=0\rangle =& \sqrt{\frac{1}{2}}\Big(\left|J=\frac{1}{2},\Sigma=\Omega=\frac{1}{2},F=0\right\rangle + \left|J=\frac{1}{2},\Sigma=\Omega=-\frac{1}{2},F=0\right\rangle \\
|G=1,F=1\rangle =& \sqrt{\frac{1}{6}}\left|J=\frac{3}{2},\Sigma=\Omega=\frac{1}{2},F=1\right\rangle - \sqrt{\frac{1}{6}}\left|J=\frac{3}{2},\Sigma=\Omega=-\frac{1}{2},F=1\right\rangle \\
& + \sqrt{\frac{1}{3}}\left|J=\frac{1}{2},\Sigma=\Omega=\frac{1}{2},F=1\right\rangle + \sqrt{\frac{1}{3}}\left|J=\frac{1}{2},\Sigma=\Omega=-\frac{1}{2},F=1\right\rangle \\
|G=1,F=2\rangle =& \sqrt{\frac{1}{2}}\Big(\left|J=\frac{3}{2},\Sigma=\Omega=\frac{1}{2},F=2\right\rangle - \left|J=\frac{3}{2},\Sigma=\Omega=-\frac{1}{2},F=2\right\rangle
\end{aligned}
\tag{2.43}
$$

2.7.2 Calculating dipole moments.

There are three transitions for which we wish to calculate the hyperfine branching ratios. The electric dipole (E1) transition between the $A^2\Pi_{1/2}$, $J = \frac{1}{2}$ state and the $X^2\Sigma$, $N = 1$ state; the E1 transition between the $A^2\Delta_{3/2}$, $J = \frac{3}{2}$ state and the $X^2\Sigma$, $N = 1$; and the magnetic dipole (M1) transition between the $A^2\Pi_{1/2}$, $J = \frac{1}{2}$ state and the $X^2\Sigma$, $N = 1$ state.

We are going to calculate transition dipole moments

$$\langle d\rangle = \langle\Psi_e|\, T^1_p(d)\,|\Psi_g\rangle \tag{2.44}$$

and square them to obtain the branching ratios in question. Here $T^1_p(d)$ is the first rank tensor denoting the electric or magnetic dipole moment and p denotes the polarization of light. Following the treatment in section 5.5 of [92], in particular, applying the Wigner-Eckart

theorem

$$\begin{aligned}\langle d\rangle &= \langle J', I', F', M'_F|\ T^1_p(\mathbf{d})\,|J, I, F, M_F\rangle \\ &= (-1)^{F'-M'_F}\begin{pmatrix} F' & 1 & F \\ -M'_F & p & M_F\end{pmatrix} \\ &\quad (-1)^{F+J'+I+1}\sqrt{(2F'+1)(2F+1)}\begin{Bmatrix} J & F & I \\ F' & J' & 1\end{Bmatrix} \\ &\quad \langle \Lambda', S', \Sigma', \Omega', J'|\,|T^1(\mathbf{d})|\,|\Lambda, S, \Sigma, \Omega, J\rangle\,. \end{aligned} \tag{2.45}$$

We can further reduce the final term by transforming into the molecule's body fixed frame:

$$\begin{aligned}\langle \Lambda', S', \Sigma', \Omega', J'|\,|T^1(\mathbf{d})|\,|\Lambda, S, \Sigma, \Omega, J\rangle = \sum_{q=-1}^{1}(-1)^{J'-\Omega'}\sqrt{(2J'+1)(2J+1)} \\ \begin{pmatrix} J' & 1 & J \\ -\Omega' & q & \Omega\end{pmatrix}\langle \Lambda', S', \Sigma'|\,T^1(\mathbf{d})\,|\Lambda, S, \Sigma\rangle\,\hat{\epsilon}_q^{el/mag}.\end{aligned} \tag{2.46}$$

The term $\langle \Lambda', S', \Sigma'|\,T^1(\mathbf{d})\,|\Lambda, S, \Sigma\rangle$ would require knowledge of the electronic wavefunctions but as it is common to all branches, it is not needed to calculate the relative branching ratios. The term $\hat{\epsilon}_q^{el/mag}$ is a vector that indicates the projection of the electric or magnetic dipole moment on the body fixed axis and from the appendix of [58]:

$$\hat{\epsilon}_{\pm1}^{el} = i \tag{2.47}$$

$$\hat{\epsilon}_{\pm1}^{mag} = \mp 1 \tag{2.48}$$

$$\hat{\epsilon}_0^{el/mag} = 0. \tag{2.49}$$

These vectors are responsible for the parity selection rules for electric (E1) and magnetic (M1) dipole transitions.

2.7.3 $X^2\Sigma^+, N = 1 \leftarrow A^2\Pi_{1/2}, J = 1/2$, E1 transition.

The optical cycling connects to the state of positive parity in the $A^2\Pi_{1/2}$, $J = \frac{1}{2}$ state as the $X^2\Sigma$, $N = 1$, has negative parity. From p.251 of Brown and Carrington [92], states of good parity for Hund's case (a) are given by

$$\begin{aligned}
|\Lambda; J, M_J; +\rangle &= \frac{1}{\sqrt{2}}\Big(|\Lambda; S, \Sigma; J, \Omega, M_J\rangle + (-1)^{J-S} |\Lambda; S, -\Sigma; J, -\Omega, M_J\rangle \Big) \\
|\Lambda; J, M_J; -\rangle &= \frac{1}{\sqrt{2}}\Big(|\Lambda; S, \Sigma; J, \Omega, M_J\rangle - (-1)^{J-S} |\Lambda; S, -\Sigma; J, -\Omega, M_J\rangle \Big)
\end{aligned} \tag{2.50}$$

The $A^2\Pi_{1/2}$, $J = \frac{1}{2}$ (+) state is can be rewritten as:

$$\begin{aligned}
\left|\Pi; J = \frac{1}{2}, M_J; +\right\rangle = \frac{1}{\sqrt{2}}\Big(&\left|\Lambda = 1; S = \frac{1}{2}, \Sigma = -\frac{1}{2}; J = \frac{1}{2}, \Omega = \frac{1}{2}, M_J\right\rangle \\
&+ \left|\Lambda = -1; S = \frac{1}{2}, \Sigma = +\frac{1}{2}; J = \frac{1}{2}, \Omega = -\frac{1}{2}, M_J\right\rangle \Big)
\end{aligned} \tag{2.51}$$

A computer program was written in Mathematica to evaluate all of the branching ratios. Due to the angular momentum selection rules for the electric dipole transition, only decays to the $N = 1$ level in the ground Σ state are allowed from the $A^2\Pi_1/2, J = 1/2$ (-) state are allowed. As a consistency check, the branching ratios in each column of Table 2.4 add up to 1. In table 2.5, we sum up the branching ratios over M_F and average over M'_F.

	(F', M'_F)			
(G, F, M_F)	(0,0)	(1,-1)	(1,0)	$(1, 1)$
(0,1,-1)	8/27	1/54	1/54	0
(0,1,0)	8/27	1/54	0	1/54
(0,1,1)	8/27	0	1/54	1/54
(1,0,0)	0	2/9	2/9	2/9
(1,1,-1)	1/27	25/108	25/108	0
(1,1,0)	1/27	25/108	25/108	0
(1,1,1)	1/27	0	25/108	25/108
(1,2,-2)	0	1/6	0	0
(1,2,-1)	0	1/12	1/12	0
(1,2,0)	0	1/36	1/9	1/36
(1,2,1)	0	0	1/12	1/12
(1,2,2)	0	0	0	1/6

Table 2.4: Branching ratios for the $X^2\Sigma, N = 1 \leftarrow A^2\Pi_1/2, J' = 1/2$, electric dipole (E1) transition, i.e. the main optical cycling transition. Columns are denoted by the excited state's hyperfine numbers (F', M'_F) and the rows are denoted by the ground states (G, F, M_F) numbers.

(G,F)	$F'=0$	$F'=1$
(0,1)	8/9	1/27
(1,0)	0	2/9
(1,1)	1/9	25/54
(1,2)	0	5/18

Table 2.5: Branching ratios for the $X^2\Sigma, N=1 \leftarrow A^2\Pi_1/2, J=1/2$, electric dipole transition, i.e. the main optical cycling transition. The branching ratios are summed over M_F and averaged over M'_F. Columns are denoted by the excited state's hyperfine numbers F' and the rows are denoted by the ground states (G,F) numbers.

2.7.4 $X^2\Sigma, N=0,2 \leftarrow A'^2\Delta_{3/2}, J=1/2$, E1 transition.

Branching to the $A'^2\Delta_{3/2}$ state occur at a part in three thousand level from the $A^2\Pi_{1/2}$ state. Such decays are deleterious to the optical cycling as this decay requires 3 photons and thus the YO molecule decays to (+) parity states in the ground electronic state. This is the opposite parity from where the YO molecule and would stop the optical cycling as different rotational states are now populated. The rotational ground state of the $A'^2\Delta_{3/2}$ state has $J=\frac{3}{2}$ and by the $\Delta J \leq 1$ selection rule, is the only state that can be populated by decays from the $A^2\Pi_{1/2}, J=1/2$ state. For the $A'\Delta$ state, we optically pump into the odd parity state since it requires a two-photon process from the ground state and from Equation 2.50, is expressed as

$$\left|\Delta; J=\frac{1}{2}, M; +\right\rangle = \frac{1}{\sqrt{2}}\Big(\left|\Lambda=2; S=\frac{3}{2}, \Sigma=-\frac{1}{2}; J=\frac{1}{2}, \Omega=\frac{3}{2}, M\right\rangle + \left|\Lambda=-2; S=\frac{1}{2}, \Sigma=+\frac{1}{2}; J=\frac{3}{2}, \Omega=-\frac{3}{2}, M\right\rangle \Big). \tag{2.52}$$

The calculated branching ratios for the $X^2\Sigma^+, N=0$ state are shown in Table 2.6 and for $N=2$ is shown in Table 2.7. In Table 2.8, branching ratios are summed over M_F and averaged over M'_F. By summing over all the G and F levels in each rotational manifold, we

see that the total branching ratio to $N = 0$ and to $N = 2$ are both $\frac{1}{2}$.

(G, F, M_F)	$\Delta_{3/2}, J' = 3/2, (F', M'_F)$							
$N = 0$	(1,-1)	(1,0)	(1,1)	(2,-2)	(2,-1)	(2,0)	(2,1)	(2,2)
(0,0,0)	1/3	1/3	1/3	0	0	0	0	0
(1,1,-1)	1/12	1/12	0	1/2	1/4	1/12	0	0
(1,1,0)	1/12	0	1/12	0	1/4	1/3	1/4	0
(1,1,1)	0	1/12	1/12	0	0	1/12	1/4	1/2

Table 2.6: Branching ratios for the $X^2\Sigma, N = 0 \leftarrow A'^2\Delta_{3/2}, J' = 3/2$, electric dipole transitions. Columns are denoted by the excited state's hyperfine numbers (F', M'_F) and the rows are denoted by the ground states (G, F, M_F) numbers.

(G, F, M_F)	$\Delta_{3/2}, J' = 3/2, (F', M'_F)$							
$N = 2$	(1,-1)	(1,0)	(1,1)	(2,-2)	(2,-1)	(2,0)	(2,1)	(2,2)
(0,2,-2)	1/250	0	0	49/375	49/750	0	0	0
(0,2,-1)	1/500	1/500	0	49/750	49/1500	49/500	0	0
(0,2,0)	1/1500	1/375	1/1500	0	49/500	0	49/500	0
(0,2,1)	0	1/500	1/500	0	0	49/500	49/1500	49/750
(0,2,2)	0	0	1/250	0	0	0	49/750	49/375
(1,1,-1)	1/6	1/6	0	1/25	1/50	1/150	0	0
(1,1,0)	1/6	0	1/6	0	1/50	2/75	1/50	0
(1,1,1)	0	1/6	1/6	0	0	1/150	1/50	1/25
(1,2,-2)	12/125	0	0	128/1125	64/1125	0	0	0
(1,2,-1)	6/125	6/125	0	64/1125	32/1125	32/375	0	0
(1,2,0)	2/125	8/125	2/125	0	32/375	0	32/375	0
(1,2,1)	0	6/125	6/125	0	0	32/375	32/1125	64/1125
(1,2,2)	0	0	12/125	0	0	0	64/1125	128/1125
(1,3,-3)	0	0	0	1/15	0	0	0	0
(1,3,-2)	0	0	0	1/45	2/45	0	0	0
(1,3,-1)	0	0	0	1/225	8/225	2/75	0	0
(1,3,0)	0	0	0	0	1/75	1/25	1/75	0
(1,3,1)	0	0	0	0	0	2/75	8/225	1/225
(1,3,2)	0	0	0	0	0	0	2/45	1/45
(1,3,3)	0	0	0	0	0	0	0	1/15

Table 2.7: Branching ratios for the $X^2\Sigma, N = 2 \leftarrow A'^2\Delta_{3/2}, J' = 3/2$, electric dipole transition. Columns are denoted by the excited state's hyperfine numbers (F', M'_F) and the rows are denoted by the ground states (G, F, M_F) numbers.

	$\Delta_{3/2}, J' = 3/2, (F')$	
(N, G, F)	(1)	(2)
(0,0,0)	1/3	0
(0,1,1)	1/6	1/2
(2,0,2)	1/150	49/250
(2,1,1)	1/3	1/25
(2,1,2)	4/25	64/375
(2,1,3)	0	7/75

Table 2.8: Branching ratios for the $X^2\Sigma, N = 0 \leftarrow A'^2\Delta_{3/2}, J' = 3/2$, electric dipole transitions. Branching ratios are summed across M_F and averaged over M'_F. Columns are denoted by the excited state's hyperfine numbers (F') and the rows are denoted by the ground states (N, G, F) numbers. Summing across G and F, the branching ratio to $N = 0$ and $N = 2$ are both $\frac{1}{2}$.

2.7.5 $X^2\Sigma, N = 0, 2 \leftarrow A'^2\Pi_1/2, J' = 1/2$, M1 transition.

The optical cycling scheme for molecules relies on the fact that an electric dipole transition can only connect states of opposite parity. However, M1 transitions connect states of the same parity, hence, if the YO molecule relaxes via an M1 transition, it will end up in the wrong parity and hence we opent up decays to other rotational states and the cycling comes to a stop.

While it is commonly assumed that magnetic dipole transitions are suppressed by a factor $\alpha^2 \approx 5 \times 10^{-5}$ compared to E1 transitions, where α is the fine structure constant, quantum chemistry calculations and experimental measurements in OH show a factor of 7 [58] higher than expected magnetic dipole transition strength. This may lead to larger than expected rotational branching and become a limiting factor in optical cycling.

In the optical cycling transition, the YO molecules relaxes from the $J = 1/2, +$ state

and by angular momentum and parity selection the $N = 0, 2$ levels are populated. The branching ratios are tabulated for $N = 0$ in Table 2.9 and for $N = 2$ in Table 2.10. The branching ratios are summed up over M_F for each F value and averaged over M'_F and tabulated in Table 2.11. By summing over all the G and F levels in each rotational manifold, we see that the total branching ratio to $N = 0$ is $\frac{2}{3}$ and to $N = 2$ is $\frac{1}{3}$.

(G, F, M_F)	$\Pi_{1/2}, J' = 1/2, (F', M'_F)$			
$N = 2$	(0,0)	(1,-1)	(1,0)	(1,1)
(0,0,0)	0	2/9	2/9	2/9
(1,1,-1)	2/9	2/9	2/9	0
(1,1,0)	2/9	2/9	0	2/9
(1,1,1)	2/9	0	2/9	2/9

Table 2.9: Branching ratios for the $X^2\Sigma, N = 0 \leftarrow A^2\Pi_{1/2}, J = 1/2$, magnetic dipole (M1) transitions. Columns are denoted by the excited state's hyperfine numbers (F', M'_F) and the rows are denoted by the ground states (G, F, M_F) numbers.

(G, F, M_F)	$\Pi_{1/2}, J' = 1/2, (F', M'_F)$			
$N = 2$	(0,0)	(1,-1)	(1,0)	(1,1)
(0,2,-2)	0	1/15	0	0
(0,2,-1)	0	1/30	1/30	0
(0,2,0)	0	1/90	2/45	1/90
(0,2,1)	0	0	1/30	1/30
(0,2,2)	0	0	0	1/15
(1,1,-1)	1/9	1/36	1/36	0
(1,1,0)	1/9	1/36	0	1/36
(1,1,1)	1/9	0	1/36	1/36
(1,2,-2)	0	1/10	0	0
(1,2,-1)	0	1/20	1/20	0
(1,2,0)	0	1/60	1/15	1/60
(1,2,1)	0	0	1/20	1/20
(1,2,2)	0	0	0	1/10

Table 2.10: Branching ratios for the $X^2\Sigma, N = 2 \leftarrow A^2\Pi_{1/2}, J = 1/2$, magnetic dipole transitions. Columns are denoted by the excited state's hyperfine numbers (F', M'_F) and the rows are denoted by the ground states (G, F, M_F) numbers. F = 3 states are omitted since the $\Delta F \leq 1$ selection rule prevents decays to that state.

	$\Delta_{3/2}, J' = 3/2, (F')$	
(N, G, F)	(0)	(1)
(0,0,0)	0	2/9
(0,1,1)	2/3	4/9
(2,0,2)	0	1/9
(2,1,1)	1/3	1/18
(2,1,2)	0	1/6
(2,1,3)	0	0

Table 2.11: Branching ratios for the $X^2\Sigma^+ \leftarrow A^2\Pi_{1/2}, J' = 1/2$, magnetic dipole transitions. Branching ratios are summed across M_F and averaged over M'_F. Columns are denoted by the excited state's hyperfine numbers (F') and the rows are denoted by the ground states (N, G, F) numbers. Summing across G and F, the branching ratio to $N = 0$ is $\frac{2}{3}$ and to $N = 2$ is $\frac{1}{3}$.

Chapter 3

Laser setup.

Due to the more complex internal structure of molecules, the laser cooling of YO requires several laser systems. At the heart of the optical setup is a 100 MHz self-referenced Er doped fiber comb [105]. This provides a frequency ruler that references all of the other lasers that are used to manipulate the YO molecules. These lasers include a dye laser, several external cavity diode lasers (ECDLs) and a fiber based Raman amplifier. In this chapter we will describe these laser systems and the schemes used to frequency stabilize them.

3.1 An introduction to frequency combs

Mode-locked pulsed lasers have been powerful tools in frequency metrology [106,107] by allowing easily generated and measured radio frequencies to control a wide comb of regularly spaced optical frequencies. A mode-locked laser in the time domain is a set of regular spaced intensity pulses separated in time by t_{rep}, the repetition period; the inverse of this is known as the repetition frequency $f_{rep} = t_{rep}^{-1}$ (Fig. 3.1 (a)). The width of the pulse is on the order of the frequency bandwidth of the gain medium (shown schematically in blue in (b).

As depicted in (a), the electric field also has a phase offset with respect to the amplitude envelope. For a mode-locked laser, between consecutive pulses, there is a constant phase offset ϕ_{co}, known as the carrier offset phase. In the frequency domain the mode-locked laser's spectrum is a regular comb with frequency spacing f_{rep} offset by the so called carrier

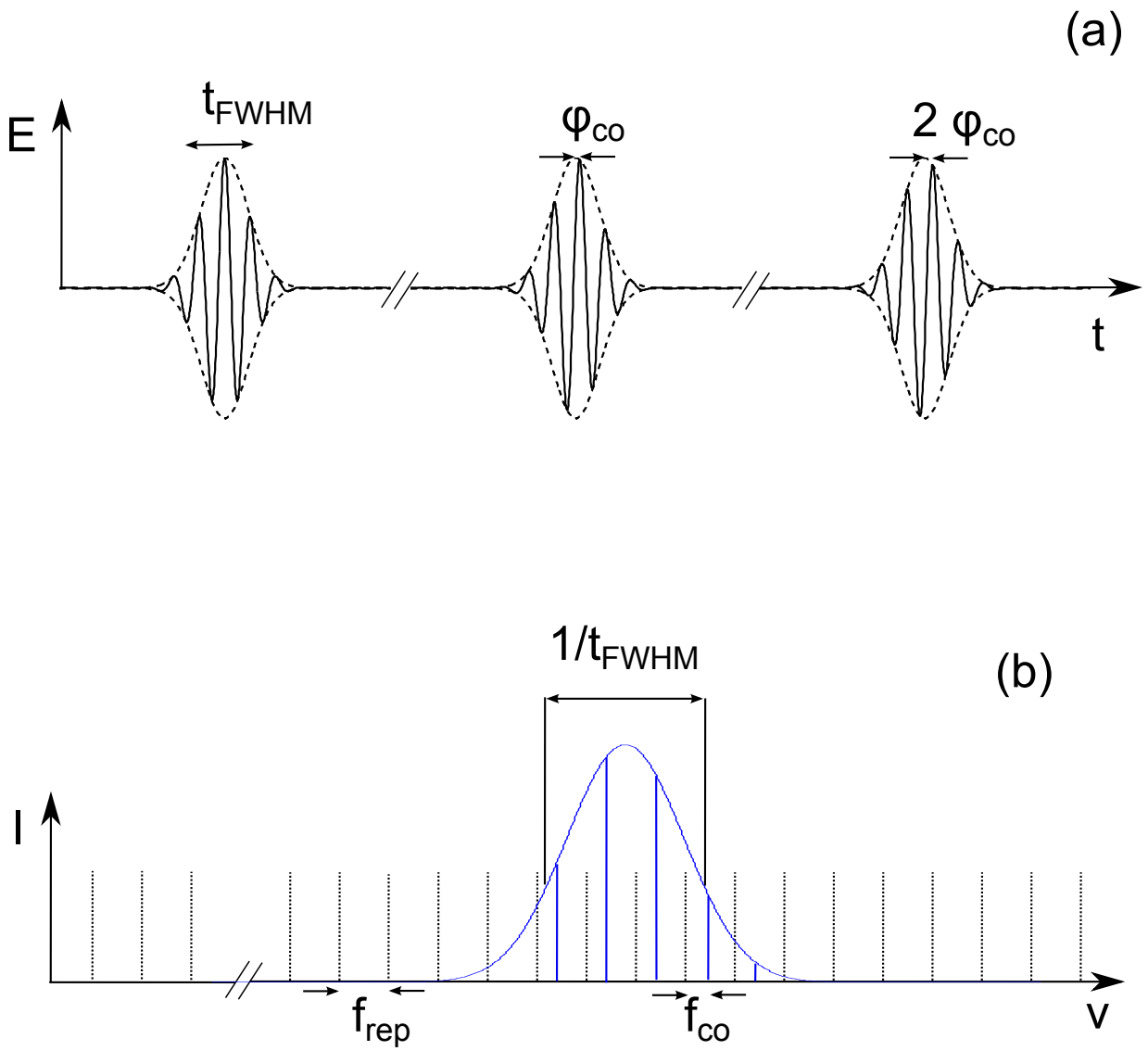

Figure 3.1: Illustration of a mode-locked laser. (a) Mode-locked laser electric field (E) in the time domain. (b) Mode-locked laser in the frequency domain.

offset frequency, f_{CO}:

$$f_{CO} = f_{rep} \times \frac{\phi_{co}}{2\pi} \tag{3.1}$$

The phase slip between the amplitude envelope and the electric field is due to the difference between the group and phase velocities and an excellent description may be found in Seth Foreman's thesis [108].

3.2 Erbium Doped Fiber Frequency Comb

The laser stabilization scheme relies upon an 100 MHz repetition rate Erbium (Er^{3+}) mode-locked fiber comb . The comb is remarkably robust and can maintain mode-lock for several months at a time. Technology for the Erbium fiber laser has pushed forward due to the telecommunications industry, which makes the laser fairly inexpensive and parts readily available.

The relevant energy levels for Er^{3+} are shown in Fig. 3.2. The pump is at 980 nm and the lasing transition occurs between the lowest two lowest levels at 1530 nm. A two pump photon transition also occurs, leading to radiation at 550 nm. This gives rise to the characteristic green glow from the Erbium doped fibers.

When doped into the silica fiber host, a combination of homogenous and inhomogeneous broadening [109] results in a broad absorption band which makes it suitable for a mode-locked laser.

This laser is passively mode-locked using the technique known as polarization additive pulse mode locking (P-APM) [110, 111]. In brief, elliptically polarized light entering the gain fiber is rotated by an angle that is intensity and ellipticity dependent. By applying the opposite polarization rotation at high intensity with the freespace waveplates as shown in figure 3.3(a), the laser will passively mode-lock. The resulting mode-locked spectrum is shown in figure 3.3 (b).

Figure 3.3 (a) shows a schematic of the comb oscillator. The pump light is provided by a fiber Bragg grating stabilized 980 nm pump diode (part number : JDSU 29-800-500) that provides up to 500 mW of power. The pump laser is coupled into the cavity via a wavelength division multiplexer (WDM) in a counterpropagating manner. This is advantageous as the laser pulse propagates towards regions of greater gain inversion, thus increasing the overall gain. Also, because of the counterpropagating topology, no pump light pollutes our output due to the free space optical isolator (OI). The cavity has a net dispersion of 0.022 ps^2. This

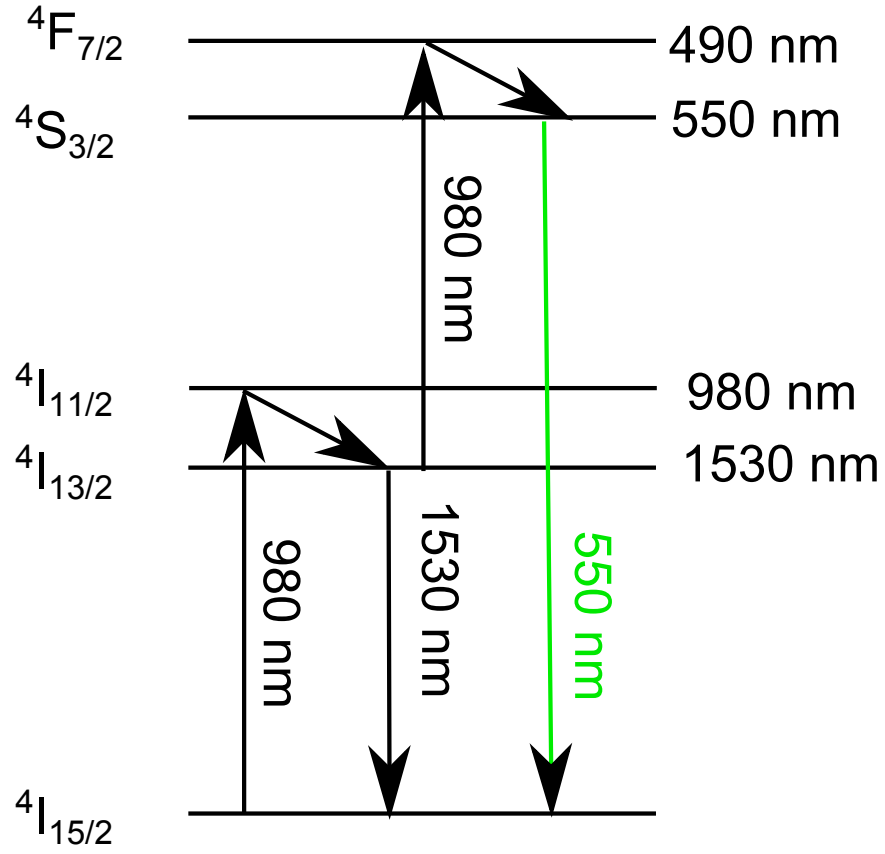

Figure 3.2: Level structure of Er^{3+}. The lasing transition occurs at 1530 nm and is the laser is pumped by 980 nm light.

relatively high dispersion was chosen to achieve longer intra-cavity pulses ($\sim$ 100 fs), which leads to higher output power. A polarizing beam splitter (PBS) cube is used to outcouple $\sim$20% of the light, and we thus obtain $\approx$6 mW output power with $\approx$35 mW of circulating power.

Stabilization of the repetition rate is achieved with an rf phase lock to the 10th harmonic of f_{rep}. Approximately 4% of of the mode-locked laser's output is picked off and sent to an InGaAs photo-diode and band-passed filtered. This detection scheme is shown in Figure 3.4. A 1 GHz signal generated by a ultrastable Wenzl crystal oscillator is mixed with an adjustable frequency $f_{rep,synth} \approx 5\ MHz$ signal that is generated by an Analog Devices Direct

Digital Synthesizer referenced to the same crystal oscillator source. The 10th harmonic is then phase locked to the lower sideband with frequency ≈995 MHzm which allows us to use $f_{rep,synth}$ to tune the entire frequency comb.

$$f_{rep} = \frac{1GHz - f_{rep,synth}}{10} \tag{3.2}$$

Changes in f_{rep} are actuated with an in-fiber electro-optic modulator (General Photonics Fiber Phase Shifter) with a bandwidth of ∼12 kHz. A slower long throw actuator consists of a collimating lens mounted on a PZT driven mount.

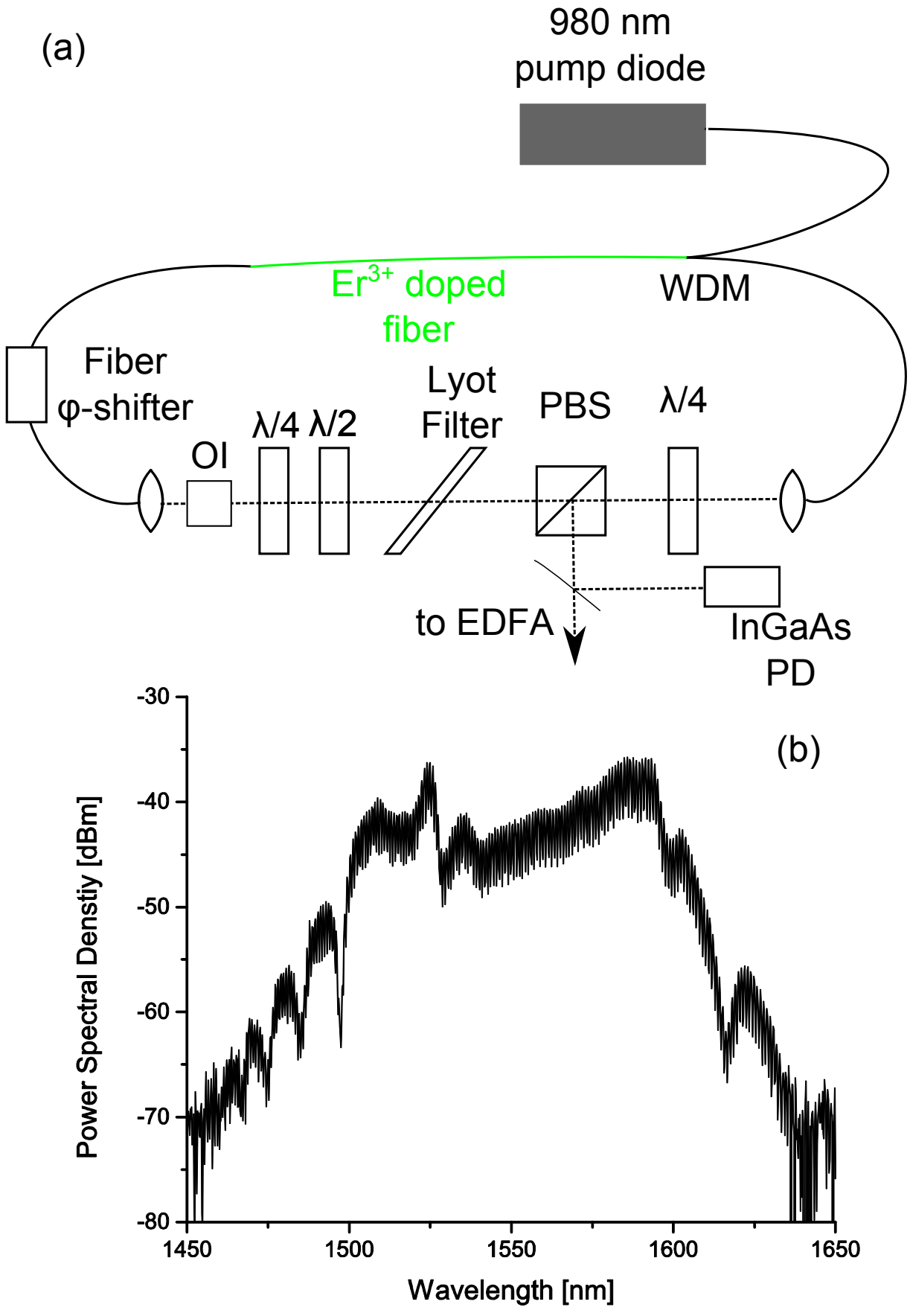

Figure 3.3: (a) Schematic of 1550 nm mode-locked fiber comb. (b) Mode-locked Spectrum.

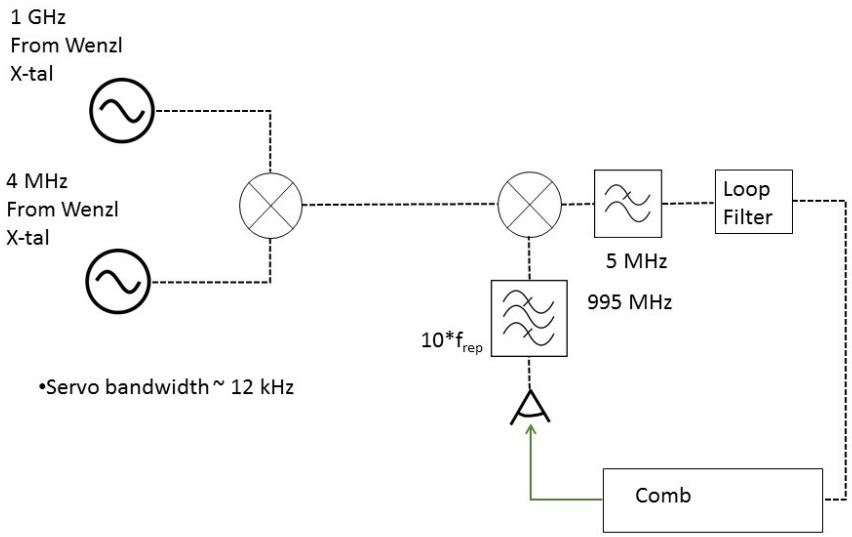

Figure 3.4: Schematic of f_{rep} detection and stabilization.

3.2.1 Octave spanning supercontinuum

As can be seen in Fig. 3.3 (b), the comb oscillator spectrum only covers about 100 nm. This is insufficient for our purposes for 2 reasons. One, this does not overlap with the lasers that we wish to stabilize and two, a much larger spectrum is required in order to measure the carrier-offset frequency f_{co}. The key to broadening the spectrum is a highly nonlinear fiber. For our wavelength range, such fibers are Germanium doped, have a reduced core diameter of 3.7 μm and have a zero dispersion wavelength of $\approx$ 1520 nm [112,113]. The small core (which is less than half the diameter of SMF-28) ensures a high intensity to ensure the non-linear spectral broadening effects. An advantage of this fiber is that can be spliced onto regular fiber (e.g. SMF-28) using standard techniques. In our system $\approx$10 cm of non-linear fiber is spliced onto $\approx$10 cm of SMF-28, as the comb light is fiber-coupled into the much larger core diameter fiber, it is much less sensitive to misalignments and makes the supercontinuum generation much more robust. This is in contrast to the small core diameter micro-structure photonic crystal fiber (PCF) used to broaden mode-locked titanium-sapphire lasers where the microstructure is destroyed during the splicing process.

The 6 mW that we produce from the oscillator is insufficient to induce the spectral broadening. As such, we amplify the light using an Erbium Doped Fiber Amplifier (EDFA) [114] as shown in Figure 3.5. The EDFA is a $\approx$10 cm length of the same Er^{3+} fiber, pumped on both ends with 980 nm fiber Bragg grating diode lasers coupled via WDMs. Each pump diode produces 700 mW (Part number: World Star Tech LC96UF74-20R) and we obtain 180 mW of infra-red power after amplification. The light is then sent through a free space silicon prism pair that recompresses the pulse. Fine tuning of the dispersion compensation is provided by moving one of the prisms mounted on a micrometer stage. The light is then fiber coupled into the non-linear fiber, which produces 80 mW total power in the super-continuum.

A typical octave spanning supercontinuum spectrum is shown in Fig. 3.6. The comb light used to stabilize the various lasers and for measuring f_{CO} are indicated by grey dots.

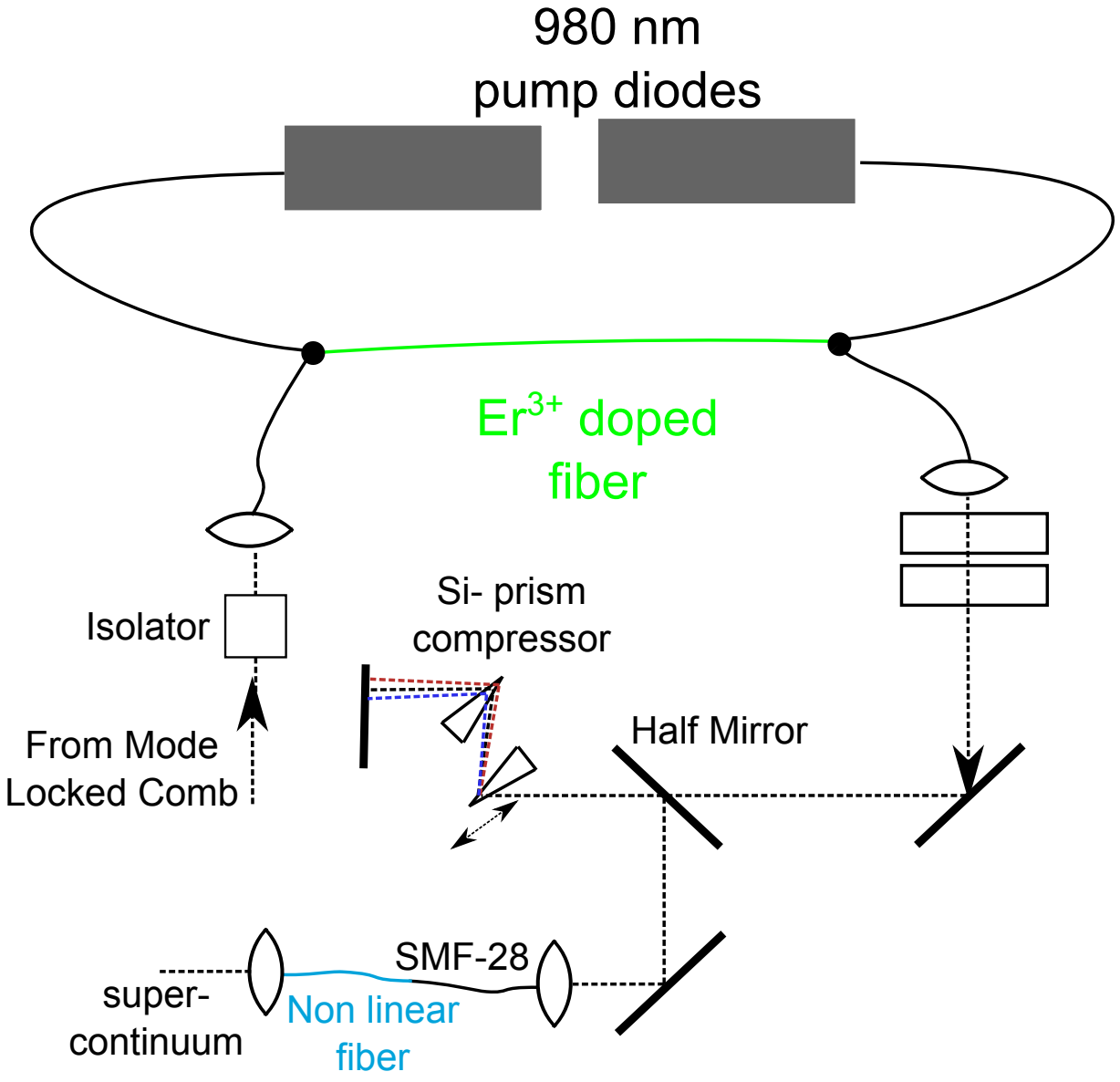

Figure 3.5: Schematic of supercontinuum generation. 6 mw light from the mode-locked comb is amplified with the EDFA to 180 mW. A silicon prism pair is used compress the pulse before being spectrally broadened by the highly non-linear fiber.

Light at 1050 nm and 2100 nm (not shown) is used for self-referencing, while the comb teeth at 1228 and 1298 nm are used to stabilize the various cooling and repump lasers.

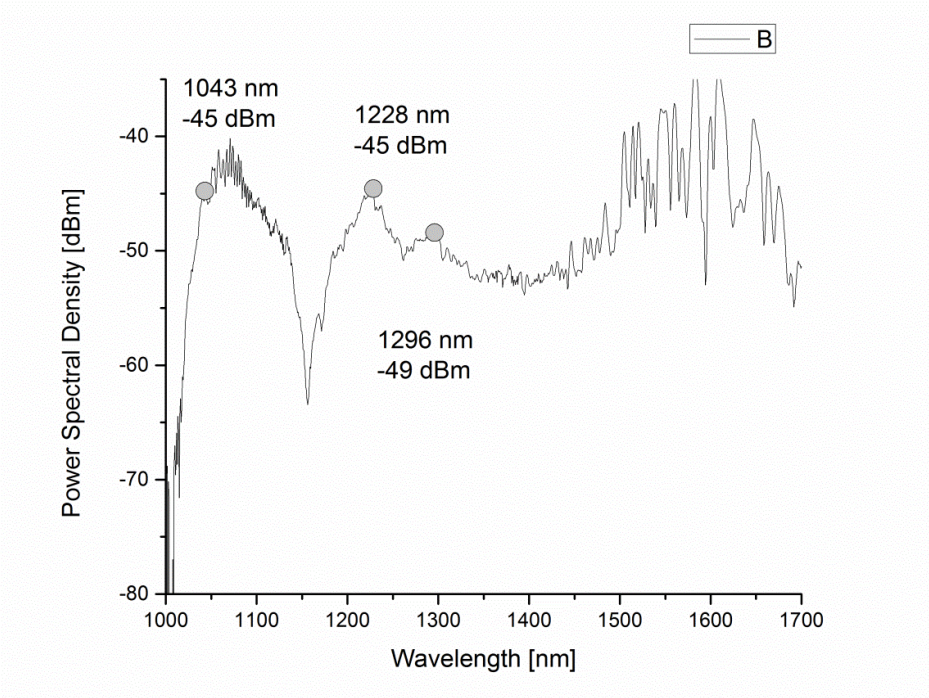

Figure 3.6: Super-continuum Spectrum. The wavelengths used for various heterodyne beats are indicated by grey dots. The 1228 and 1298 nm light is frequency is used to stabilize the lasers used in the experiment . Light at 1050 nm and 2100 nm (not shown) is used to measure f_{CO}.

3.2.2 Measuring f_{CO} with an f-2f interferometer

The determination of the carrier offset frequency f_{co} is more difficult to measure than the repetition frequency. For this, we use the technique of self-referencing of an octave spanning comb [115–117].

The frequency of the n-th comb tooth can be expressed as

$$f_n = nf_{rep} + f_{co} \tag{3.3}$$

To perform the self referencing measurement, we frequency double the portion of the supercontinuum at ∼2100 nm yielding a new frequency comb with the following frequency comb teeth,

$$f_{2f-arm} = mf_{rep} + 2f_{co} \tag{3.4}$$

where m is another integer. The term $2f_{co}$ comes from the fact that each new comb tooth is generated by the sum frequency of two of the original comb teeth. We may mix the frequency-doubled comb, i.e. the 2f arm, and the undoubled light at ∼1050 nm and the lowest frequency component in the heterodyne signal is the offset frequency f_{co}.

The optical scheme is shown in figure 3.9. To generate the frequency-doubled light, we used a magnesium oxide doped periodically poled lithium niobate (MgO:PPLN) crystal (part number: Covega SHG 7 crystal). The pulse intensity is sufficiently high that we may use the crystal without cavity enhancement and obtain an approximate conversion efficiency of 10 %. The f-2f interferometer is set up with a Michelson interferometer topology. The retroreflecting mirror on the undoubled arm is mounted on a micrometer stage; this allows fine adjustments in order to temporally overlap the pulses from the two arms. Both arms are split and recombined with a 1500 nm dichroic mirror and are both sent through the doubling crystal. A 10 nm bandpass filter at 1050 nm filters out the unneeded spectral components in the undoubled arm and the resulting heterodyne beat is detected on an InGaAs photodiode.

Figure 3.9 shows a schematic for the f_{CO} stabilization. First the heterodyne signal is sent through a 50 MHz low pass filter, thus filtering out all frequency components except

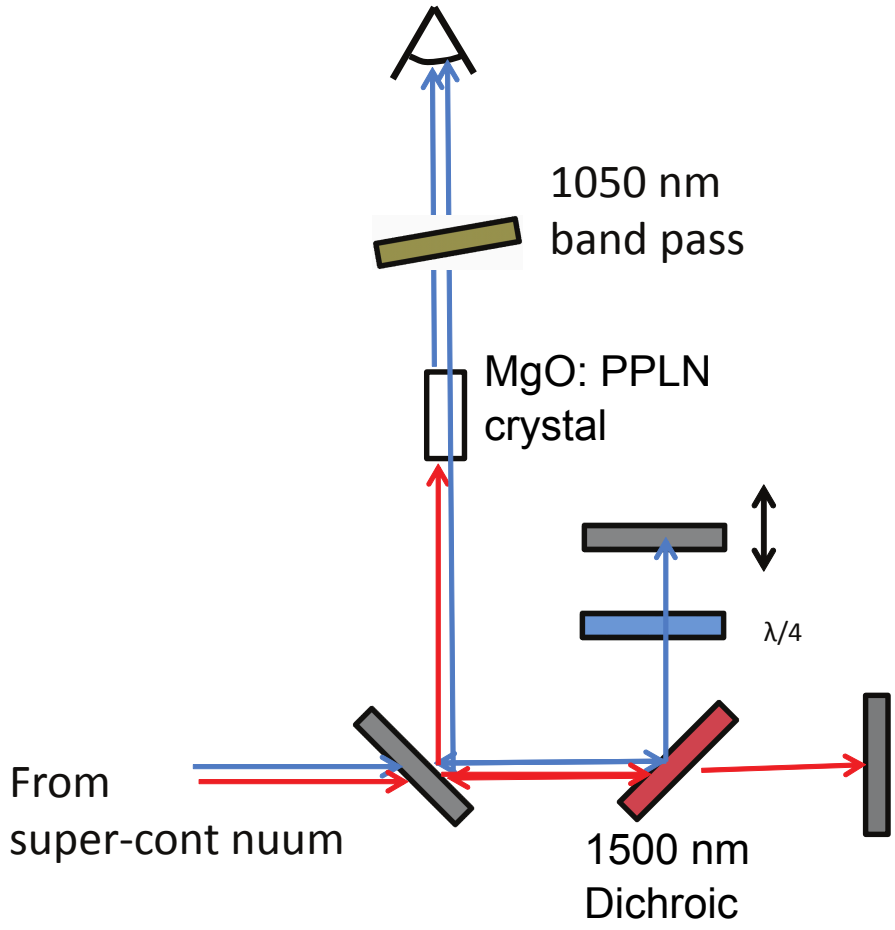

Figure 3.7: Schematic of f_{co} detection. Blue arrows indicate light at ∼1050 nm and red arrows indicates light at ∼2100 nm. A dichroic mirror at 1500 nm splits the light between the 2 arms of the interferometer. The MgO:PPLN frequency doubles the 2100 nm portion of the spectrum.

for f_{CO}. This signal is mixed with a 43 MHz signal and high-pass filtered such that only the 43 MHz+f_{CO} sideband passes through. This signal is cleaned up with an rf tracking filter, i.e. a VCO phase locked to the input signal. The phase difference between the tracking filter's output and a tunable synthesizer, $f_{synth,CO}$ is measured with a home built phase frequency detector (note that the tracking filter's frequency is divided by 4 in the phase frequency detector). To close the loop, feedback is applied to the pump diode current of the comb

oscillator. This affects the in-cavity dispersion, which in turn affects the group and phase velocity mismatch and therefore changes f_{CO}. We may express the carrier offset frequency as:

$$f_{CO} = 4 \times f_{synth,CO} - 43MHz \tag{3.5}$$

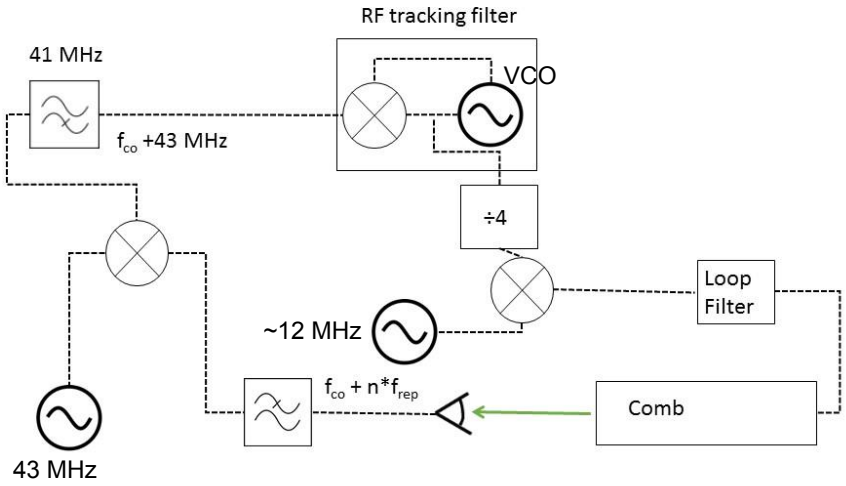

Figure 3.8: f_{co} stabilization.

3.3 Light for the main cooling transition at 614 nm

3.3.1 Dye Laser

To provide the 614 nm light required for the main cooling transition, we use a commercial Matisse DR dye laser from Sirah Lasertechnik [118]. To attain this awkward wavelength, we use Rhodamine 610 dye mixed in ethylene glycol with a concentration of 0.57 g/L. The dye is forced through a slit nozzle at a pressure of 13.5 bar, creating a free-space dye jet less than a 1 mm thick. Care needs to be taken to ensure that the dye jet drains correctly; if not, the dye will spray uncontrollably, and a tedious clean up job awaits.

The laser is pumped with 6.5 W of 532 nm from a Verdi V-10 Nd:YAG laser. Two

concave mirrors (FM) set the cavity mode and ensure the cavity is stable. Rhodamine 610 has a lasing range of several 10s of nm while the free spectral range (FSR) of the overall lasing cavity is ∼160 MHz. Therefore in order to ensure that only one of these modes lases, we require three frequency selection elements. The coarsest frequency selection element is the birefringent filter [119],(Bi-Fi), consisting of a stack of three birefringent plates having thicknesses ratio 1:3:15. This narrows the possible lasing range to ∼200 GHz. The thin etalon (TE) and the thick etalon (PZETL) have FSRs of 250 GHz and 20 GHz respectively. The PZETL's length is dither locked to coincide with the maximum transmission of the appropriate longitudinal laser cavity mode.

To ensure lasing only occurs in the counter-clockwise sense, there is Faraday rotator (FR), which consists of a Terbium-Gallium-Garnet crystal plate placed between two rare earth magnets. The out of plane mirror on the right of the laser cavity induces a small polarization rotation that is cancelled by the FR for counter-clockwise propagation and adds for clockwise propagation. Brewster losses off the dye jet, FR, TE and Bi-Fi prevents lasing in the clockwise sense; this forms an optical diode. Despite this optical diode, care must be taken to slightly vertically misalign the PZETL as back reflections off it can lead to bi-directional lasing. This leads to intensity and frequency instability and the laser becomes unworkable at that point. To stabilize the frequency, the overall cavity length can be changed by two mirrors mounted on PZTs. The first, labelled the FPZ mirror has a bandwidth of $\sim$ 20 kHZ. A slow long throw PZT on the mirror labelled SPZ has bandwidth of ∼10 Hz and takes care of long-term drifts. Typically, we can obtain ≈400 mW of power on fresh dye which lasts for 2-3 weeks.

3.3.2 Raman Amplifier

For the implementation of the 3D MOT where longitudinal slowing is required, an independent laser at 614 nm became very desirable for the independent frequency tuning and for more power. Therefore, we have a Raman fiber amplifier from MPB-Communications

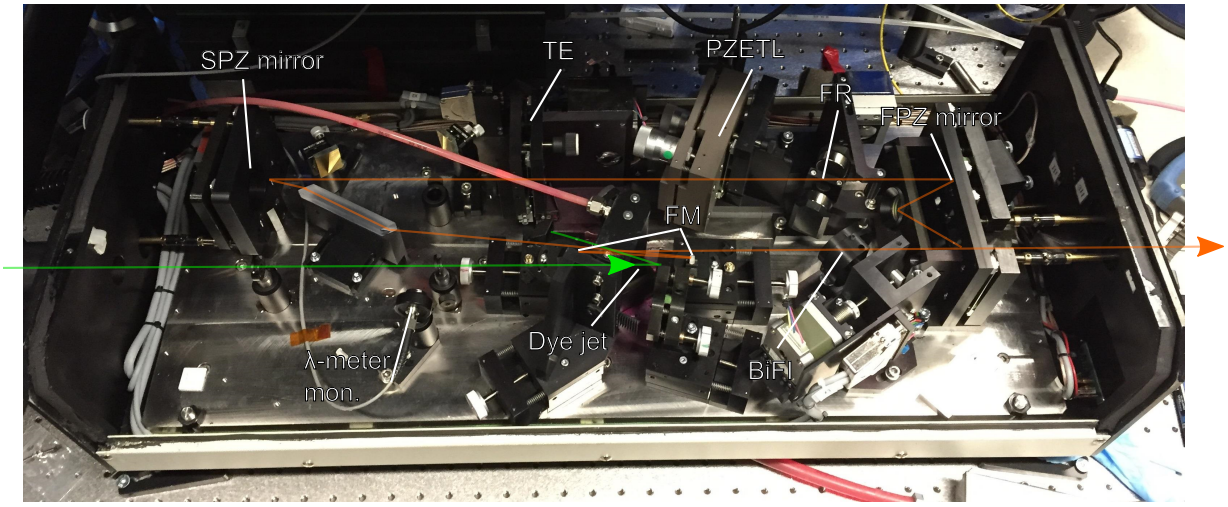

Figure 3.9: Photograph of the Matisse DR dye laser system.

Inc [120]. Here, a seed laser, in our case at 1228 nm, is amplified in a P_2O_5 doped fiber pumped with a Ytterbium fiber laser. It turns out that for these so called P-doped fibers, a strong stimulated Raman scattering peak occurs at ≈40 THz [121]. This therefore allows us to bridge the gap between the seed wavelength at 1228 nm and the pump wavelength of ≈1050 nm. The input seed light is generated with an ECDL diode (Innolume GC-1230-TO-200) that is directly frequency stabilized to the comb. 20 mW of seed diode power is fiber-coupled into the Raman amplifier. The 1228 nm light is amplified to ∼10 W and is then frequency doubled and we can obtain greater than 1 W of 614 nm light.

As the entire system, sans the seed laser, is fiber coupled, operation of this laser is robust and mostly turn-key. The wavelength range of such Raman-based amplifier systems is limited by the Yb fiber laser pump and ranges from 515-670 nm [120]. Other wavelengths should be accessible by using a different pump laser. With the more robust optical alignment, similar wavelength range and the elimination of (mostly toxic) laser dye, this can be an excellent replacement for a dye laser. The seed diode is used in a Littrow ECDL configuration [122] and frequency stabilization is performed by changing the pump current.

3.3.3 Stabilization of 614 nm lasers.

To stabilize the seed diode, the comb light and $\sim$ 100 μW of the seed diode are mixed using a 50-50 beam splitter cube as shown in Figure 3.10. As the optical heterodyne signal from the two exit ports of the PBS have a π phase shift between them, we use two photodiodes and subtract the signals in order to obtain the heterodyne signal. In addition, this subtraction mostly eliminates the seed diode's technical noise in the heterodyne signal. We note that this is the same configuration as used to generate the heterodyne between the vibrational repumps and the comb.

For the 1228 nm seed laser, we applied frequency feedback by changing the diode pump current, and we obtain an in-loop linewidth of 140 kHz (Fig 3.11(b)) (for 1 second averaging). The light at 614 nm will have twice that linewidth but is still well within the natural linewidth of the YO transition.

Relative to the comb frequencies, the output frequency of the Raman amplifier's frequency doubler (at 614 nm) is thus

$$f_{raman} = 2(n_{raman} f_{rep} + f_{co} + f_{Het,RamanComb}) \tag{3.6}$$

where $f_{Het,RamanComb} = 21.5MHz$ is the difference between the seed laser's frequencies and the nearest comb tooth and n_{raman} is an integer on the order of 2.5×10^6.

With the Raman amplifier stabilized, we then phase lock the dye laser to the doubled portion of the Raman amplifier. A schematic of the dye laser to Raman amplifier locking is shown in Figure 3.11 (a). Most of the Raman amplifier power is sent through a 60 MHz AOM, where the -1 order is used to provide the light for radiation pressure slowing. This allows us to perform rapid switching of the slowing beam. If we were to address the stationary molecule, the frequency at the output of the Raman amplifier's doubler, f_{raman}, will be given by

$$f_{raman} = f_{YO} + 60MHz \tag{3.7}$$

where f_{YO} is the resonance frequency of the YO transition. It turns that in the course of

the longitudinal slowing, we will be chirping f_{raman} to gradually address slower molecules (the chirping will be discussed in section 3.6). The peak of the velocity distribution is at 70 m/s, which implies a doppler shift of 112 MHz. In contrast, as the dye laser provides the MOT radiation, we do not need to have any frequency scanning. This allows us to leave the dye laser at the optimal MOT detuning at all times and also lessens the workload of the dye laser's frequency stabilization. Therefore, the offset frequency between the Raman amplifier and the dye laser is controlled by a VCO, which has a tuning range of 130 MHz, allowing us to compensate for the full slowing chirp. Therefore, the control voltage on our VCO has two components, 1) the voltage to apply the correct frequency offset for MOT loading and 2) the voltage to cancel the Raman amplifier's frequency chirps.

A small portion of the doubled Raman amplifier light is sent through a 107.5 MHz double-passed AOM. This upshifts the frequency by 215 MHz which gets us in the range of the VCO. The two 614 nm optical frequencies [in MHz] are related to f_{YO} by

$$f_{raman} + 215MHz = f_{YO} + 60MHz - 1.6 * v_{long} \tag{3.8}$$

$$f_{dye} = f_{YO} + \delta \tag{3.9}$$

where f_{YO} is the resonance frequency of YO, v_{long}, is the longitudinal velocity class that we wish to address and δ is the desired MOT detuning. We can then solve for the VCO's frequency to be

$$f_{VCO} = f_{raman} + 215[MHz] + 60[MHz] - \delta - 1.6 * v_{long} \tag{3.10}$$

which for the case of $\delta = -\Gamma = -5MHz$, the slowing laser can address molecules ranging from 0-81 m/s. In contrast to the Raman-comb lock, the heterodyne components here have much more power ($\sim 100\ \mu$W each), and we can easily obtain signal to noise ratios of 40 dB. This results in an in-loop linewidth with respect to the doubled Raman amplifier of 400 kHz (Figure 3.11 (c)).

3.4 Vibrational repumps

The light for each vibrational repump is provided with a master diode that injection locks a string of slave diodes and tapered amplifiers. Like the seed laser for the Raman Amplifier, the master laser for the vibration repumps are set in a Littrow configuration [122]. The diode used is an Eagleyard Photonics EYP-RWE-0650. The diode has a nominal central wavelength of 653 nm.

The diode mounting is shown in Fig. 3.12 and is based on a design from [123]. The diode is mounted in a standard Thorlabs laser diode collimation tube. The grating is a holographic reflecting grating with 1800 lines/mm and is mounted on a vertical flexure, that can be adjusted by a micrometer actuator. This can be used to maximize the feedback of the diode. The mount is cooled down to ≈16 °C to reach the desired wavelength of 648 or 649 nm. Optical isolation of 60 dB is required and we can obtain 11 mW of output power. Approximately 1 mW of the diode light is picked off and frequency shifted by a single pass AOM by ≈100 MHz. This light is then heterodyned with the doubled comb light as shown schematically in Fig. 3.10. Here the doubling of the comb light is performed with a custom MgO:PPLN crystal from HC Photonics.

The frequency of the repump light is therefore

$$f_{v=x} = n_{v=x} f_{rep} + 2f_{co} + f_{Het} + |f_{ao}| \tag{3.11}$$

here $x = 1, 2$ refers to the vibrational repump in question. The exact frequency of the offset AOM can be set to position the locked heterodyne beat f_{Het} at a convenient location. The factor of 2 f_{co} is due to the frequency doubling of the comb-light. The frequency correction is actuated by the PZT that changes the grating angle; this leads to an in-loop linewidth relative to the comb of 770 kHz.

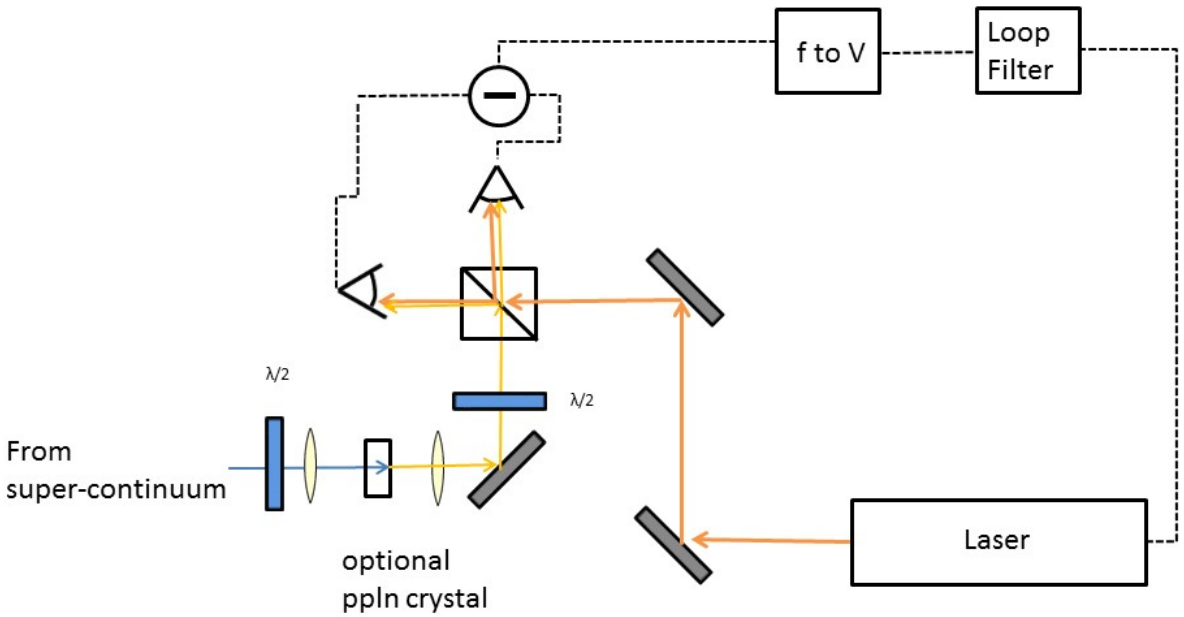

Figure 3.10: Schematic of comb-laser heterodyne beat generation. Optical PPLN crystal doubles near infrared to the visible and is used in locking vibrational repumps. For the Raman laser at 614 nm no PPLN crystal is required.

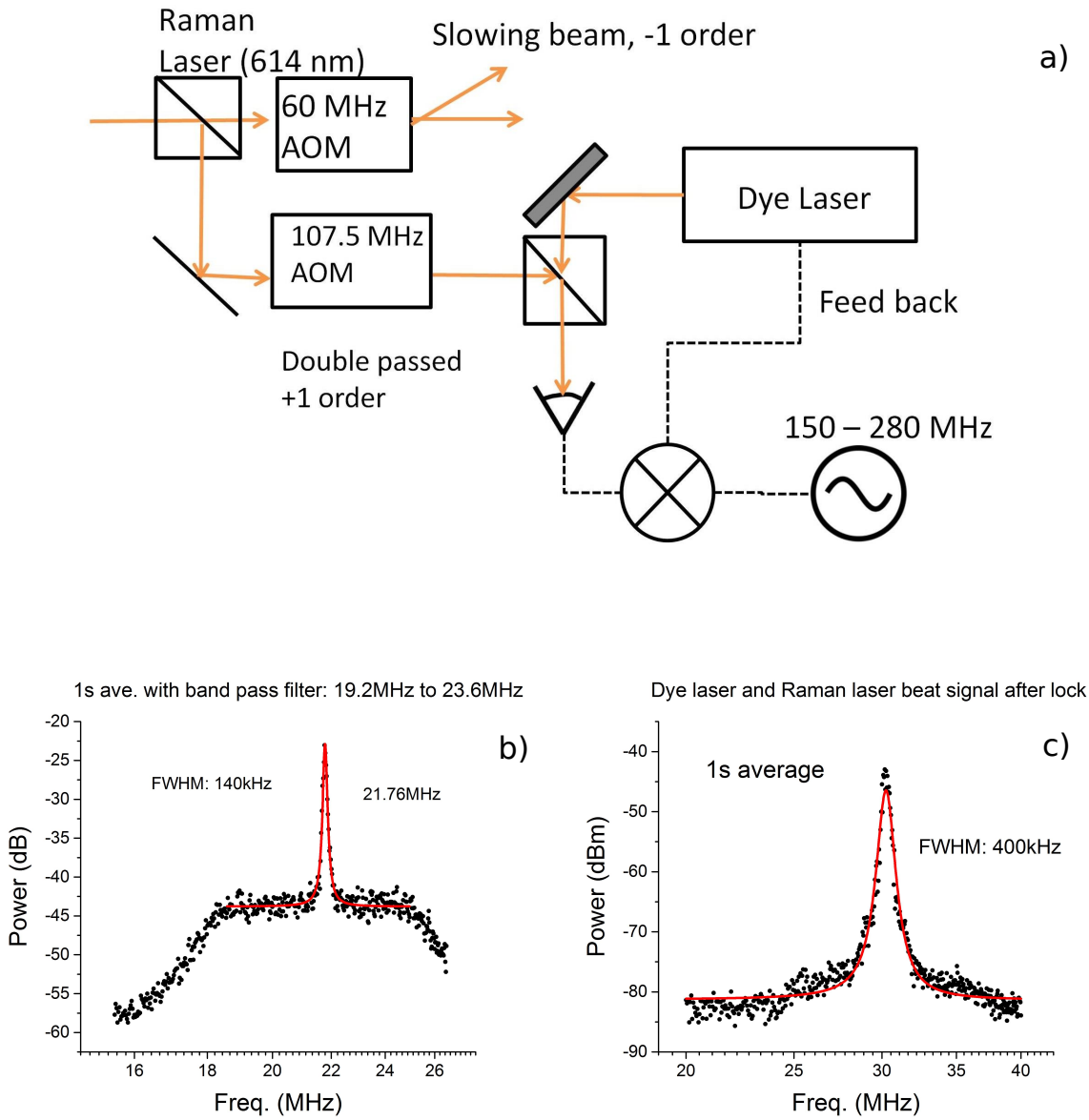

Figure 3.11: a) Schematic of Dye-Raman Amp phase lock. (b) In-loop linewidth measurement of the Raman Amplifier seed laser at 1228 nm with respect to the frequency comb. (c) In-loop linewidth of the dye laser with respect to the doubled Raman amplifier output at 614 nm.

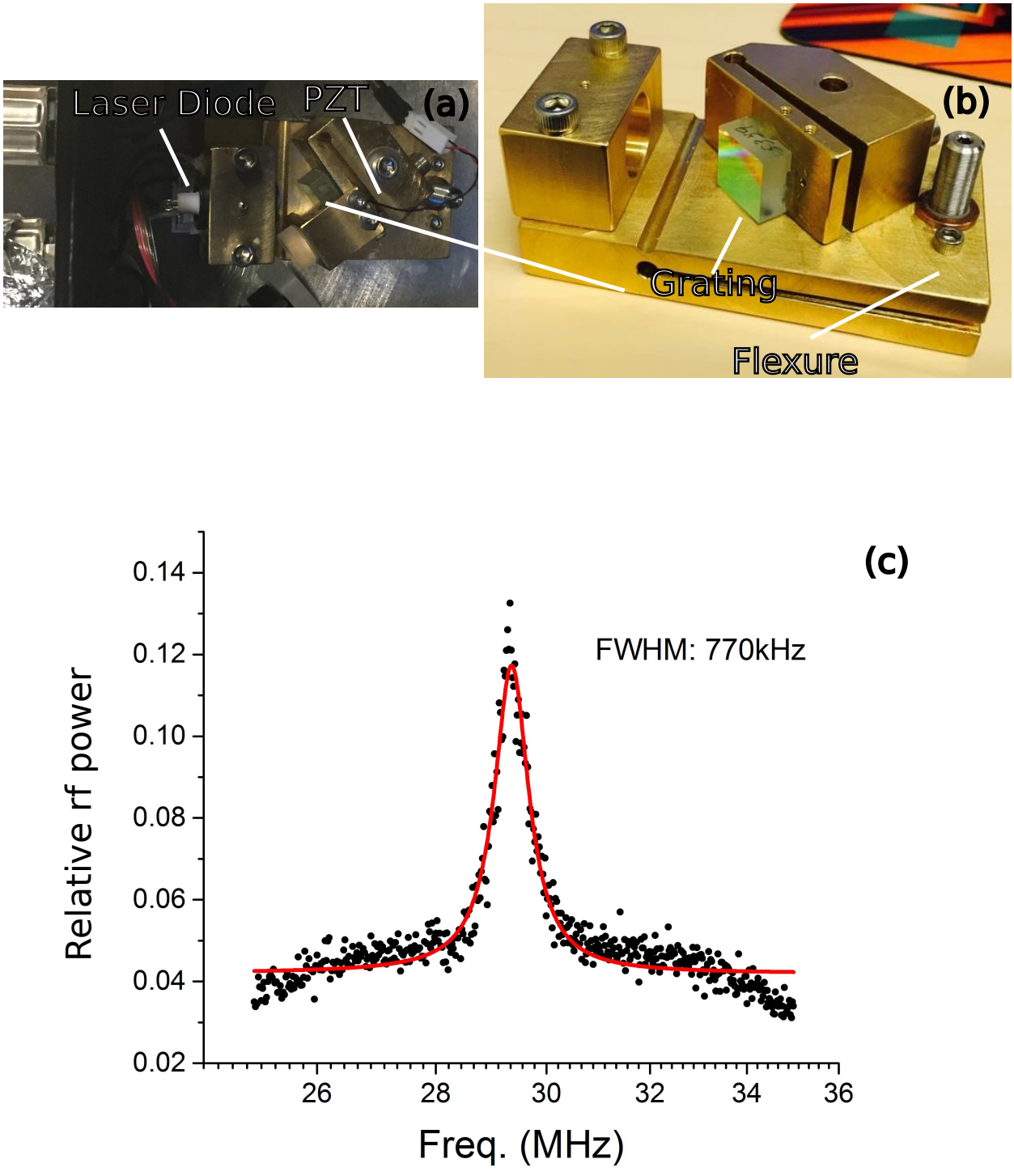

Figure 3.12: (a) Top view of Littrow mount. (b) Side view of partially assembled mount. (c) In-loop linewidth of the comb to master diode lock.

3.5 Frequency to Voltage Convertor

In the YO experiment, all laser locks to the comb use a home built frequency to voltage convertor. Commercial frequency to voltage convertors are generally limited to acoustic frequencies and are not fast enough to measure the optical heterodyne beats that can go up to $f_{rep}/2 = 50$ MHz. We therefore adapted a circuit designed by John Hall that can measure frequencies of up to 80 MHz.

An illustration of the f to V convertor is shown in fig 3.13. A TTL convertor converts the incoming heterodyne frequency into a TTL signal. This is then sent through a bistable flip flop, which divides the TTL frequency by two and helps to sharpen the rising and falling edges of the signal. Based on the sign of the TTL signal, a high stability current supply will charge the charge pump capacitor with either plus or minus 10 mA. Two diodes upstream of the charge pump capacitor are tied to two voltage rails set at ± 6.95 V. Therefore, on each half TTL cycle, the charge pump capacitor is alternately charged to the voltage $\pm V_{Rail} = \pm(6.95\ V + V_{forward})$, where $V_{forward}$ is the diode forward velocity drop.

Thus every time the TTL signal switches, the charge on the capacitor changes by

$$Q = 2 * V_{Rail}/C_{CP} \tag{3.12}$$

where C_{CP} is the capacitance of the charge pump capacitor. The diode pair downstream of the charge pump capacitor acts as a current rectifier and one obtains a current $I = Q \times f_{TTL}$ where f_{TTL} is the frequency of the TTL signal. A transimpedance amplifier then converts the frequency to a voltage. Thus we obtain a voltage that is proportional to the input frequency. It turns out that we get a frequency to voltage conversion of 0.022 V/MHz and the full electronic schematic may be found in Appendix 3.

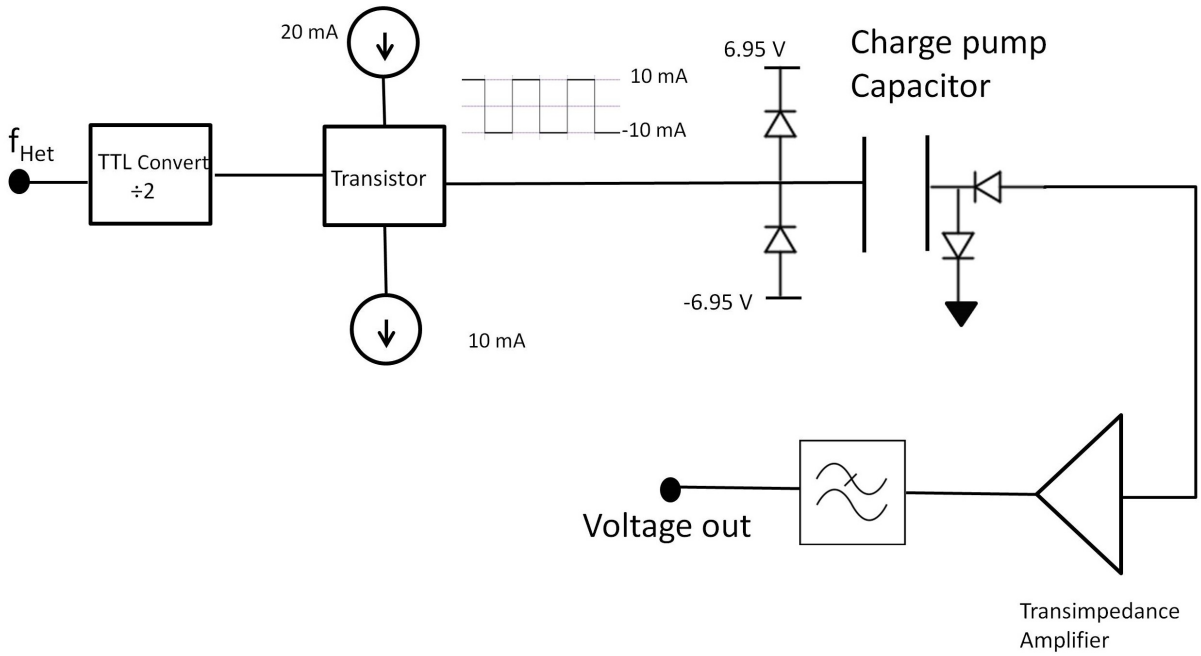

Figure 3.13: Illustration of frequency to voltage convertor. The incoming heterodyne beat is converted into a TTL signal. This TTL controls a high precision current source, providing either ± 10 mA. This current then alternately charges the charge pump capacitor to $\pm V_{Rail}$. A diode rectifier shunts the current to ground on one sign the TTL signal and to the transimpedance amplifier to the other. This yields the frequency dependent voltage which we use as an error signal to stabilize our lasers.

3.6 Frequency scanning

For certain applications, we will be chirping the frequencies of our lasers. For example, this is used in radiation pressure slowing as we wish to gradually address slower molecules.

The doppler shift is given by

$$\frac{\Delta f}{f_0} = -\frac{\Delta v_{long}}{c} \tag{3.13}$$

where f_0 is the resonant frequency at zero velocity and v_{long} is the velocity that we wish to address. Thus, the fractional frequency change is the same regardless of the laser in question.

It turns out that this chirp can be achieved by chirping f_{rep} and ensuring that all the $v'' = 0, 1, 2$ lasers frequencies follow the comb. The terms in Equations. 3.6 and 3.11 proportional to f_{rep} dominates over all of the other frequency terms due to the multiplication by the comb tooth integer. As an example, the frequency of the main cycling transition is 488.492 THz. Therefore, the red-shift to address a 100 m/s molecule is -163 MHz or a fractional change of -3.3×10^{-7}. Therefore, we need to add 330 Hz to $f_{rep,synth}$ in order to shift the laser frequencies be resonant with the 100 m/s molecules.

It turned out that to ensure the robustness of the lock while frequency chirping, we need to apply feed-forward to the scanned lasers. Feed-forward helps minimize the corrections that the feedback has to perform. Figure 3.14 illustrates this concept. The repetition frequency is changed by tuning $f_{rep,synth}$ by applying a voltage V_{chirp} to the frequency modulation input of the synthesizer. This changes the frequency lock-point of f_{rep} and drags all of the other optical lock points with it as well. The feed-forward is performed by applying a voltage proportional to V_{chirp} to the laser's frequency actuator. When the sign and magnitude of the scaling is tuned correctly, the feed forward voltage makes the laser perform the desired frequency scan and the frequency error signal will be minimized. The feed-forward is applied to the stabilization loops for f_{rep}, the Raman amplifier, and the $v'' = 1, 2$ vibrational repumps.

3.7 Putting them together.

In order to address all of the hyperfine manifolds, each vibrational frequency ($v'' = 0, 1, 2$) requires two additional frequency sidebands. The carrier frequency is tuned to the $G'' = 0$ transition whilst the additional sideband at +760 MHz addresses the $G'' = 1, F'' = 0$ manifold and the +774 MHz sideband addresses the $G'' = 1, F'' = 1, 2$.

For the 614 nm lasers, as we have sufficient power, these sidebands are generated with a single passed, two toned high speed AOM. However, as the ECDLs for the vibrational repumps have insufficient power, we end up with a string of injection locked diodes and tapered amplifiers. Each master diode injection locks a slave diode to provide light for the $G'' = 0$ hyperfine manifold. A small pickoff ($\sim$ 5 mW) of this light is then shifted up by a double passed AOM with a frequency dithered between 380 MHz and 387 MHz in order for the light to cover the $G'' = 1$ hyperfine manifold. The output of the double passed AOM is then used to injection lock a second slave diode. The slave diodes are made by Opnext with part number HL6385dg and typically provide $\approx$ 80 mW of power each. Both hyperfine components are combined and fiber-coupled to seed a tapered amplifier from Sacher (part number TPA-0650-0250) providing a total power of 200 mW for each vibrational repump. An added benefit is that all of the hyperfine components in each vibration now have the same polarization. Therefore, we can combine the $v = 1$ and $v = 2$ vibrational repumps with PBS cubes without loss. Combining the $v'' = 0$ light with the vibrational repumps is achieved with dichroic mirrors.

Figure 3.15 illustrates the lasers used in the longitudinal slowing configuration. In addition to the aforementioned sideband generation to address hyperfine states, a 5 MHz Pockel cell rapidly chops the polarization between σ^+ and σ^-. This is used to disrupt the optical pumping into dark Zeeman states and will be discussed in Chapter 5. Also resonant electro-optic modulators at 10 MHz are used to spectrally broaden the slowing light in order to aid with the efficiency of the longitudinal radiation pressure slowing (see chapter 6.

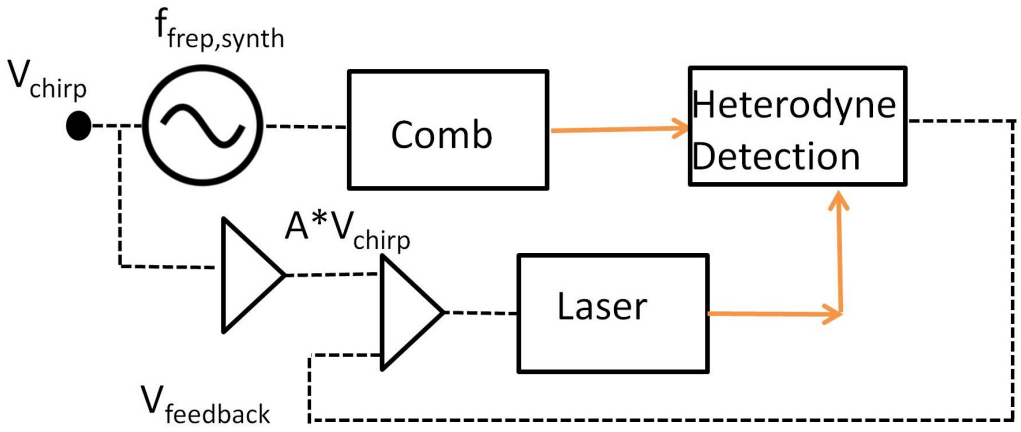

Figure 3.14: Example schematic of feed-forward applied to a laser locked to the comb. V_{Chirp} changes f_{rep}, pulling the laser lock point. V_{chirp} is scaled by a factor A in order to follow the changing lock point. $A * V_{Chirp}$ is added to the feedback voltage $V_{feedback}$.

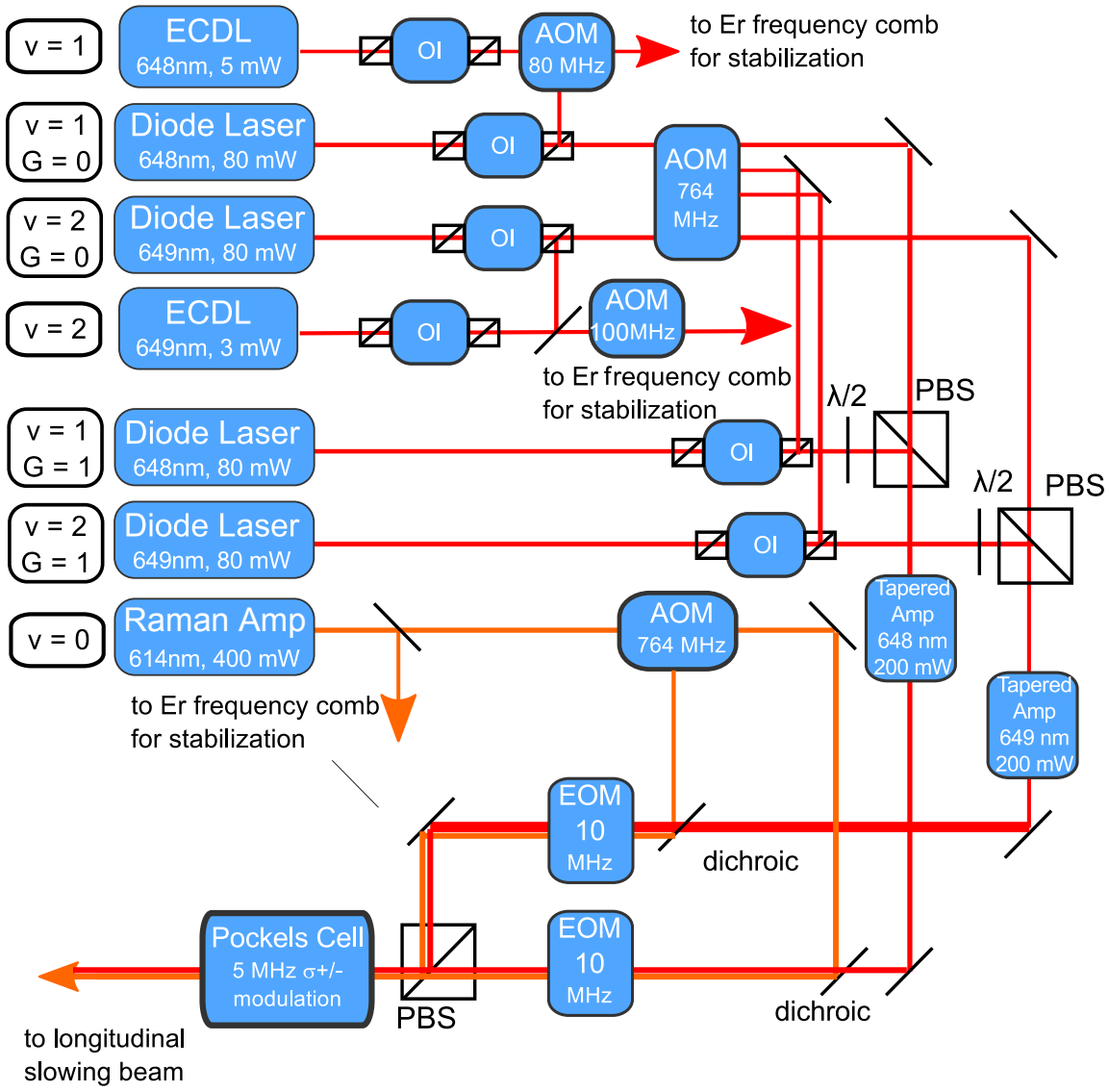

Figure 3.15: Longitudinal slowing laser setup for YO. Abbreviations: ECDL, external cavity diode laser; OI, optical isolator; AOM, acousto-optic modulator; EOM, electro-optic modulator; $\lambda/2$, half-wave retardation plate; PBS, polarizing beam splitter.

Chapter 4

Generating a Cold YO Beam

The two main sources to create a chemically diverse set of polar molecules are supersonic expansion jets and buffer gas cooled beams. While supersonic beams are easily able to generate rotationally cold and vibrationally cold samples, such beams have forward velocities of several hundreds m/s. This turns out to be fast for MOT trapping. Therefore, we produce a YO beam in a buffer gas beam formed in a cryogenic cell [48, 71, 124]. This generates a bright source of molecules in the correct quantum state with a modest forward velocity. Figure 4.1(a) shows a general schematic of the concept of the buffer gas beam. In this system, the buffer gas is fed into a cold copper cell and via collisions with the cell wall, the buffer gas comes to thermal equilibrium. The species of interest in turn thermalizes with the cold buffer gas. As rotational constants are on the Kelvin scale, temperatures on the order of 10 K are required in order to ensure sufficient population in the low rotational levels. The fractional population in each rotational state can be expressed as:

$$P(N) = \frac{1}{Z(8N+4)} e^{-\frac{BN(N+1)}{k_B T}} \tag{4.1}$$

where Z is the partition function. The resulting rotational population distribution for room temperature and 3.5 K are shown in 4.1(a) At 3.5 K, this yields a third of the population in the desired $N = 1$ state, which is a factor of 200 more than for a room temperature sample. Because vibrational states thermalize about 100-1000 times slower than rotational states [125], the buffer gas cooling is not as effective in themalizing these states. However, as

the vibrational spacing is on the order of a 1000 K, which is roughly the temperature of the ablation plume [126], there is still a significant amount of population in the desired $v = 0$ state

4.1 The Cryostat

The first ingredient to generating the YO beam is the cryostat. In the 2D MOT experiments, the system was cooled down via liquid helium and liquid nitrogen, whilst in the 3D-MOT, the system was upgraded to a pulse tube cooling system (CP2800 Cryomech) [127]. The pulse tube has good cooling power (600 mW at 4 K), has lower base temperature, 2.8 K as opposed to 4.2 K for a Helium-4 system, and will eventually pay for itself as it does not consume expensive liquid helium. The pulse tube has two cold heads, one at ≈3 K and the other at ≈40 K.

The main heat load on the cell is due to black body radiation. The power absorbed is given by:

$$P_{BB} = \sigma_{SB} T^4 A \tag{4.2}$$

where σ_{SB} is the Stefan-Boltzmann constant, T is the temperature of the environment and A is the surface area of the object. We therefore apply two layers of radiation shielding. The inner shield layer is thermally anchored to the 3 K cold head and the outer shield layer is tied to the 40 K cold head. The cell has an approximate area of 100 cm^2. If this were exposed to the room temperature outer vacuum can, we would put on a heat load of 4.5 W and would thus overwhelm the cooling power of the pulse tube. The inner shield at 40 K reduces the heat load to 1.4 mW, which the pulse tube can handle easily and is also negligible compared to the ∼100 mW of heat load due to the ablation and radiation pressure slowing lasers.

In contrast, the inner shield at 4 K's primary purpose is not to reduce the heat load but to ensure that the exiting buffer gas first bounces off the coldest surface possible. Otherwise, He atoms may bounce off the 40 K shield or a room temperature surface, heat up and destroy

the YO beam. Also, by coating the inner shield with activated charcoal, the helium buffer can be effectively cryo-pumped . We note that from work in other groups [128, 129] and experience from our own apparatus (see Section 4.3), the relative position of the shields and charcoal can make a significant difference to the beam's brightness, velocity and robustness.

There are some general construction techniques that we found useful. Everything in the cryostat that needs to be cold is made out of oxygen-free high thermal conductivity (OFHC) copper. As the name suggests, this grade of copper has high thermal conductivity at cryogenic temperatures: $\kappa = 630$ W/(m K) at 4 K and $\kappa = 1470$ W/(m K) at 40 K [130], which is more than an order of magnitude better than "regular" copper [131]. Indium is used for seals as they do not crack when cold or thermal cycled. For mating copper surfaces that need to be removable, the low temperature vacuum grease Apiezon N is liberally applied to the mating surfaces to increase the thermal conductivity [130]. Due to the differing thermal expansion coefficients, care must be taken when bolting the apparatus together as the differential expansion of different materials can pull the apparatus apart. To combat this, we use Belleville washers, which are conically shaped washers with a considerable amount of spring to them. By cranking down tightly, the washers spring out if the apparatus contracts and thus keep the pieces together. Thus we do not have to worry about building stacks of washers with different materials to compensate for differing thermal expansion.

4.2 The Cell

Figure 4.2 (a,b) shows photographs of the cryogenic buffer gas beam source. The 1st stage of the cell is made out of a 1.5"×1.5"×1.25" long OFHC copper rectangular cuboid. The cell cavity is formed by two through holes of 0.85 inch diameter. The total volume of the main cell is thus, $V = \pi r^2 * (l + w) - \frac{16}{3} r^3 = 18.8$ cm^3. The last term is the volume of the so called mouhefanggai shape formed by the intersection of the two cylinders of radius r. The beam exits through a 3 mm aperture.

YO molecules are formed via laser ablation of sintered Y_2O_3 pellets from Alfa-Aesar.

A Continuum Minilite I Q-switched laser produces ∼4 ns long pulses with energy 3 mJ at a 10 Hz rate at 532 nm. The ablation laser is focused onto the target by a 35 cm lens. The 30 mW average power is sufficient to raise the temperature of the main cell by about 0.5 K. From in cell absorption measurements, we estimate a YO density in the $N'' = 1$ state of 10^{10} cm^{-3} [71].

The helium buffer gas is continuously fed into the back of the cell via a 2.5 mm diameter copper tube. The buffer gas is pre-cooled by wrapping and soldering ≈60 cm of the feed line around a 1 inch diameter copper bobbin that is bolted to the 3 K cold plate. The helium flow rate is measured in units of standard cubic centimeter per minute (sccm), (i.e. the flow rate that would raise the pressure of a 1 cm^3 volume by 1 bar at 273 K). This corresponds to an number flow rate of 1 sccm = 4.4×10^{17} atoms/s. We typically run the experiment at 5-6 sccm which is controlled by a mass flow controller from Alicat Scientific.

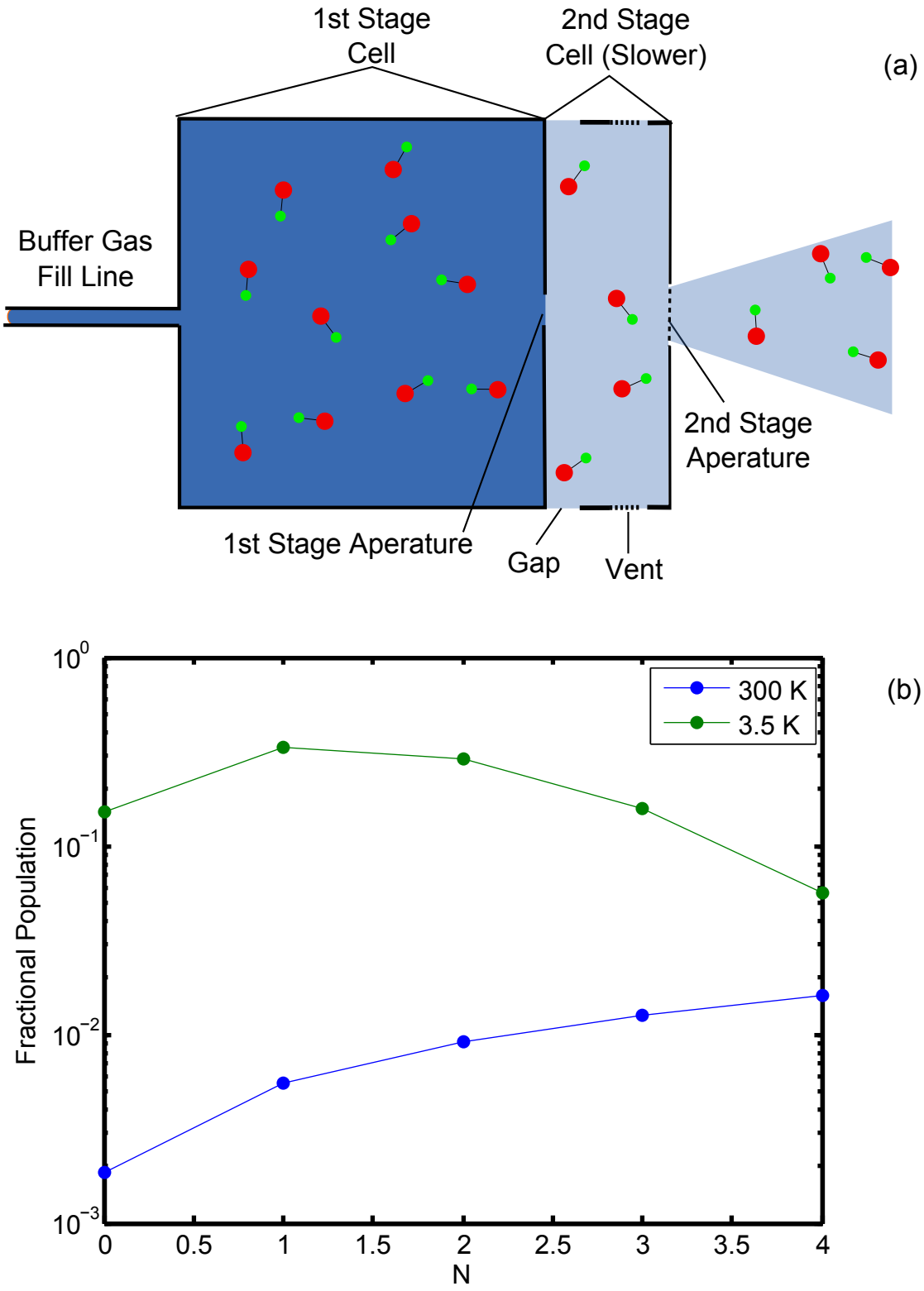

Figure 4.1: (a) Schematic of slowing cell. The YO molecules are themalized to the cold copper cell walls via He buffer gas. Higher helium density is represented with darker blue shading. The density in the slower cell is lower due to the gap and the vents. (b) Calculated Boltzmann rotational distribution for 300 K and 3.5 K. At the lower temperature, the fractional population in $N = 1$ is more than 200 greater than for room temperature.

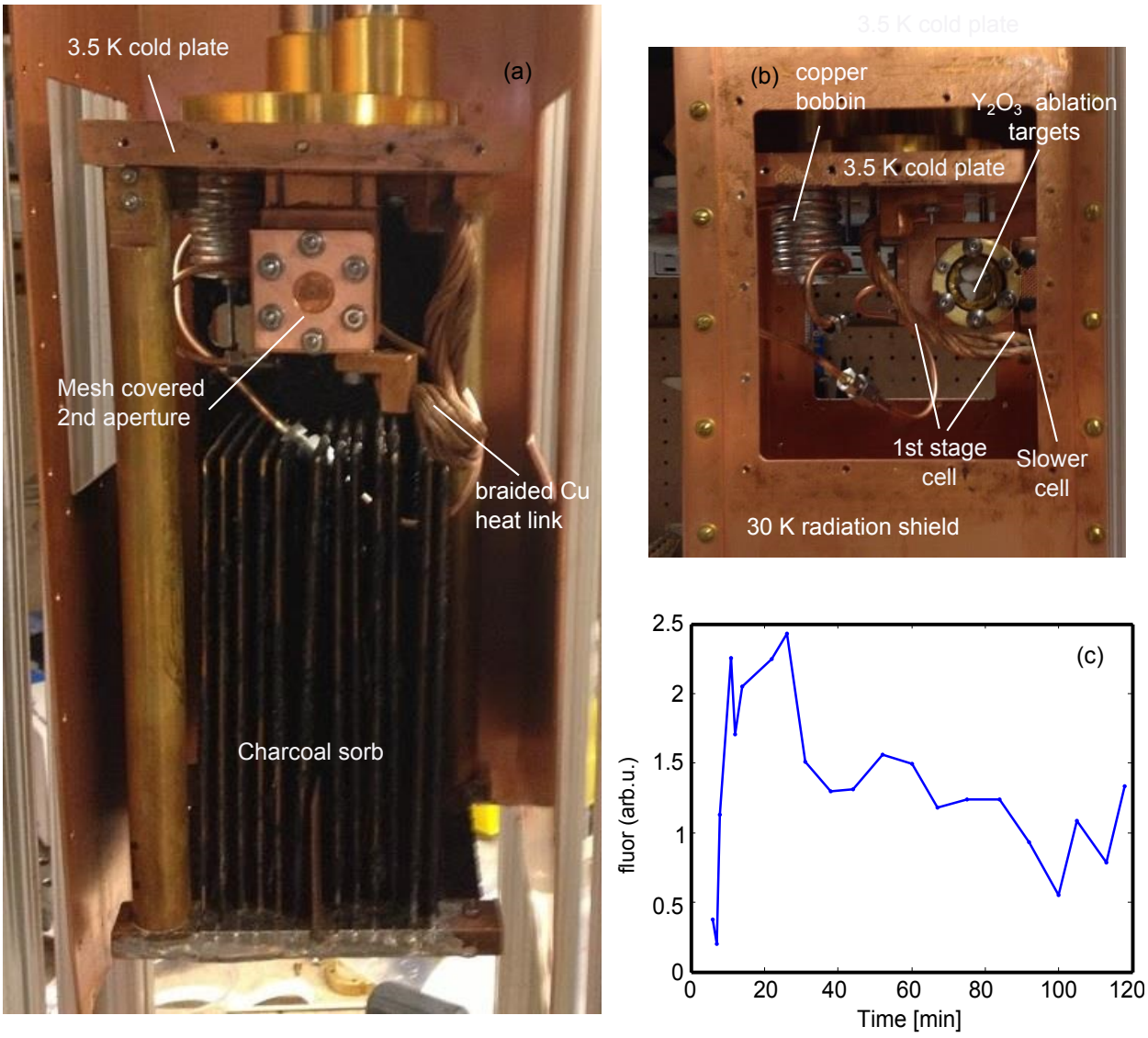

Figure 4.2: (a) Front view of slower cell and cryostat. The 9 mm diameter 2nd stage aperture is covered with a 30% transmissive copper mesh. The charcoal sorb is used to cryo-pump He buffer gas. (b) Side View of slower cell. Sintered Y_2O_3 pellets are laser ablated to form YO. The 1st stage cell is directly connected to the 3.5 K cold plate while the 2nd stage is connected via a copper braid heat link and thermally isolated from the 1st stage. (c) YO fluorescence measured ≈30 cm from the cell exit.

4.2.1 Gas flow regimes

Based on the helium flow rate and thus the stagnation buffer gas pressure, we can access three different gas flow regimes. These regimes can be characterized by the Knudsen number Kn

$$Kn = \frac{\lambda}{d} \tag{4.3}$$

where d is the aperture diameter and λ is the mean free path given by

$$\lambda = \frac{1}{\sqrt{2} n_{He} \sigma} \tag{4.4}$$

where σ is the He-He elastic cross section.

In the effusive regime, $Kn > 1$, implying that collisions are rare near the aperture. As a result the effusive beam is essentially a sampling of the thermal distribution in the cell. The forward velocity has the following distribution [49]

$$f_{beam}(v) = \frac{1}{2}\Big(\frac{m}{k_B T}\Big)^2 v^3 e^{-\frac{mv^2}{2k_B T}} \tag{4.5}$$

Integrating to find the exact velocity, we obtain

$$\bar{v}_{eff} = \int_0^\infty v f_{beam}(v) dv = \frac{3\pi}{8}\sqrt{\frac{8k_B T}{\pi m}} \tag{4.6}$$

On the other extreme, for Kn less than $\sim 10^{-2}$, inertial forces dominate over viscous forces and many collisions occur with the buffer gas near the aperture. As a result, the YO molecules experience a hydrodynamic boost as they exit the cell and take on the velocity of the carrier gas. This is known as the full hydrodynamic regime or in room temperature applications, the supersonic regime [47]. Here, enthalpy is converted into the forward velocity and is therefore able to cool the rotational degrees of freedom. Assuming that the temperature of the expansion is much lower than the in-cell temperature, the terminal forward velocity is [47, 132]

$$v_\infty = \sqrt{\frac{2k_B T_0}{m_{He}} \frac{\gamma}{\gamma - 1}} = \sqrt{\frac{5k_B T}{m_{He}}} \tag{4.7}$$

	v_{eff}	v_{∞}	v_{meas}
5 K	37 m/s	228 m/s	120 m/s
3 K	29 m/s	177 m/s	48 m/s

Table 4.1: Calculated forward beam velocities in effusive and supersonic regimes compared to measured velocities.

We note that since YO is the minority species in the expansion, the supersonic beam's properties are set by the buffer gas. As a result, since $m_{YO}/m_{He} = 26$, the velocity of the supersonic beam is much greater than that of the effusive beam given the same cell temperature. This is summarized in Table 4.1. It turns out that our original YO beam [71] was actually run in the so called partially hydrodynamic regime [133] as our measured center velocity was 120 m/s , which is intermediate between v_{eff} and v_{∞}. Due to the large forward velocity, buffer gas cells are not used in the hydrodynamic regime. In the effusive regime, the extraction efficiency is poor as any non-helium species will stick to the cell walls. Therefore buffer gas cells are typically run in the intermediate regime or partially hydrodynamic regime [129] with Kn between 0.01 and 1. However, for the 3D MOT, whose capture velocity is only $\sim$10 m/s, a slower beam is highly desirable and this is the subject of the next subsection.

4.2.2 Slower Cell

In order to further slow the beam, we attached an additional slowing cell [133, 134] to the 1st stage. This 2nd stage cell is deliberately made to be very leaky as shown schematically 4.1 (a). The 2nd stage cell is stood off 2.8 mm away from the main stage's aperture face. In addition, two rectangular vents on the side of the cell provide additional leakage and the beam exit aperture is 9 mm in diameter. The ratio of the slowing cell leak area to the main leak area (i.e. the aperture area) in our system is 50:1 . These leakages creates a pressure region intermediate between the cell and the low vacuum region of the rest of the cryostat. This yields a region with a mean free path on the order of several mm. Therefore,

the molecules experience several collisions on its way out, shedding some of their forward velocity. Copper mesh of various transparencies was placed on the side vents (40%) and the aperture (30%) in order to fine tune the intermediate pressure. The longitudinal doppler spectrum was measured 89 cm downstream of the cell and was fit using a Gaussian multiplied by the square of the velocity in order to account for transverse spreading of the beam.

$$f(v) \propto v^2 e^{-\frac{m(v-v_c)^2}{2k_B T}} \tag{4.8}$$

The result is a 48 m/s beam with a tempature of 8 K as shown in 4.3. This is more than a factor of 2 reduction in the beam velocity,

Photographs of the slowing cell are shown in Figure 4.2. The slowing cell is made of an OFHC copper block that is 0.38" long with the same 1.5" square face as the main cell. The aperture to aperture distance is 12.5 mm. A machine drawing of the cell is shown in Appendix 2. In order to prevent unnecessary heating of the slowing cell from the ablation laser, the slower is stood off by stainless steel washers (κ = 0.2 W/m.K) and is cooled via a flexible copper heat link, which is described in section 4.3.2 of Wesley Campbell's thesis [135]. This keeps the temperature of the slower cell ≈0.5 K lower than the main cell during operation. Our slowing cell was based very closely on the a design from the Doyle group at Harvard University and was presented in reference [134].

4.2.3 In-cell buffer gas density

To estimate the density of the helium buffer gas, we need to know the conductance of the aperture. In the viscous regime, the mean free path is much smaller than the aperture diameter, and the conductance in Liter/s is given by [136]:

$$C_{visc} = \frac{9.13 A_{ap}}{1-\xi} \xi^{\frac{1}{\gamma}} \sqrt{\frac{2\gamma}{\gamma-1}\frac{T}{M}(1-\xi^{\frac{\gamma-1}{\gamma}})} \tag{4.9}$$

where A_{ap} is the area of the aperture in cm^2, T is the temperature in K, $\gamma = \frac{5}{3}$ is the ratio of the specific heat of He at constant pressure to the specific heat at constant volume and

M is the atomic weight of He. The variable $\xi = \frac{P_{out}}{P_{in}}$, the ratio of the pressure outside vs inside the cell. However, for helium, for $\frac{P_{out}}{P_{in}}$ below the critical value of ≈0.49, ξ saturates to this critical value. This is indeed the regime that we are in as the pressure outside the cell should be much lower than inside.

Plugging these numbers into Equation 4.9, the conductance is

$$C_{visc} = 6.5 A_{ap} \sqrt{T} \tag{4.10}$$

which gives a value of 1.6 liter/s where we haveused values of T = 3.5 K, and $A = \pi(0.15cm)^2 = 0.07cm^2$. The exponential pumpout time is then given by

$$\tau_{pumpout} = V_{cell}/C_{visc} = 11.8ms. \tag{4.11}$$

Therefore at steady state, at a flow rate of 5 sccm, the number density of He atoms in the cell is

$$n_{He} = \tau_{pumpout} \times 5 \times 4.4 \times 10^{17}/V = 1.4 \times 10^{15} cm^{-3} \tag{4.12}$$

where V is the volume of the 1st stage cell.

4.3 Charcoal Cryopumping

Pumping out the buffer gas by a mechanical pump is difficult as the cell is enclosed two layers of radiation shielding, which makes the pumping speed very small. In addition, turbomolecular pumps has a poor compression ratio for helium gas. For example, for the Varian Turbo-V 70 [137], the ratio is 4×10^3. This makes it difficult to have a sufficiently good vacuum to make the YO beam.

With the temperatures that we can attain with our pulse tube refrigerator, cryopumping for any other gas is automatic. For example, the vapor pressure for neon at 4 K is less than 10^{-9} torr [49]. In contrast, at 4 K the vapor pressure of helium is still several hundred Pascal, and hardly any cryopumping occurs. However, it turns out that activated charcoal cooled to less than 10 K becomes an excellent cryopump for helium [131]. With

$\approx$100 cm^2 of 4 K, several hundred l/s worth of pumping power can be attained. In addition, the charcoal, due its porous nature, can adsorb several percent of its weight in helium at 4 K. This is of key importance due to the relatively high flow rates that we use.

To implement this, we glued the charcoal to the 4 K radiation shield with the Stycast 2850 epoxy [130]. In addition, to utilize the additional volume inside the cryostat, we built a set of 12 copper fins shown in Figure 4.2(a). These were connected to the 4 K cold plate via 1 inch diameter brass rods. As compared to only coating the inner 4 K radiation shield with charcoal, these additional fins increased the charcoal sorb area by a factor of 5 with a sorb area of 900 cm^2 . The temperature of the charcoal attached to the fins is 8 K. We note that without these additional fins, the overall adsorption capacity was initially a limiting factor to the run time to the experiment, where we initially obtained a continuous run time at 6 sccm of approximately 15 minutes. The addition of the fins gave us a run time of about 2 hours as shown in Figure 4.2 (c) making it feasible to run the experiment.

As the beam quality would degrade after about 2 hours of running, particularly in the lower end of the velocity distribution, we have to regenerate the charcoal sorb. To do this, we let the cryostat warm up by turning off the pulse tube. This process is accelerated as the helium pressure rises as it is desorbed and acts as a convective exchange gas to room temperature. The cryostat temperature rises to about 40 K very rapidly and we use the Turbo-V 70 turbo molecular pump at low speed to pump away the excess helium. A gate valve installed between the cryostat and the rest of the apparatus allows us to isolate the two vacuum regions and protects the MOT apparatus from this burst of helium. This allows for ablation target changes without exposing the MOT region to atmosphere.

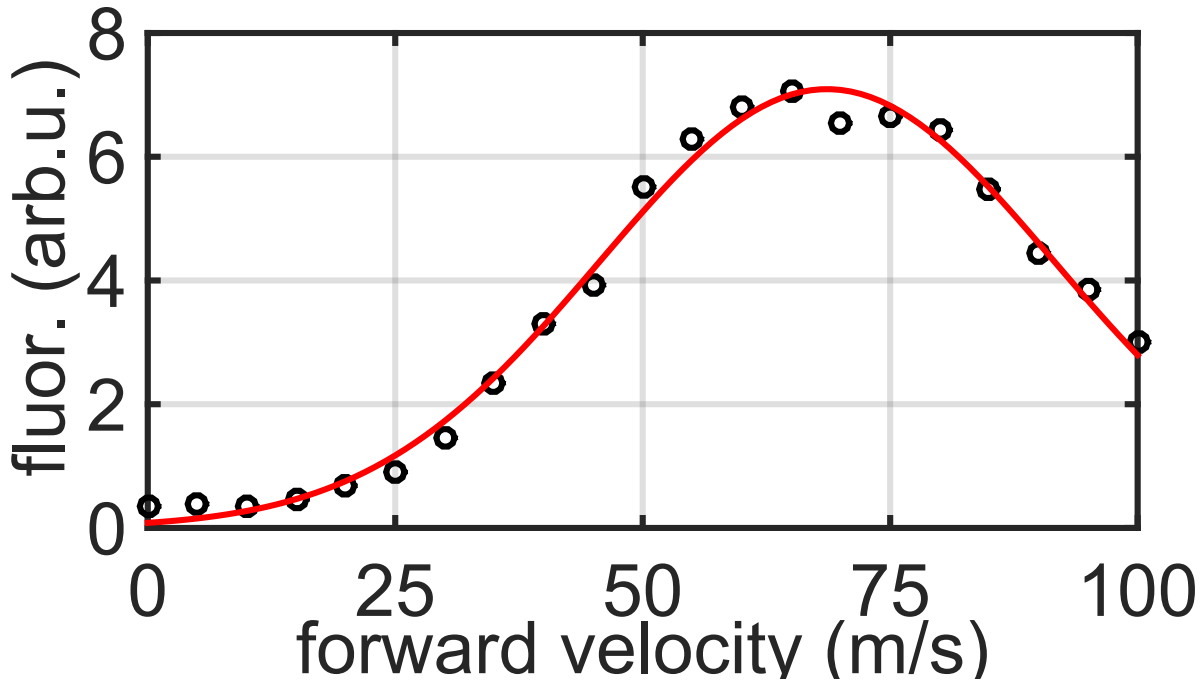

Figure 4.3: Forward velocity distribution of YO as measured 89 cm from the cell exit via light induced fluorescence. The solid line is a fit to a Gaussian (with center longitudinal velocity of the beam at 49 m/s and a temperature of 8 K) multiplied by the square of the forward velocity to account for the transverse velocity spread.

Chapter 5

Magneto-Optical Trapping of YO

5.1 Introduction to Laser Cooling

Laser cooling of atoms and ions has had a long and venerable history starting with the first proposals for Doppler cooling in 1975 [138,139] and its first demonstration in 1978 [140]. Laser cooling atoms has become a cornerstone of atomic physics. However, it was not until 2010 that the first molecule was laser cooled [70].

Building on laser cooling, the magneto-optical trap (MOT) was first demonstrated in 1987 in Bell Laboratories [141] by using inhomogeneous magnetic fields to use the same large forces available from the photon cycling already exploited in Doppler cooling to spatially confine neutral atoms.

To gain an quantitative understanding of these two processes, we consider a molecule moving with velocity $\mathbf{v}$. Following the notation of [73], the molecule has a set of states labelled with ψ_l and ψ_u (for lower and upper) and the transitions have angular frequency $\omega_{u,l}$ and natural linewidth Γ. Multiple circularly polarized laser beams, each of which may contain several frequency sidebands, illuminate the molecule with frequency ω_p, intensity I_p and propagate in the $\hat{\mathbf{p}}$ unit vector direction . For each transition, there is a set of detunings associated with each laser beam or frequency side band $\delta_{u,l,p}$. The saturation intensity I_s for each transition is given by

$$I_s = \frac{\pi h c \Gamma}{3\lambda_{u,l}^3} \tag{5.1}$$

where $\lambda_{u,l}$ are the transition wavelengths. The fractional population in each state N_l, N_u will then be governed by the following rate equations

$$\dot{N}_l = \Gamma \sum_u r_{l,u} N_u + \sum_{u,p} R_{l,u,p}(N_u - N_l) \tag{5.2a}$$

$$\dot{N}_u = -\Gamma N_u + \sum_{l,p} R_{l,u,p}(N_l - N_u) \tag{5.2b}$$

where $r_{l,u}$ are the branching ratios calculated in Sections 2.7. The excitation rates $R_{l,u,p}$ are given by [1, 73]:

$$R_{l,u,p} = \frac{\Gamma}{2} \frac{r_{l,u} s_p}{1 + 4\left(\frac{\delta_p - 2\pi k_p \hat{\mathbf{p}}\cdot\mathbf{v} - \Delta_{u,l}^{Zeeman}}{\Gamma}\right)^2} \tag{5.3}$$

where $k_p = \frac{2\pi}{\lambda}$ are the laser's angular wavenumber $\Delta_{u,l}^{Zeeman} = (\mu_u - \mu_l)B/\hbar$ is the differential Zeeman shift between the two states. (The magnetic moments, $\mu_u - \mu_l$ are calculated in Section 2.3) and the on-resonance saturation parameter s_p is given by:

$$s_p = \frac{I_p}{I_s} \tag{5.4}$$

To provide the inhomogeneous magnetic field, a quadrupolar magnetic field is used and the spatially dependent field can be written as:

$$\mathbf{B} = A(\frac{x}{2}\hat{\mathbf{x}} + \frac{y}{2}\hat{\mathbf{y}} - z\hat{\mathbf{z}}) \tag{5.5}$$

The on-resonance saturation parameter s_p is related to the Rabi frequency $\Omega_{u,l}$ by $r_{l,u} s_p = 2|\Omega_{u,l,p}|^2/\Gamma^2$.

Because spontaneous emission is isotropic in free space, this process leads to no force on average. Therefore, the force is the sum of the excitation due to each laser beam multiplied by the photon momentum, i.e.

$$\mathbf{F} = \hbar \sum_{l,u,p} k_p \hat{\mathbf{p}} R_{l,u,p}(N_l - N_u) \tag{5.6}$$

It is the imbalance of these scattering rates from counter-propagating beams as a function of velocity and magnetic field that leads to the damping and restoring forces associated with doppler cooling and magneto-optical trapping.

5.1.1 2 Level Atom

For a qualitative understanding of how laser cooling works, we assume that the magnetic field is zero and the molecule is a 2-level system. We first apply a single frequency laser counterpropagating to the velocity **v** of the atom.

The force exerted on the atom is given by the stimulated absorption rate multiplied by the momentum of the photon and can be written as

$$\mathbf{F} = \Gamma \hbar k_p \bar{N_u} = \hbar k_p \frac{\Gamma}{2} \frac{s_p}{1 + s_p + 4\left(\frac{\delta + k_p v}{\Gamma}\right)^2} \tag{5.7}$$

where $\bar{N_u}$ is the steady state population obtained by solving the rate equations. As expected, this force saturates to $F = \hbar k \frac{\Gamma}{2}$ at large s_p.

If we added an additional laser beam to the system that is copropagating with the motion of the atom, we can solve the rate equations (Equation 5.2) to obtain the optical molasses force [142]:

$$F_{1D,OM} = \frac{8 s \Gamma k_p v \delta}{16(k_p v)^4/\Gamma^2 + 8(k_p v)^2(1 + s - 4\delta^2/\Gamma^2 + (1 + 4\delta^2)((1 + 2s)\Gamma^2 + 4\delta^2)} \tag{5.8}$$

As the denominator is positive definite, the sign of this force is only dependent on kv and so we see that if δ is negative, this yields a damping force for all velocities. This is the basis of doppler cooling. In figure 5.1 we plot this damping force for various saturation parameters as a function of velocity. We note that with increasing saturation parameter, as the overall scattering rate increases, the cooling force increases and due to the power broadening, and the overall width of the cooling force also increases.

To first order in $k_p v$ the force is linear with respect to v and we can define the damping coefficient β/m as:

$$\frac{F}{m} \approx -\frac{\beta}{m} v = \frac{8 \hbar s \Gamma k_p^2 \delta}{m(\Gamma^2 + 4\delta^2)(1 + 2s + 4\delta^2/\Gamma^2)} v \tag{5.9}$$

In the limit of $s \ll 1$ this is consistent with conventional laser cooling theory [1, 143], which is derived by adding the forces from each of the counterpropagating beams. This turns out

to be

$$F \approx \frac{8s\hbar k_p^2 \delta}{m\Gamma(1+s+4\delta^2/\Gamma^2)^2} v \tag{5.10}$$

5.1.2 MOT Forces

The doppler shift $k_p v$ and the Zeeman shift Δ^{Zeeman} affect the populations and hence the forces (Equation 5.2) in a mathematically equivalent manner. Therefore, we may replace kv with $\frac{A(\mu_u - \mu_l)}{\hbar}$. Applying the same linearization process for a stationary molecule about z =0, the MOT force is therefore approximated as

$$\frac{F}{m} \approx -\omega_z^2 z = \frac{8\hbar s\Gamma k_p(\mu_u - \mu_l)A\delta}{\hbar m(\Gamma^2+4\delta^2)(1+2s+4\delta^2/\Gamma^2)} z \tag{5.11}$$

Therefore, if the ω_z^2 term is positive, the molecule will be confined about $z = 0$ and will perform harmonic oscillation with secular frequency $\omega_z/(2\pi)$. For the quadrupole geometry, the other two trapping frequencies are given by

$$\omega_x = \omega_y = \frac{1}{\sqrt{2}}\omega_z. \tag{5.12}$$

Similar to doppler cooling, for small displacements we may linearize this restoring force and obtain in the z direction,

$$F_z = -\beta v - m\omega_z^2 z \tag{5.13}$$

where the secular square of the secular frequency can be expressed as

$$\omega_z^2 z = \frac{(\mu_u - \mu_l)A)}{\hbar k}\beta \tag{5.14}$$

This is the familiar first order differential equation describing a damped harmonic oscillator.

To ensure that the MOT forces confine and not blow up our sample we must also pay attention to the polarization of the light. Figure 5.2 (a) illustrates a typical MOT transition, (a so called type I MOT [141]) . The upper state has more total angular momentum than the lower state, i.e. $J' = J + 1$. A laser beam with σ^- circular polarization propagates towards the left and may only drive the $m_J \rightarrow m'_J = m_J - 1$ transition. The σ^+ laser beam

propagating to the right only drives the $m_J \rightarrow m'_J = m_J + 1$. As both lasers are red detuned to facilitate doppler cooling, an atom at a position of positive B-field will preferentially absorb from the leftwards propagating beam as shown in 5.2 (a). Similarly, an atom experiencing a negative B field will preferentially absorb from the rightward propagating beam. This results in the net confining force in Equation 5.11.

Figure 5.2 (b) shows a schematic of the so called type-II MOT. Such MOTs operate on either $J \rightarrow J' = J - 1$ or $J \rightarrow J' = J$ transitions. Due to the requirement of maintaining rotational closure, all previously laser cooled molecules [70, 71, 75] have used such Type-II MOT transition. The type-II MOT is complicated by optical pumping into Zeeman sublevels dark to the restoring beam leading to zero confinement. For example in panel b, it turns out that this optical pumping leads to a population imbalance between the $m_J = \pm 1$ levels that exactly cancels the ratio of the absorption rate between the confining and anti-confining beam thus leading to zero confinement [74]. (The $m_J = 0$ while dark to both beams in 1D is remixed via orthogonal MOT beams.)

However if the ground state Zeeman sub-levels are aggressively remixed, then the combination of the red detuning and polarization selection rules will lead to the MOT confining force similar to the Type-I case as shown in Figure 5.2 (b). In this work, this remixing is achieved by rapidly switching the circular polarization of the MOT beams in phase with the direction of the magnetic quadrupole field [71]. This is described in further detail in sections 5.2.3 and 5.2.6. We note that for polar molecules, this remixing can also be achieved by re-projecting the molecular's angular momentum by applying a pulsed electric field non-parallel to the magnetic field [68].

Despite the expectation of zero confinement in type-II MOTs without additional remixing mechanisms, this trapping scheme has been demonstrated in several atomic systems [144–147] and was also demonstrated in the SrF 3D MOT system [72, 74]. A theoretical explanation was put forth by Tarbutt in 2014 [73] for which the non-zero Zeeman shift in the upper state breaks this symmetry and yields the weak confining forces.

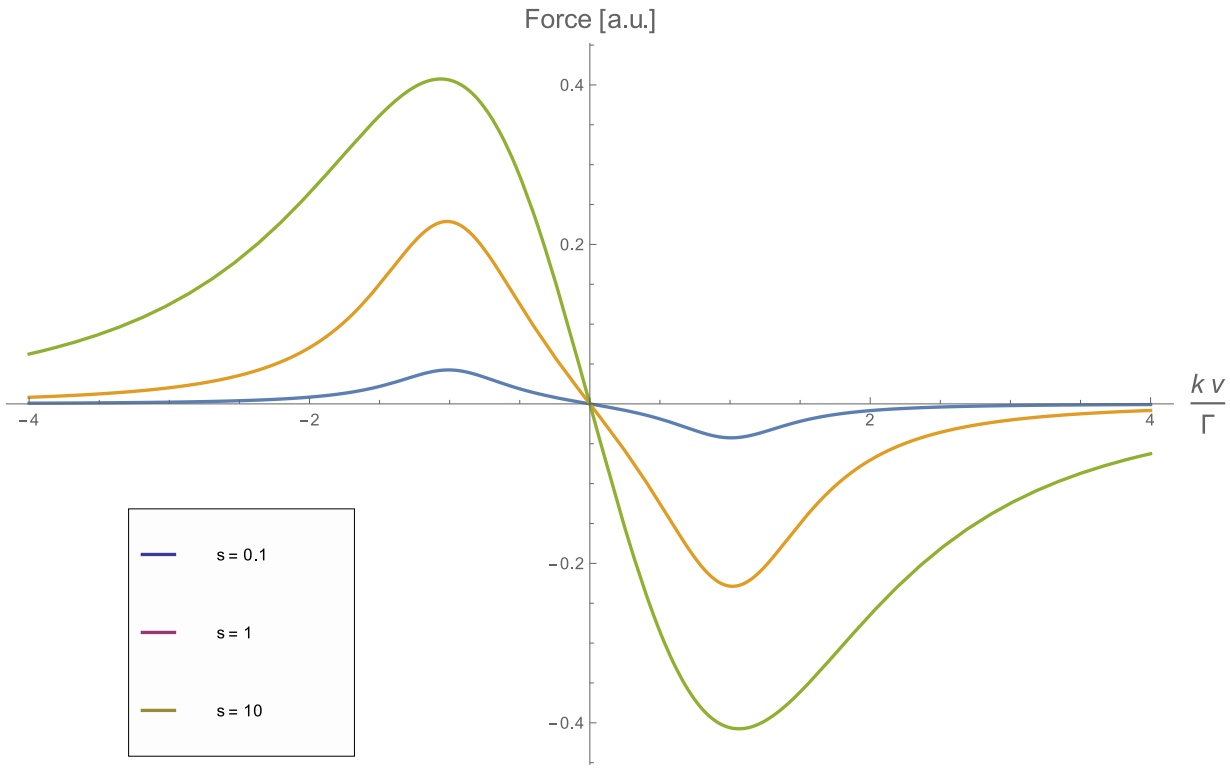

Figure 5.1: Force on a 2 level system by two red detuned counterpropagating lasers.

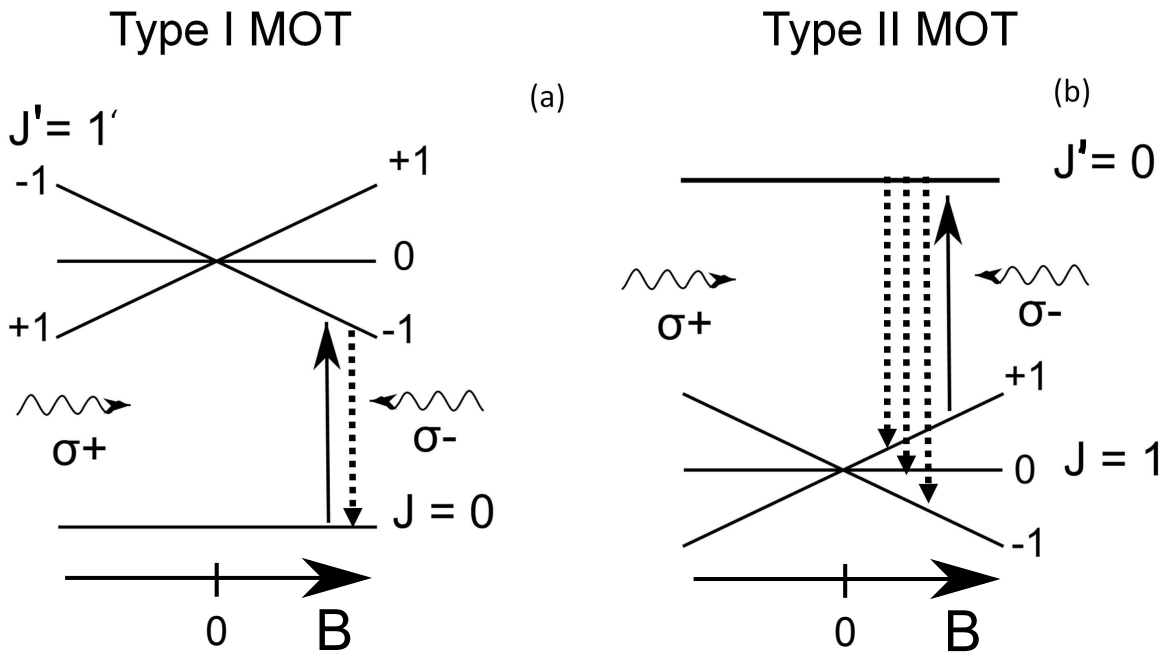

Figure 5.2: (a) Illustration of Type I MOT, where transitions have the form of $J \to J' = J+1$. Illustration of Type II MOT, where transitions are of type $J \to J' = J - 1$.

5.1.3 Doppler Temperatures

Equation 5.13 would imply that the temperature of the sample would converge to absolute zero and is clearly nonphysical. The finite temperature is due to random momentum kicks due to spontaneous emission. The momentum drift due to this process is zero as the spontaneous emission is spatially isotropic. The evolution of the momentum can be thought of as a random walk, thus the variance of the momentum scales linearly with the number of emission events. Following from reference [148], the rate of change of the momentum variance is

$$\frac{d < p_x^2 >}{dt} = 2\hbar^2 k^2 \sum_{l,u,p} \hat{\mathbf{p}} R_{l,u,p}(N_l - N_u) \tag{5.15}$$

The heating can then expressed as

$$\frac{dQ}{dt} = \frac{1}{2m} \frac{d < p_x^2 >}{dt} \tag{5.16}$$

Balancing the cooling rate $-\beta \mathbf{v} \cdot v$ at low saturation and for $\delta = -\Gamma/2$, the final temperature is given by

$$T_{doppler} = \frac{\hbar \Gamma}{2k_B} \tag{5.17}$$

$T_{doppler}$ represents the minimum temperature attainable by Doppler cooling and for the YO molecules' main cooling transition $X^2\Sigma^+ \rightarrow A^2\Pi_{1/2}$, this turns out to be 116 μK.

The root mean squared velocity this corresponds to is

$$v_{doppler} = \frac{\hbar \Gamma}{2m} = 9.5 cm/s \tag{5.18}$$

Two other special laser cooling temperature can be derived [1]. The first is the so called Capture Limit. This corresponds to the velocity at which the doppler shift is equivalent to the natural linewidth. I.e. $v_c = \Gamma/k$, this yields a temperature of

$$T_c = \frac{m\Gamma^2}{k_B k^2} \tag{5.19}$$

This yields values of $v_c = 3$ m/s and $T_c = 100$ mK. This yields an order magnitude estimate of the maximum trappable velocity.

The much colder limit is given by the recoil velocity due to a single photon, $v_r = \hbar k/m$. This temperature is given by

$$T_r = \frac{\hbar^2 k^2}{k_B m} \tag{5.20}$$

This evaluates to $T_r = 500$ nK and $v_r = 6.2$ mm/s. Reaching sub-Doppler temperatures involve Sisyphus type cooling [1,149], distinct from the Doppler cooling described above and was observed in laser cooling experiments in SrF in [70].

5.2 A 2D MOT for molecules.

In this section, we will describe the experiments on the transverse laser cooling and magneto-optical trapping of the a cryogenically produced buffer gas beam of YO [71].

5.2.1 Recap of YO structure

We briefly recap the salient features of the YO structure used in optical cooling. The main optical cycling transition is the $X^2\Sigma^+ \rightarrow A^2\Pi_{1/2}$ at 614 nm. The natural lifetime of this transition $\Gamma^{-1} = 33$ ns allows for rapid cycling. Due to the highly diagonal Franck-Condon factors as calculated in section 2.5, vibrational branching into the $A^2\Pi_{1/2}$ state is limited. We therefore apply repump lasers at 648 nm and 649 nm to repump the $X^2\Sigma^+, v'' = 1 \rightarrow A^2\Pi_{1/2}, v' = 0$ and the $X^2\Sigma^+, v'' = 2 \rightarrow A^2\Pi_{1/2}, v' = 1$ as shown in Figure 5.3 (a).

Fig. 5.3 (b) shows the rotational and hyperfine structure. Parity and angular momentum selection rules prevent decays to all rotational states except the $N'' = 1$ state (see Section 2.6). To address all of the hyperfine states in the ground electronic state (see section 2.3, in addition to the frequency tuned to the $X^2\Sigma^+, G'' = 0 \rightarrow A^2\Pi_{1/2}$ transition, 2 additional frequencies ~ 750 MHz are used to address the $G'' = 1, F'' = 0$ and the spectroscopically unresolved $G'' = 1, F'' = 1, 2$ states. The hyperfine structure is similar across $v'' =$ 0-2 (see Table 2.1), hence the same frequency sideband structure can be used to address all vibrational states.

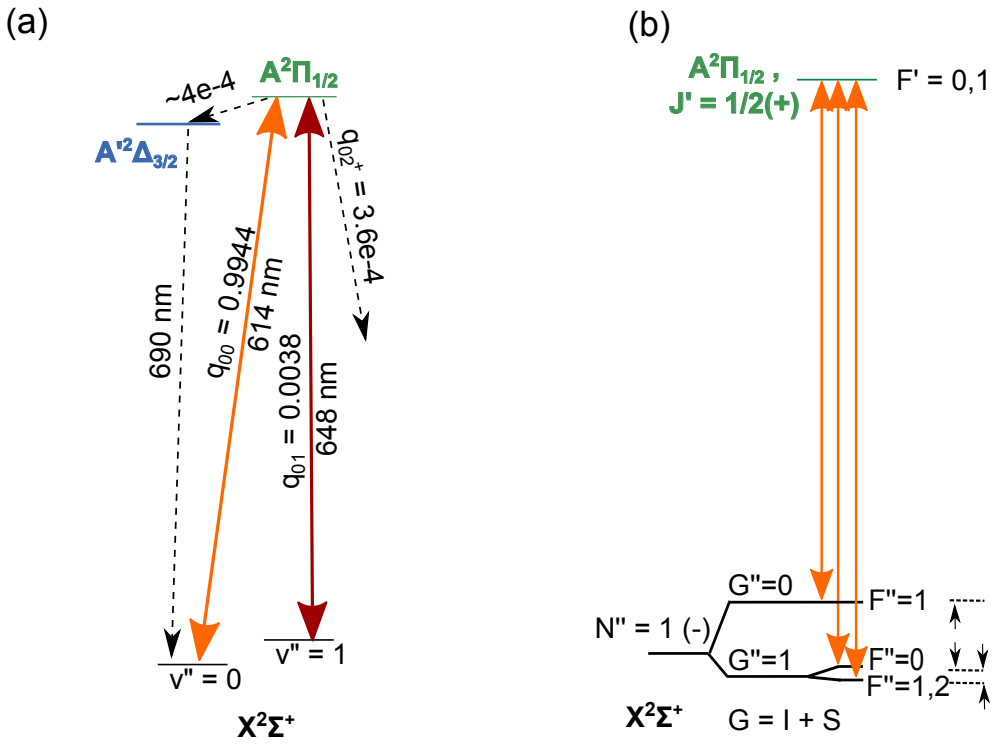

Figure 5.3: (a) Rovibronic structure. (b) Hyperfine structure of the $X^2\Sigma^+$ state. Orange solid arrows show the three frequency components used to excite the hyperfine components.

5.2.2 Beam Apparatus

The initial YO molecule beam is produced via a cryogenic buffer gas beam source, which is thermally anchored to a 4.5 K liquid helium reservoir described in Chapter 4. The YO density in the $N'' = 1$ state is measured to be $\sim 10^{10}$ cm^{-3} with $\sim 10^{10}$ molecules produced per pulse. The forward velocity of the beam is measured via doppler shift fluorescence spectroscopy with mean velocity of 120 m/s and FWHM of 40 m/s. A 2.5 mm aperture is placed 130 mm away from the buffer gas cell aperture. This collimates the beam and results in a transverse temperature of 25 mK.

After the collimating aperture, the YO molecules fly through a 10 cm interaction region where they interact with the cooling lasers, set up in a retroreflected multipass configuration. The molecules fly through the ∼3 mm (FWHM) diameter cooling lasers 11 times, which corresponds to a 275 μs interaction time. The multipass setup in each transverse dimension consists of a pair of mirrors and $\lambda/4$ waveplates. This ensures the correct polarization for MOT confinement. We use a rectangular baseball geometry coil to provide the quadrupole magnetic field. This will be discussed in further detail in Section 5.2.5.

After the interaction region, the molecules are allowed to free fly a further 30 cm to the detection region. This detection region consists of a multipass clean-up beam consisting of the $v'' = 1, 2$ repumps followed by a retroreflected detection laser consisting of the same light used for the laser cooling. The fluorescence is imaged onto a CCD camera in the y dimension. The temperature is calculated via

$$T_x = \sigma_{v_x}^2 m_{YO}/k_B. \tag{5.21}$$

Due to the long free flight region after the interaction region, the spatial profile of the YO beam is dominated by the variance of the velocity, $\sigma_{v_x}^2$. Monte-Carlo calculations using the magneto-optical forces are used to determine the spatial and velocity profile of the YO beam; this allows us to assign a temperature based on the beam profile.

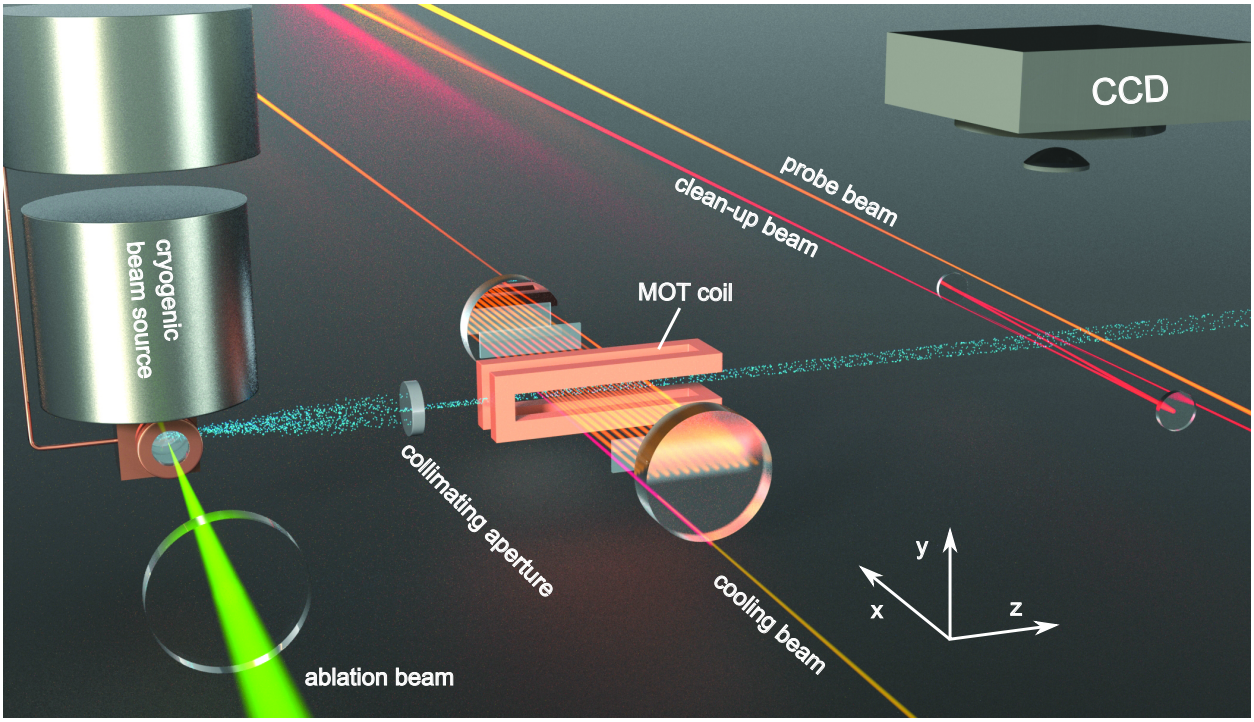

Figure 5.4: Depiction of the MOT/Laser Cooling apparatus in the 1D implementation. An additional multipass in the y direction is implemented for the 2D MOT. (Image created by Brad Baxley)

5.2.3 Polarization chopping and Doppler cooling

The last piece in the puzzle to obtain optical cycling is the repumping of Zeeman dark states. For the $J'' \rightarrow J' = J'' + 1$ type II MOTs which are required for rotational closure, optical pumping into dark Zeeman states is guaranteed. The first molecular cooling experiment [69, 70] used an off axis magnetic field to Larmor precess the molecules out of the dark Zeeman sublevel. However, YO is not amenable to this technique as the $G'' = 0$ hyperfine has a very small Zeeman shift (Figure 5.8 (a)) at the relevant magnetic fields. Therefore, we use the method of polarization chopping in order to repump the Zeeman sublevels.

From the analysis of Berkeland and Boshier, it turns out this technique works efficiently when the polarization is modulated at frequency of order the natural linewidth of the transition [150]. The polarization chopping is done with a Pockel's cell and a $\lambda/4$ waveplate. This yields alternately σ^+ and σ^- light. The cold YO beam is sent through the cooling multipass as described in the previous section, with each $v'' = 0$ laser frequency component detuned by $\delta = -2\pi \times 5$ MHz. We see that the final transverse temperature [1] monotonically decreases with increasing chopping rate as shown in Figure 5.5. The cooling rate settles at a chopping rate $\sim$5 MHz consistent with the analysis of Reference [150].

5.2.4 Doppler cooling of YO

With all the pieces in place for optical cycling, we consider the Doppler forces that the YO molecule experiences. To calculate the cooling and trapping forces fully, we need to take into account 44 zeeman states, 15 optical frequencies and time dependant polarizations. and solve Equation 5.2. However, certain simplifications turned out to satisfactorily model the system and match experimental data. The $X^2\Sigma^+$ state was modelled with only 5 states. The first state represents the $v'' = 1, 2$, the second represent the $v'' = 0, G'' = 0$. For this only the

[1] The initial transverse temperature is 15 mK here due to a different collimating. All subsequent experimental data in this chapter has an unperturbed temperature of 25 mK

614 nm light with carrier frequency, f_{YO} addresses this state. The last three states represent the $G'' = 1, F'' = 0, 1, 2$ manifolds respectively. These three states are addressed by the two frequency components at $f_{YO} + 760$ MHz and $f_{YO} + 774$ MHz to address the $F'' = 0$ state and the $F'' = 1, 2$ respectively. We note that the two-toned AOM also puts on unintended frequency sidebands at $f_{YO} + (2 \times 760 - 774)$ MHz and at $f_{YO} + (2 \times 774 - 760)$ MHz. These sidebands have a factor of 10 less power than the intended sidebands but must be taken into account in order to correctly model the cooling and MOT forces. With a saturation parameter of 20 we can calculate the optical molasses forces. In panel a, we see that cooling is least maintained for all velocities. Due to the spin-rotation and the dipolar hyperfine interaction, there is a $\sim 4\ \Gamma$ splitting between the $F = 0$, and $F = 1, 2$ manifolds, leading to the more complex shape of the optical molasses force compared to a simple 2 level system.

In panel (b), the damping coefficient $\frac{\beta}{m_{YO}}$ is plotted as a function of the laser detuning. Here we see an even greater departure from the typical two level system's behaviour where there are regions in the frequency space for which negative detuning leads to heating and positive detuning leads to cooling, the opposite of the expected behaviour. In the case of red-detuning, this occurs when the frequency sideband used to originally address the $F'' = 1, 2$ manifold is detuned by more than $1.5\ \Gamma$, it ends up being closer to the $F = 0$ transition. As the laser frequency is now in effect blue-detuned with respect to this transition, it yields a net heating effect.

Figure 5.7 (a) shows the transverse YO beam spatial profile under various conditions. The fluorescence curve (i) shows the unperturbed beam with a transverse temperature of 25 mK. Turing off the $v'' = 1, 2$ repumpers in both the clean up beam and the interaction beam curve(ii) leads to severe depletion as expected. Curves (iii) shows doppler cooling where we red detune all of the $v'' = 0$ laser frequencies by $\delta = -2\pi \times 5$ MHz and as a result the spatial distribution narrows and the temperature decreases to 10 mK. In order for the vibrational repumps to work at maximum efficiency, they are all left at resonance. Curve (iv) shows the effect of blue detuning the lasers to $\delta = +2\pi \times 5$ MHz and we as expected heat

the beam to 60 mK. (b) Shows the final temperature T_x as a function of laser detuning. We find the optimal cooling occurs at $\delta = -2 \times 5$ MHz. In addition, due to the closely spaced hyperfine levels, cooling can occur at apparent positive detunings.

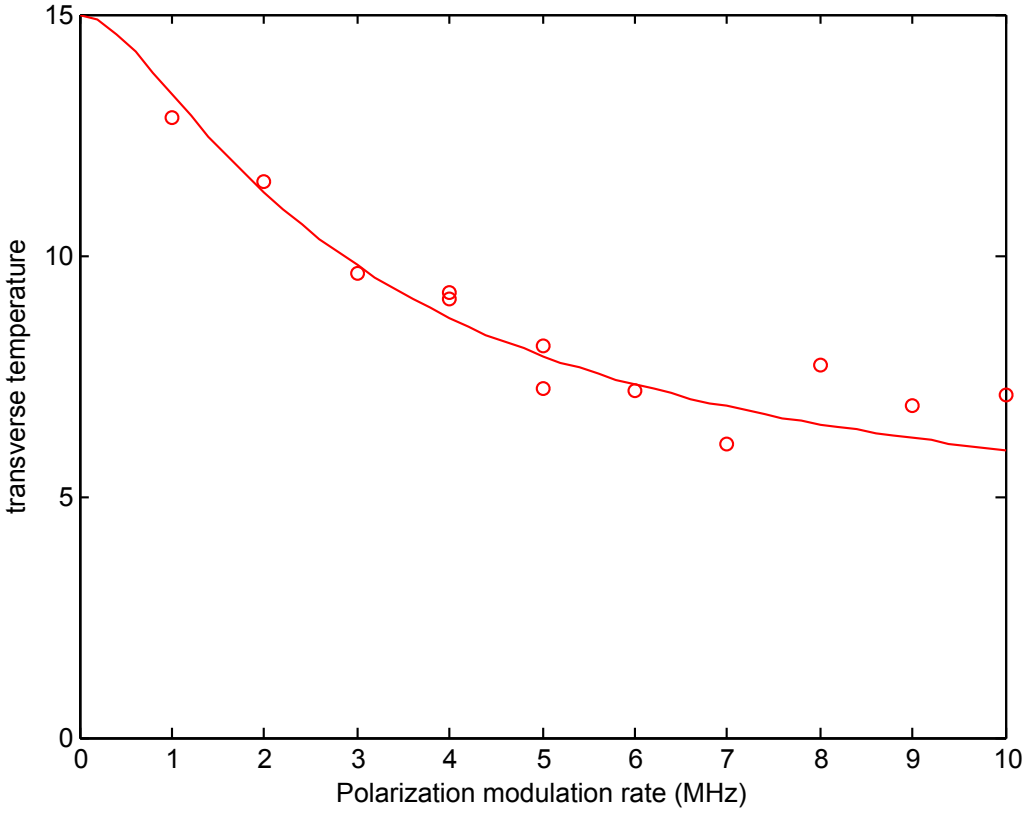

Figure 5.5: Temperature after Doppler cooling as a function of polarization chopping rate.

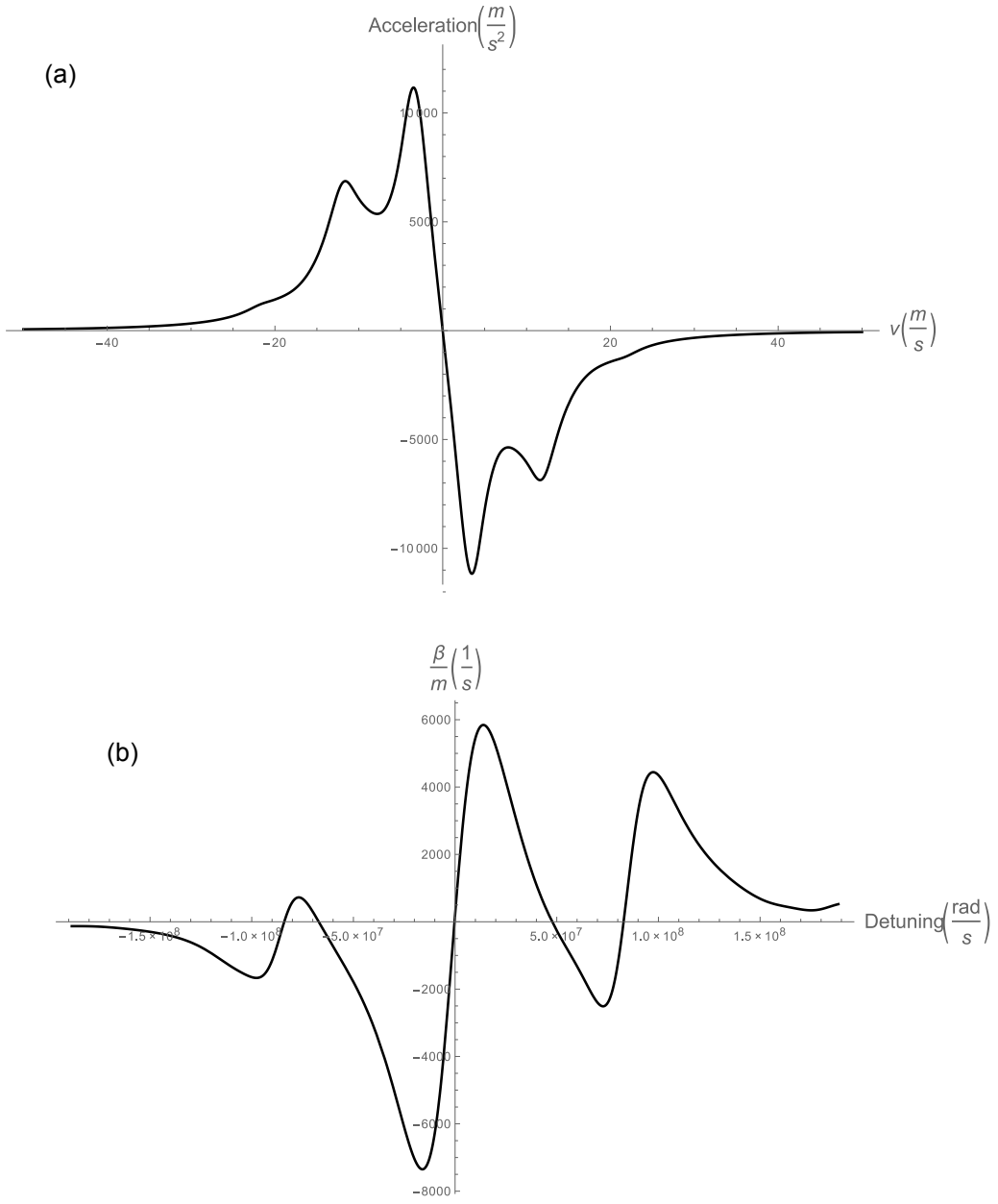

Figure 5.6: (a) Acceleration due to optical molasses on YO molecule with saturation parameter = 20 and laser detuning for each level of -Γ = -5 MHz. (b) β/m_{YO} as a function of laser detuning. Note that there are regions of blue (red) detuning which cool (heat).

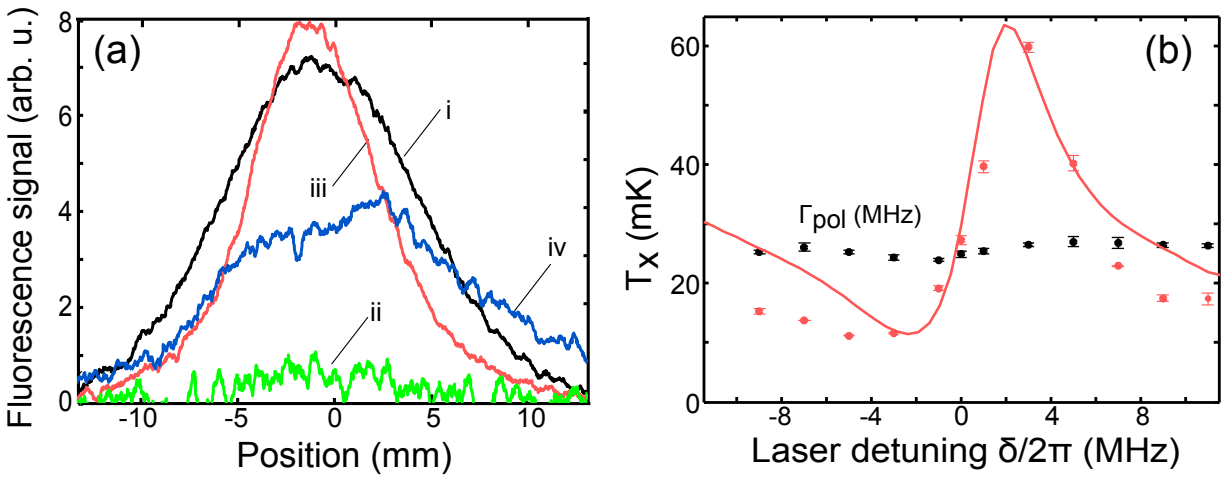

Figure 5.7: 1-D Doppler cooling. (a) Spatial profile of YO beam under the conditions: (i) unperturbed, (ii) Doppler cooling turned on and $v'' = 1$ repumper turned off, (iii) Doppler cooling ($\delta = -2\pi\times$ 5 MHz) , (iv) Doppler cooling ($\delta = 2\pi\times$ 5 MHz) (b) Temperature of 1-D doppler cooled YO beam in terms of laser detuning.

5.2.5 The MOT

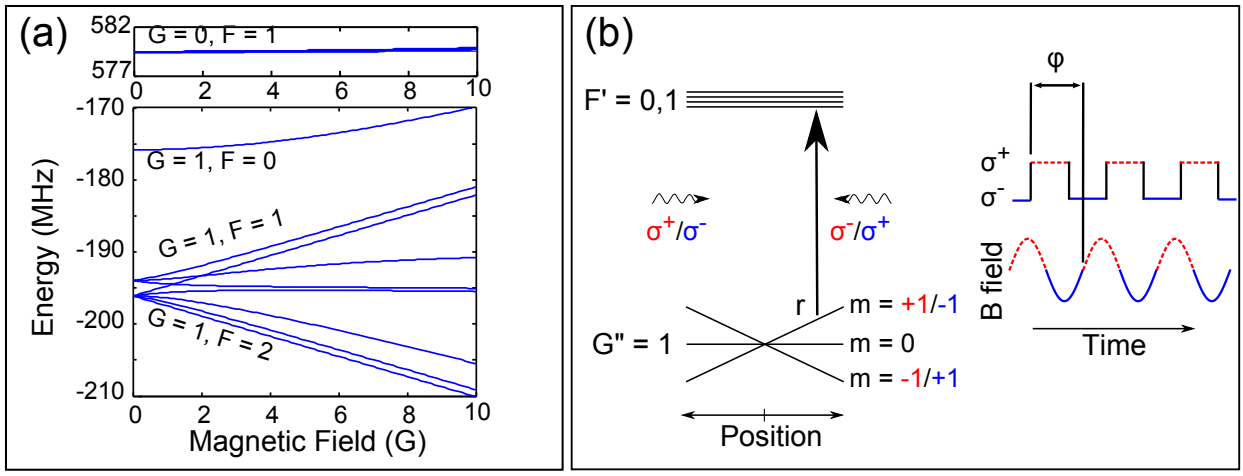

Figure 5.8: (a) Zeeman energy of the $X^2\Sigma^+$ state. (b) Schematic of polarization chopping.

5.2.6 A YO MOT

While the polarization chopping does solve the problem of optical pumping into dark Zeeman sublevels, it does create a significant problem to realize a MOT. In essence, the handedness of the polarization of the incoming laser determines whether the MOT forces confine or blows up the YO beam, hence, with the polarization chopping, each cycle will consist of equal times with confining and anti-confining forces averaging to zero. To solve this problem, we therefore had to switch the direction of the magnetic field in phase with the polarization switching as shown in figure 5.8 (b). Such a scheme was shown to work at acoustic frequencies by Harvey and Murray [151], however in our case, we need to switch our fields at radio frequencies.

In order to match the aspect ratio of our interaction region, we built a rectangular baseball geometry quadruple coils [152] as shown in figure 5.9 (a). The coil is wound with 25 turns of 350/46 Litz wire. The Litz wire was chosen as each wire consists of a bundle of 350 individually insulated 46 gauge wires. The skin depth at $\sim$ 1 MHz is 50 microns, which is

greater than the diameter of each wire, therefore we can maintain both high current carrying capacity and conductivity at rf frequencies. The coils dimensions are $5 \times 5 \times 15$ cm.

The coil itself acts as the inductor in a resonant LC circuit configuration as shown in figure 5.9(b). We were able to achieve a quality factor of $Q \approx 77$ at a frequency of 2 MHz. In order to achieve the required field gradient, we required a peak current 1.5 A which is provided by a inductively coupling 25 W of RF power through a home-built impedance matching transformer. Assuming perfect rf power coupling, we should obtain a root mean square value of the magnetic field gradient to $A_{rms} = 6$ G/cm.

As the expected voltage drop across the coil is on the order of 4 kV, for voltage management, the coils were wound in layers of 5 and glued on to the previous layer with Loctite 401 epoxy. Each layer is then coated with Q-Dope. After winding, the coils are potted in Epo-Tek H70E epoxy. It combines low outgassing with decent thermal conductivity (0.9 W/(m.K)). In-vacuum cooling water lines are attached to the coils with 1 inch thick Boron Nitride standoffs. This is because that bulk metal placed less than a cm from the coils would noticeable reduce the Q (by $\approx 10\%$) (presumably due to Eddy currents). Boron nitride was used as it has good thermal conductivity (30 W/(m.K)) but is electrically insulation.

During the running of the experiment, the coils would heat by ≈ 10 K, thus leading to shifts in the phase of the magnetic field with respect to the supply voltage. For simplicity, we held the polarization switching frequency and phase fixed. The magnetic field is detected with a pickup coil and is phase stabilized to the polarization chopping as shown in figure 5.9(b). This phase locking also allows us to place an arbitrary phase offset ϕ between the polarization chopping and the magnetic field.

Figure 5.10 shows the effect of applying the MOT cooling forces in the $\hat{\mathbf{x}}$ dimension. The laser detuning was set at $\delta = -2 \times 5$ MHz and the $v'' = 1, 2$ repumps are on resonance.. In panel (a) the YO beam spatial profiles under various conditions. Curve (i) shows the uncooled beam while (ii) shows the purely doppler cooled beam for comparison. Turning on the MOT forces with the correct polarization switching ($\phi = 0$) further cools the beam down

to T_x ∼2 mK. There is also a clear enhancement of the molecular signal at x=0, signifying an increase in density in that region. In panel (iv) we switch the magnetic field out of phase with respect to the polarization switching and the beam is only cooled down to 15 mK. While the MOT forces are anti-confining, the doppler cooling is still in effect.

Figure 5.10 (b) shows the dependance of the final transverse temperature as a function of the phase offset between the polarization switching and the magnetic field. As expected, the final temperature is coldest when in phase and least cold when out of phase. The final temperature can be modelled with a MOT force varying by $\cos(\phi)$.

While we have achieved a greater than 10 fold decrease in transverse temperature, we note that we are still a factor of 20 above $T_{Doppler}$ which is due to the short interaction time. From this reduction in temperature, we can calculate the doppler cooling rate $2\beta/m_{YO}$ to be 5×10^3 s^{-1}. Which is in good agreement with the theoretical model of 8×10^3 s^{-1}. In addition, using equation 5.14the MOT frequency ω_x is found to be $2\pi \times 155$ Hz which is good agreement with the calculated value of $2\pi \times 155$ Hz as derived from a field gradient of $A_{rms} = 6G$. We note that the YO beam's interaction time is much less than the MOT oscillation period but is well explained by the rate equation model and provides a clear brightening of the beam. We then extend the MOT action to two dimensions. For this, we set up an identical multipass in the $\hat{\mathbf{y}}$ dimension. Figure 5.11 (a) shows the effects of the MOT and doppler cooling in only the $\hat{\mathbf{y}}$ dimension while still measuring the spatial profile along the $\hat{\mathbf{x}}$ dimension. From this we see an enhancement of the signal and this is because the spatial spread of the unperturbed molecules in the $\hat{\mathbf{y}}$ dimensio is larger than the detection beam. Therefore, the doppler cooling (curve (ii)) and MOT (curve (iii)) brightens the beam towards the center and thus more molecules are detected as compared to the uncooled beam (i). Note that T_x is unchanged as we do not manipulate the molecules in this dimension. Figure (b) shows a comparison between the 1D and the 2D MOT. Curve (i) is the unperturbed case and curve (ii) shows the spatial profile for a 1D MOT. The 2D MOT action (curve iii) does a similar overall beam enhancement as in (a). However,

the final temperature is higher than of the 1D MOT and is consistent with damping and MOT forces one half of the 1D case. This is to expected qualitatively as when driven above saturation, the scattering rate is limited to in our case $\Gamma/7$. As half of these scatters are due to absorptions from the $\hat{\mathbf{y}}$ cooling beams, the force along the $\hat{\mathbf{x}}$ dimension has to be halved. This result also comes out be solving equations 5.2 and eq: Multilevel Force.

We also observe a $\sim 10\%$ decrease in the total molecular signal when performing the doppler cooling and MOT experiments. This is due to decays through the intermediate $A'^2\Delta_{3/2}$ electronic state that leads to optically pumping into dark rotational states. Due to the short $\sim$275 μs interaction time, this is not a problem in this experiment but presents a serious challenge for the loading of of a 3D MOT. The solution to this problem will be discussed in Chapter 6.

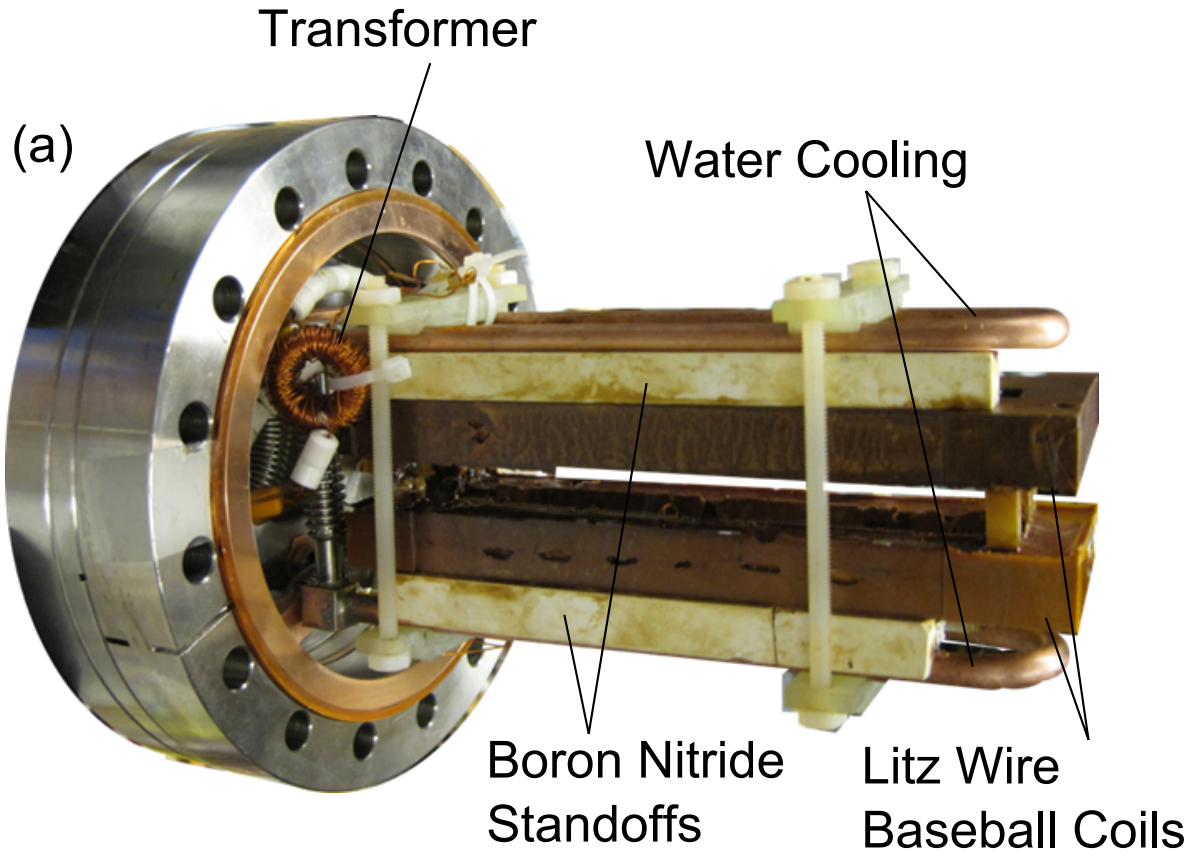

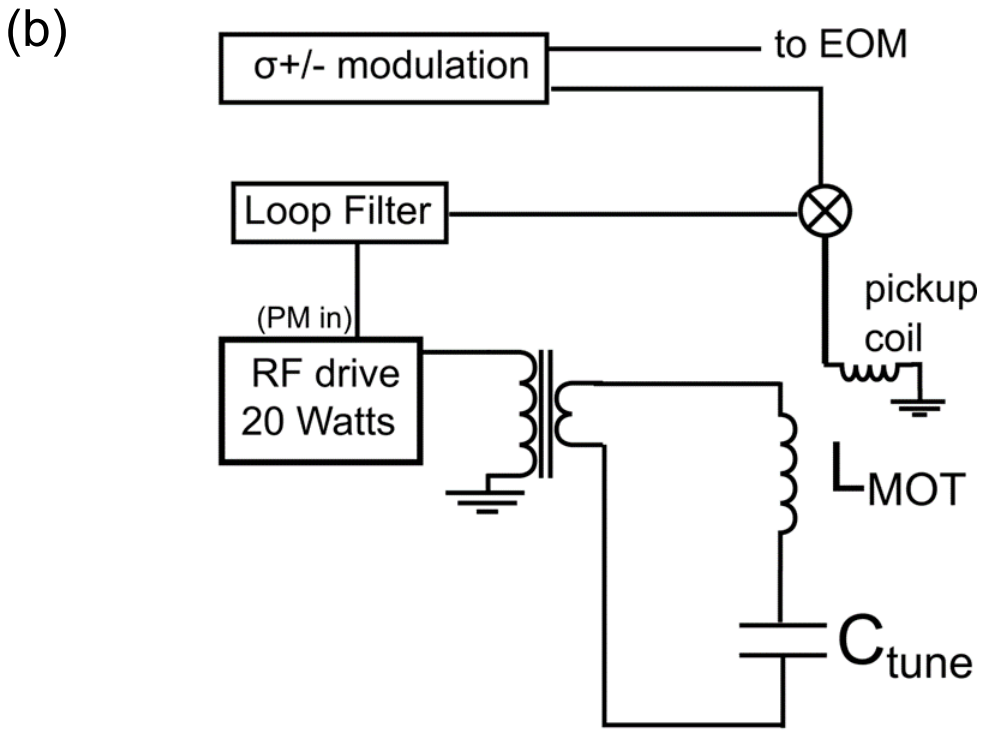

Figure 5.9: (a) Photograph Baseball MOT coils resonance circuit. (b) Schematic of resonant MOT coil. The phase of the magnetic field is monitored with a pick-up coil and is locked to the polarization switching phase.

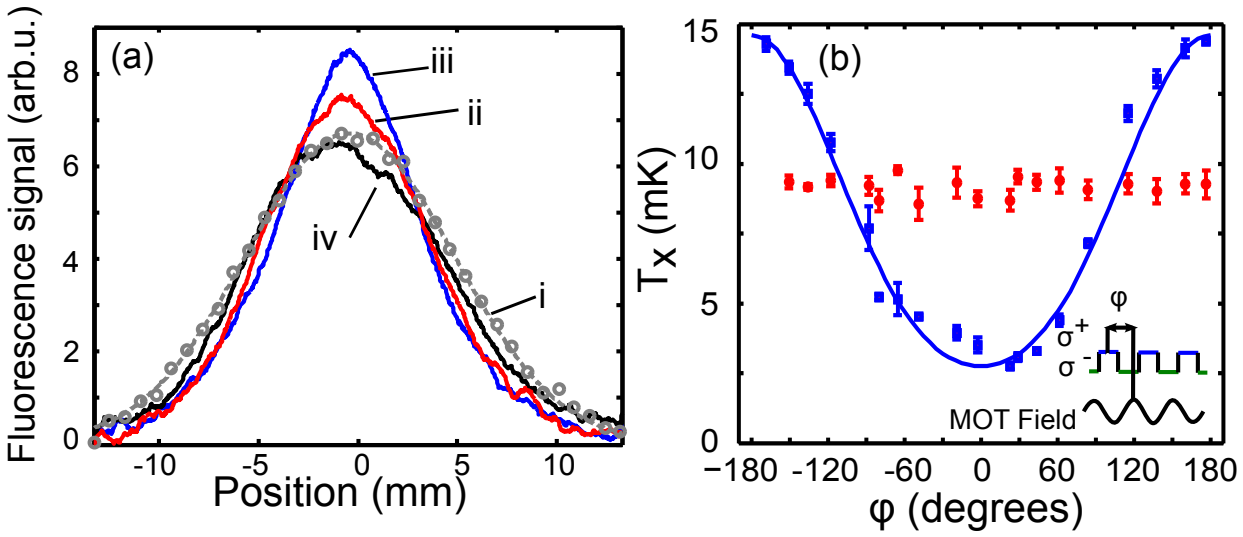

Figure 5.10: 1-D MOT and Doppler cooling. YO beam spatial profiles for (i) unperturbed beam, (ii) a Doppler cooled beam (iii) a 1D MOT ($\phi = 0$) (iv) a 1D anti-MOT ($\phi = 180°$) (b) (Purple) T_x as a function of ϕ, the phase offset between the polarization switching and the magnetic field. (Red) Doppler cooling only.

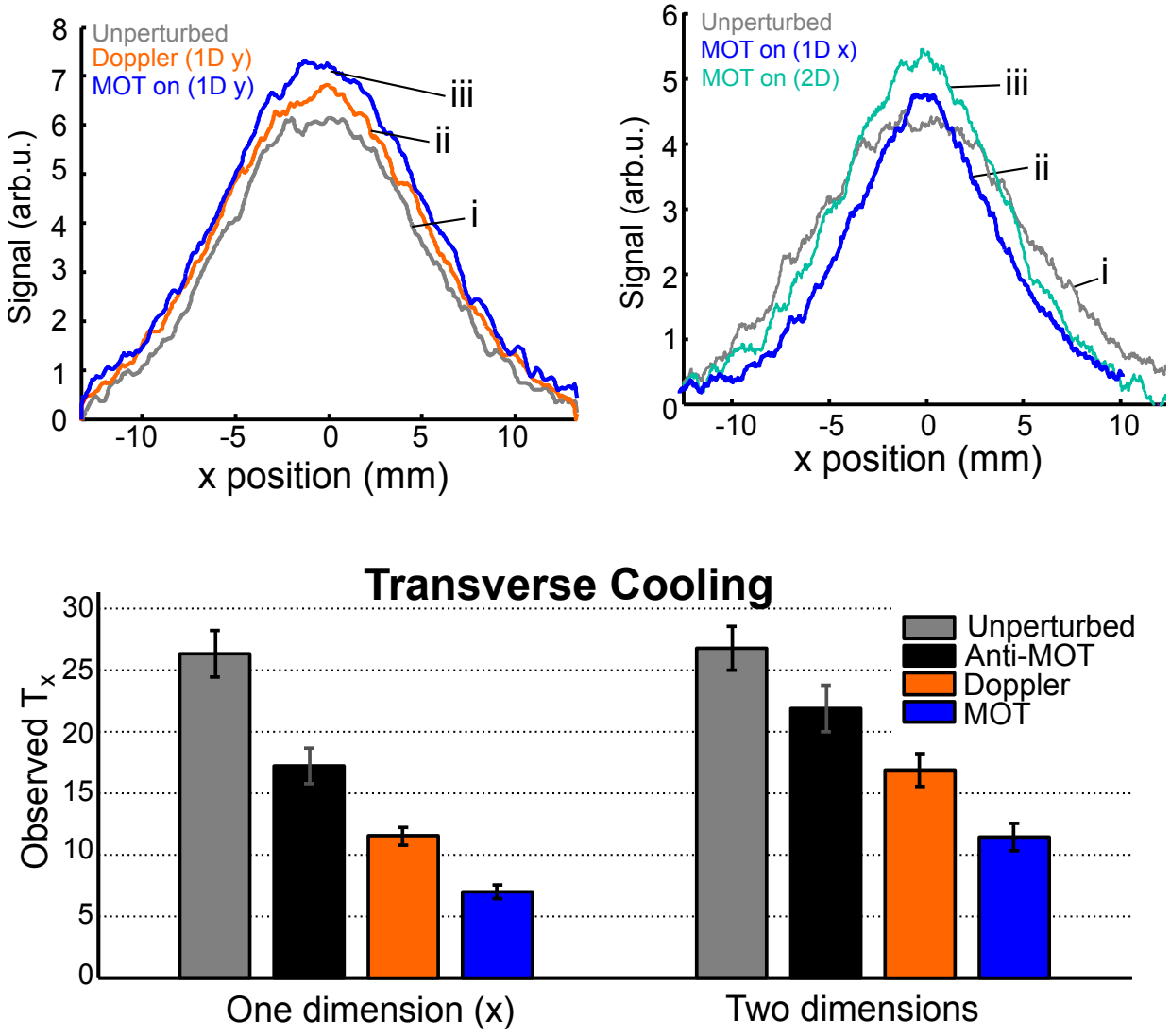

Figure 5.11: (a) YO beam profiles in the $\hat{\mathbf{x}}$ dimension with cooling action only in the $\hat{\mathbf{y}}$ dimensions. (i) An unperturbed beam, (ii) Doppler Cooling only and (iii) 1D MOT. (b) YO spatial profiles for (i) Unperturbed, (ii) 1D MOT in $\hat{\mathbf{x}}$ an (iii) 2D MOT. (c) Summary of transverse temperature T_x for Doppler and MOT cooling in 1 and 2 dimensions.

Chapter 6

Microwave remixing and longitudinal slowing.

6.1 Introduction

There are two closely related problems that we need to solve to extend the 2D MOT technology to the realization of a 3D MOT for YO. The first is to sufficiently slow the YO beam to MOT trappable velocities, and the second is to stop the leakage through the intermediate $A'^2\Delta_{3/2}$ electronic state. In this chapter, we will make an estimate for the MOT trapping velocities, which will turn out to be much slower than what is emitted from the cryogenic beam source. Branching through the $A'^2\Delta_{3/2}$ state presents a problem as decays through this state lead to decays into the $N'' = 0, 2$ rotational dark states. This presents a problem to both the final MOT lifetime and the generation of sufficiently slow YO molecules to be loaded into the trap.

6.1.1 Capture Velocity Estimation

A standard method to estimate capture velocity is to simulate the trajectory of the molecule and look for the highest velocity for which it stays within the cooling laser beam radius [1], which we shall set to 5 mm.

For the laser and MOT cooling along 1 dimension, we determined that the doppler cooling rate is

$$\Gamma_D = \frac{2\beta}{m} = 5000 s^{-1} \tag{6.1}$$

and the trap oscillation frequency is

$$\omega_{MOT} = \sqrt{\kappa/m} = 2\pi \times 155Hz \tag{6.2}$$

For the 3D MOT, the cooling forces must be derated by a factor of three from the 1D case as we now have 3 pairs of counter-propagating beams. We therefore use the force equation,

$$F_x = -\frac{\beta}{3}v - \frac{m}{3}(\omega_{MOT})^2 x \tag{6.3}$$

In figure 6.1, the trajectories are plotted in terms of position and velocity. Each molecule starts at position -5 mm with varying velocities. The trajectory for the 11 m/s molecule is shown in red and as it travels past +5 mm it would no longer be trapped. Therefore by this criterion we estimate 10 m/s as be the capture velocity of the MOT.

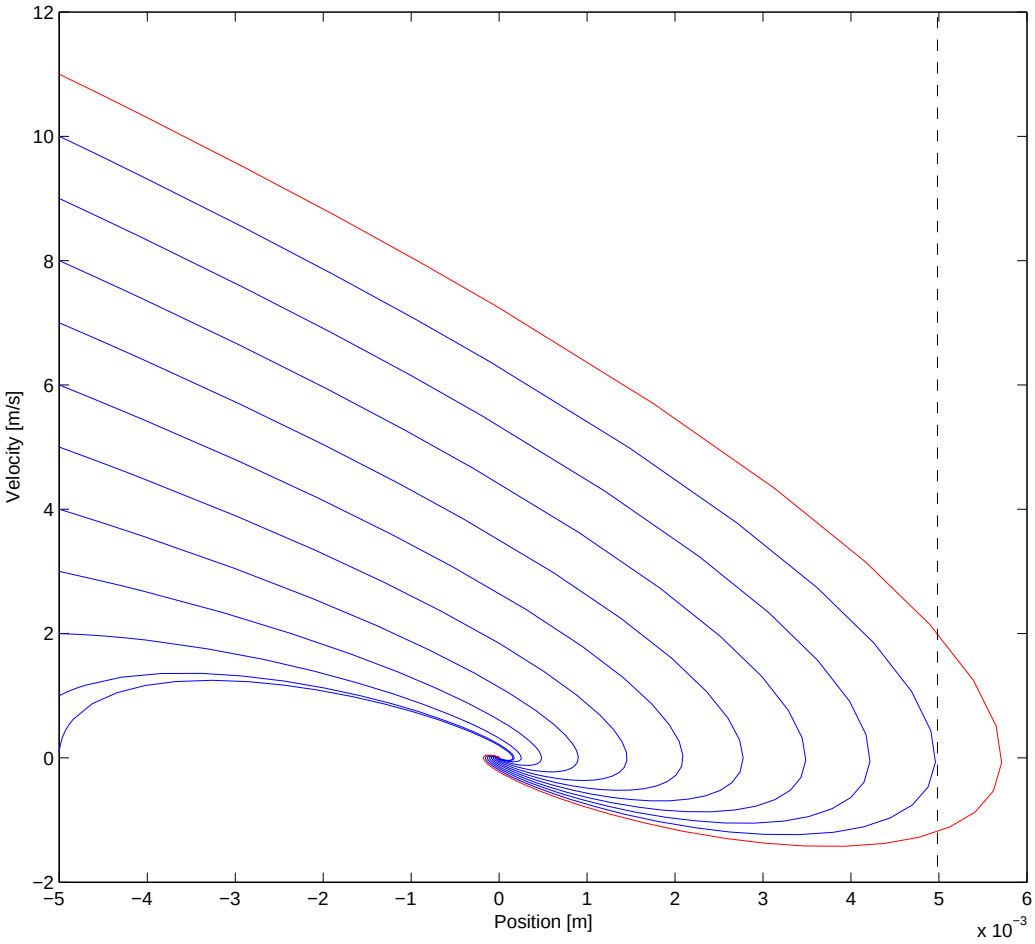

Figure 6.1: Simulation of capture process for 3D MOT. Above 10 m/s, the molecule does not turn around by $x = 5$ mm and is lost.

6.1.2 MOT Loading in a cell

Due to the relatively large longitudinal velocity of the beam compared to the MOT trapping velocity, it may be tempting to perform the MOT inside the cryogenic cell and not worry about trying to slow the molecular beam. However, this approach turns out to not be feasible.

We simulate the MOT action 1 cm diameter laser beams on all three cartesian axes with the MOT forces. The new 3 D MOT coils are designed to have the same magnetic field gradient along the weak axes as the baseball coil in the 2D MOT. Therefore, we simulate the MOT using the expression for the force

$$F_x = -\frac{\beta}{3}v - \frac{m}{3}(\omega_{MOT})^2 x \tag{6.4}$$

$$F_y = -\frac{\beta}{3}v - \frac{m}{3}(\omega_{MOT})^2 y \tag{6.5}$$

$$F_z = -\frac{\beta}{3}v - \frac{2m}{3}(\omega_{MOT})^2 z \tag{6.6}$$

We assume that the MOT is in a uniform density of helium, and we model the YO molecule's trajectories as well as their internal rotational states. Fluorescence is estimated by counting the number of molecules within all 6 cooling beams and in the $N'' = 1$ state. Further details of the simulations can be found in the Appendix 1. The estimated collision rate can be expressed in terms of

$$\gamma_{col} = n_{He}\sigma v_{col} \tag{6.7}$$

where n_{He} is the buffer gas number density, σ is the collision cross section and v_{col} is the mean relative velocity of the He and YO molecules. As YO is heavier than helium, this velocity is roughly the rms thermal velocity of helium. While the YO-He collisions cross section is not known, the collision cross section between trapped CaH and He was measured to be $\sim 10^{-14}$ cm^2 and we use this value to estimate the He-YO collisions rate from a known

helium density.

Figure 6.2 shows three helium density regimes. The high helium density regime is needed in order to thermalize the ablation plume and in our cell that density is $\sim 10^{15}$ cm^{-3}. In this regime, the YO molecules are confined due to the high He density and concomitant long diffusion time constant. At low pressures the MOT forces dominate and lifetimes are on the order of several 10s ms. In between these two extreme density regimes, there is a region of minimum lifetime. This is shown in Figure 6.3. This minimum lifetime in our system $\sim$1 ms and occurs at a helium number density of 10^{13} cm^{-3}. This presents a problem as the pump out time of the cell as calculated in Chapter 4 is $\sim$12 ms, which is much longer than this minimum lifetime. Therefore, there is no way to move between the high and low density regimes quickly enough without destroying the YO MOT.

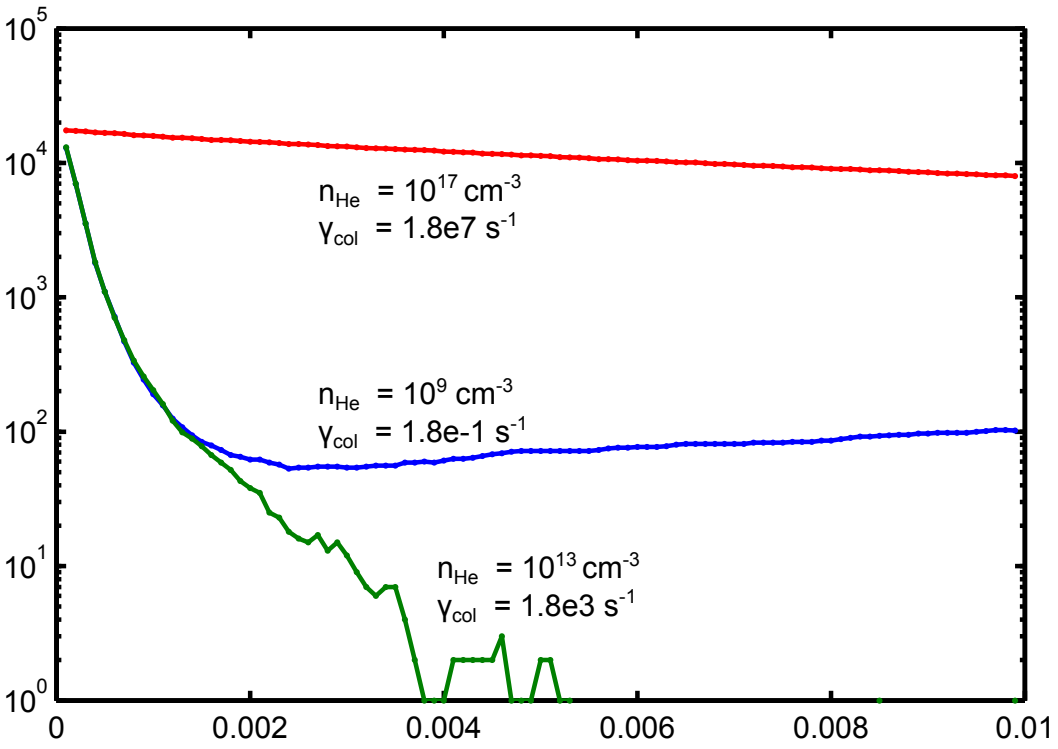

Figure 6.2: Simulation of expected fluorescence signal for three different buffer gas density regimes.

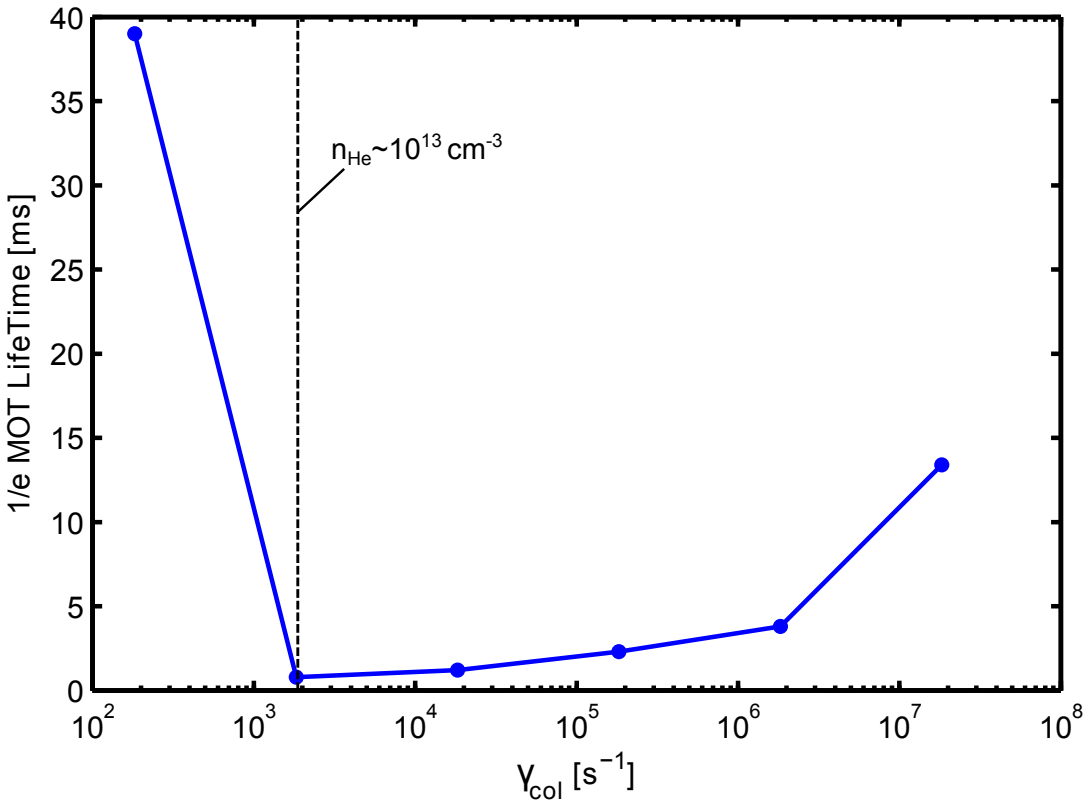

Figure 6.3: 1/e MOT lifetime as a function of He buffer gas density. The minimum lifetime is at 0.8 ms corresponding to an approximate density of 10^{13} cm^{-3}.

6.2 Microwave mixing and slowing

6.2.1 Introduction

While directly loading a buffer-gas cooled atomic beam into a three-dimensional (3D) magneto-optic trap (MOT) is possible [153], for molecules with much lower photon scattering rates compared to typical laser cooled atomic species, longitudinal optical cooling is necessary for loading into a 3D MOT. Typically 10^4 photons must be scattered to slow molecules to within the capture velocity of a MOT. During the slowing process, the molecular transition used for optical cooling experiences a Doppler frequency shift of tens or hundreds of resonance linewidths, resulting in inefficient photon scattering for a monochromatic unchirped laser beam. To date, molecules that have been laser cooled all have the magnetic sub-levels in the ground electronic state continually remixed by the multi-level optical cycling process. This is consequence of the type-II MOT transition required for rotational closure. Hence, the widely used atomic Zeeman slower [154], which relies on the Zeeman shift of a single magnetic sublevel to compensate for the Doppler shift during deceleration is not applicable. To maintain a sufficiently large optical scattering rate throughout the slowing process, two techniques have been employed. Chirping the laser frequency was shown to reduce the velocity of a supersonic beam of CaF by 30 m/s [75]. For SrF, broadband laser radiation was used to slow molecules to be loaded directly into a 3D MOT [72].

Optical cycling in molecules [68, 70] is critical for the radiation pressure force to directly slow and cool molecular beams. However, achieving optical cycling in a large class of molecules remains difficult due to optical pumping into dark states. While vibrational dark states can be addressed with repump lasers [67], maintaining rotational closure has heretofore been ensured with a mixture of angular momentum and parity selection rules. However, there are several loss mechanisms that break the rotational closure in current molecular optical cycling schemes and they arise from additional decays via intermediate states or higher order transition moments.

The first mechanism is due to decays between vibrational levels in the ground electronic states. In the case of YO, this loss mechanism occurs due to decays from the $v'' = 1, N'' = 1$ state down to the $v'' = 0$ state. Decays from higher vibrational states are suppressed by the harmonic oscillator selection rules, $\Delta v = \pm 1$. Due to parity selection rules, this process will end up populating the $N'' = 0, 2$ levels in the case of YO for example. From [155], the transition dipole moment is given by

$$\mu_{v+1,v} = \sqrt{\frac{v+1}{2}}\sqrt{\frac{\hbar}{m_{YO}\omega_e}}\left(\frac{d\mu}{dR}\right)_{R=R_e} \tag{6.8}$$

where v here is the vibrational quantum number, $\omega_e = 861cm^{-1}$ is the vibrational constant, and $\left(\frac{d\mu}{dR}\right)_{R=R_e}$ is the derivative of the electric dipole moment function evaluated at R_e, the equilibrium internuclear distance. The derivative's value is calculated to be 3.5 Debye/a_0 [82] where a_0 is the Bohr radius. The resulting transition dipole moment, $\mu_{1,0}$, is .090 Debye. The linewidth is then given by

$$\Gamma_{vibrational} = \frac{1}{3\pi\epsilon_0\hbar c^3} * \omega_e^3\mu_{1,0}^2 \tag{6.9}$$

which yields a value of 1.6 s^{-1} or a 1/e lifetime of 620 ms.

Magnetic dipole moments connect states of equal parity, in contrast to electric dipole transitions which connect states of opposite parity. Decays via magnetic dipole transitions are typically suppressed by a factor of $\alpha^2 \approx 5 \times 10^{-5}$ compared to electric dipole transitions where α is the fine structure constant [156]. However recent measurements in OH indicate that they can be a factor of $\sim$10 faster than expected [58], making this a potentially large population leakage mechanism.

For some molecules, maintaining optical cycling can be more complex due to decays through intermediate electronic states, which are present in, for example, YO [78] and BaF [157]. Such decays are normally suppressed by the relatively long transition wavelengths. For YO the suppression factor is $\sim 3 \times 10^{-4}$ compared to the main cycling transition. However, the decay is sufficient to cause population leakage to rotational dark states when a large number of photon scatters are needed for cooling.

For the rest of this section, we discuss the demonstration of microwave mixing of rotational states to close these additional loss channels. This enables us to slow a beam of YO emitting from a two-stage buffer gas cell to molecular velocities < 10 m/s, at which point the YO molecules can be loaded into a 3D MOT.

The optical cycling transition in YO was discussed in sections 2.6 and 2.5. In brief, highly diagonal Franck-Condon factors limit vibrational branching [81] such that a single repump laser limits branching loss to 3.6×10^{-4} (Fig. 6.4(a)). Rotational branching is suppressed by a combination of parity and angular momentum selection rules [68, 69] when driving the $X^2\Sigma, N'' = 1$ level, where N is the rotation quantum number. Figure 6.4(b) shows the hyperfine structure of the $X^2\Sigma$ states, where G is the coupled nuclear and electronic spin, and F is the total angular momentum. For the $A^2\Pi_{1/2}$ and $A'^2\Delta_{3/2}$ states, J is the total angular momentum excluding nuclear spin. For all electronic states, $p = \pm$ represents the parity.

Figure 6.4(a) shows the additional loss channel where the $A^2\Pi_{1/2}$, $J' = 1/2$ state decays to the $A'^2\Delta_{3/2}$, $J' = 3/2$ state. Decays to states of higher J in the $A'^2\Delta_{3/2}$ are forbidden due to angular momentum selection rules. The $A'^2\Delta_{3/2}$ state has a radiative lifetime of $\sim$1 μs [78] and will rapidly decay back to the $X^2\Sigma$ state. Since the full cycle starting from and returning to the ground state is a three-photon process, the parity at the end of this process must change sign and therefore allow decays only to even rotational states (Fig. 6.4(c)). In the $X^2\Sigma$ state, while J'' is not a good quantum number, each rotational state can be expressed in terms of states with $J'' = N'' \pm 1/2$. The $\Delta J = 0, \pm 1$ angular momentum selection rule prevents decay to $N'' \geq 4$. This is because the lowest value of J'' for these states is 7/2. Therefore this process optically pumps into the $N'' = 0, 2$ states. The rotational constant, B, for the $X^2\Sigma$ state is 11.634 GHz. Microwave radiation tuned to $2B$ ($4B$) can mix the $N'' = 0$ (2) levels with the $N'' = 1$ level. This mixing effectively removes the rotational dark states; however the maximum optical scattering rate is lowered as the number of states in $X^2\Sigma$ involved in optical cycling increases. We estimate the maximum photon scattering rate

as follows,

$$\Gamma_{max,cycle} = \Gamma \frac{n_e}{n_e + n_g} \tag{6.10}$$

where n_e and n_g are the number of zeeman states in the excited and ground state respectively. In the case of the optical cycling described in chapter 5, $n_e = 4$; the number of states in each rotational level in the $X^2\Sigma^+$ state is given by $8N'' + 4$, as such n_g is 24 where we note this value also includes the zeeman states in $v'' = 1, N'' = 1$ as the repumping drives to the same $A^2\Pi_{1/2}, J' = 1/2$ state as the main cycling transition. This yields a maximum cycling rate of $\Gamma/7$.

Once microwaves are applied, n_g increases to 48. This is because the $v'' = 0$ state now involves states from the $N'' = 0, 1, 2$ levels. As we will see shortly, the number of states in $v'' = 1$ is unchanged at 12 as the microwave radiation that we produce is not sufficiently power broadened to mix the $v'' = 1$ rotational states. This leads to a maximum cycling rate of $\Gamma/13$ once microwave mixing is applied, nearly a two-fold decrease.

We employ this rotational state microwave mixing scheme for longitudinal slowing of a YO beam generated from a cryogenic buffer gas beam source as described in Chapter 4. We laser ablate sintered Y_2O_3 pellets in a copper cell filled with helium buffer gas at 3.5 K (Fig. 6.5(a)). The hot YO thermalises rotationally and translationally to the cold helium and the two stage cell [49] produces a YO beam with a mean forward velocity of 70 m/s as measured in the detection region. The YO beam then travels 89 cm to the detection region, during which it may be illuminated by a 6 mm diameter, counter-propagating slowing beam. The 614 nm $v'' = 0$ laser has 70 mW of power and the 648 nm $v'' = 1$ laser has 80 mW (Fig. 6.4(a)). The slowing laser has three frequency components to address the hyperfine manifold (Fig. 6.4(b)). To provide the rotational mixing, we use two pairs of microwave horns located along the beam path. Each pair produces $\sim$1 mW of either the 23 GHz or 46 GHz microwaves.

For velocity sensitive detection, we measure the fluorescence induced by a low intensity

4 mW/cm^2, 614 nm beam aligned 45° to the molecular beam. This probe laser has a saturation parameter of ∼0.5 (Fig. 6.4(b)). This eliminates mechanical and optical pumping effects from the detection beam. In contrast to the slowing beam, we note that the doppler sensitive detection beam only consists of the frequency components to address the $G'' = 0, F'' = 1$ and $G'' = 1, F'' = 1, 2$. Due to the small 15 MHz hyperfine spacing, molecules in the $G'' = 1, F'' = 1, 2$ manifold travelling ∼15 m/s faster than the intended velocity class end up being resonant with the $G'' = 1, F'' = 0$ frequency component, thus this frequency component is not used as it causes overestimation of the slow molecule number. The detection laser can be scanned over a range of ∼100 MHz at a rate of 1 kHz, corresponding to a velocity detection range of ∼100 m/s.

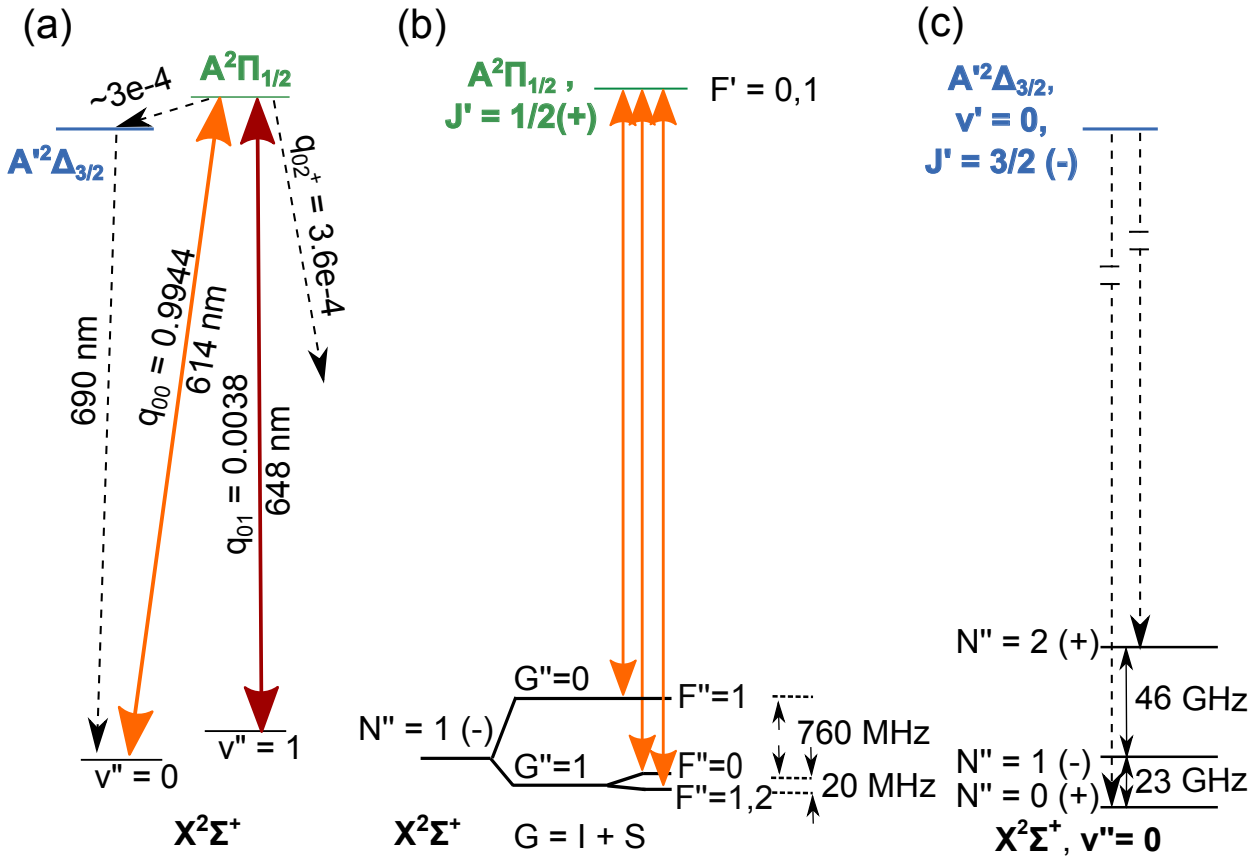

Figure 6.4: (Color online) (a) YO vibronic structure. Dashed arrows indicate decay paths with corresponding Franck-Condon factors, q [81]. Solid arrows indicate cooling and repump laser transitions. (b) Hyperfine structure. Solid arrows indicate the three hyperfine pumping components used in each vibrational manifold. (c) Rotational mixing. Dashed arrows indicate the decay paths to $X^2\Sigma$ through the $A'^2\Delta_{3/2}$ state and black solid arrows show the microwave rotational mixing.

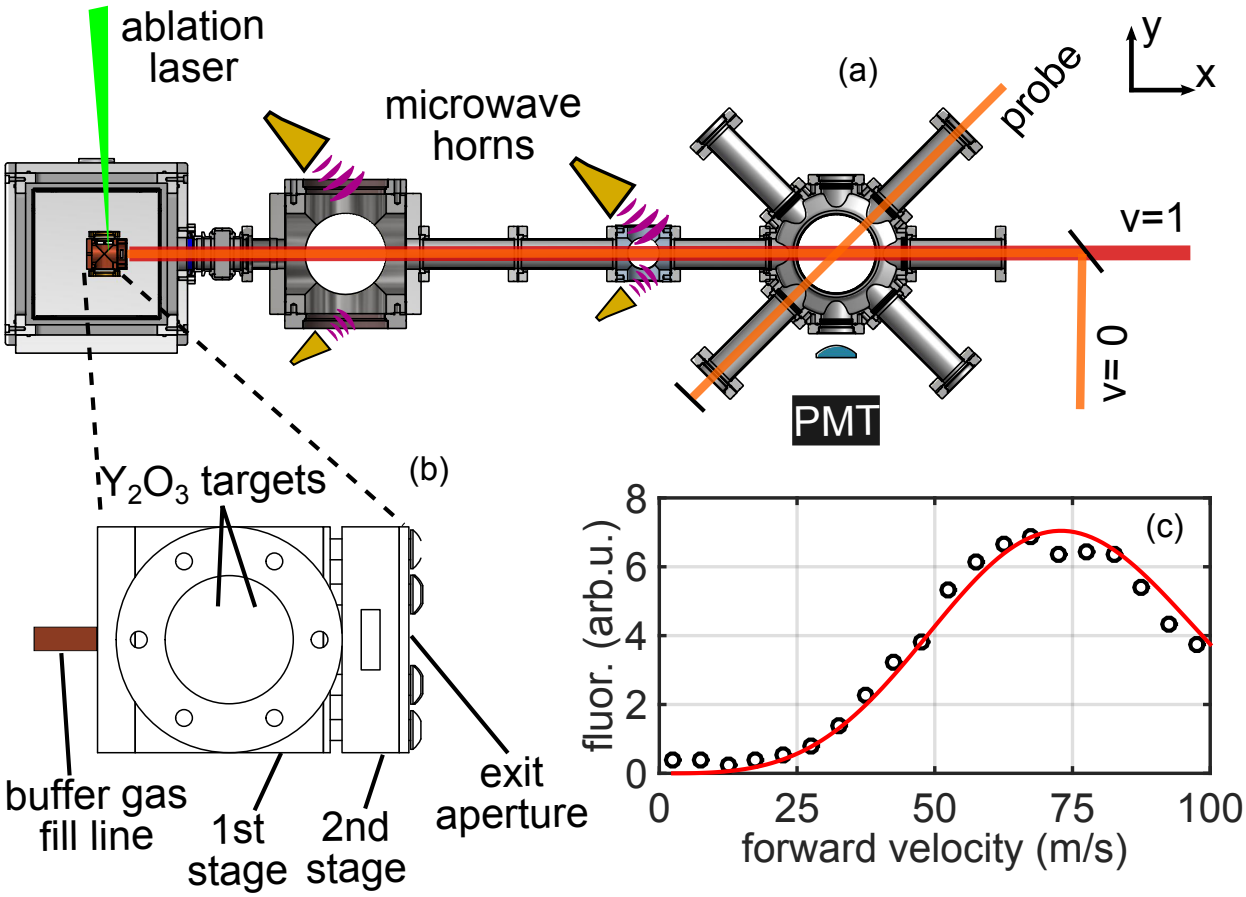

Figure 6.5: (a) Depiction of the beam apparatus. The YO molecular beam interacts with a counter-propagating slowing laser beam along x. A 45° probe beam is used for Doppler sensitive detection. A PMT is used to collect fluorescence induced by either the slowing or probe beam. (b) Two-stage buffer gas cell. (c) Velocity distribution measured at the detection region. The solid line is a fit to a Gaussian (with center longitudinal velocity of the beam at 49 m/s and a temperature of 8 K) multiplied by the square of the forward velocity to account for the transverse velocity spread.

6.2.2 Optical cycling enhancement via microwave mixing.

We study the rotational mixing by observing the fluorescence induced by the slowing beam in Fig. 6.6(a). We apply the microwaves in four binary combinations. For case i, no microwaves are applied. In contrast, when microwave mixing is applied to both $N'' = 0, 2$, (curve iv), there is a factor of four increase in fluorescence. Applying only the $N'' = 0 \leftrightarrow N'' = 1$ or $N'' = 2 \leftrightarrow N'' = 1$ mixing (Fig. 6.6(a) ii, iii respectively), we see a factor of two increase in fluorescence compared to case i.

These measurements in panel (a) can also be used to identity the predominant optical pumping mechanism. As calculated in Section 6.2.1, the vibrational lifetime is ∼600 ms, which is much longer than the optical pumping time scale. The branching ratios, calculated in Section 2.7, allow us to eliminate the M1 transitions as the branching ratios from the $A^2\Pi_{1/2}$ state is 2/3(1/3) for the $N'' = 0(2)$ levels in the $X^2\Sigma$ state. On the other hand, electric dipole transitions from the $A'^2\Delta_{3/2}$ state have equal branching ratios to the $N'' = 0, 2$ rotational levels, consistent with curves ii and iii. Hence, we identify decays through the intermediate $A'^2\Delta_{3/2}$ as the dominant loss process.

To verify that the mixing microwaves are sufficiently strong to address all hyperfine states without the need of additional frequency sidebands, we simultaneously vary the frequency of the $N'' = 1 \leftrightarrow N'' = 0(2)$ mixing microwave by $\delta(2\delta)$ and measure the corresponding enhancement in fluorescence (Fig. 6.6(a) inset). This enhancement follows a 24 MHz full-width half-maximum Lorentzian lineshape. This width is larger than the hyperfine variations of <5 MHz (see Section 2.3) among the three relevant rotational manifolds. The mixing for higher vibrational states is suppressed because the rotational constant B for $v'' = 1$ is 50 MHz smaller than that for $v'' = 0$. This results in a 100 (200) MHz detuning for the $N'' = 0$ (2) transition in $v'' = 1$. Hence, we do not suffer any further reduction in the maximum optical cycling rate.

In Fig. 6.6(b), we study the time dependence of the optical pumping into $v'' = 1$, and

also into rotational dark states via a previously unexplored branching route from the $A^2\Pi_{1/2}$ state to the $A'^2\Delta_{3/2}$ state. Again we measure the fluorescence induced by the slowing beam. For case i, the slowing and repumping light as well as microwaves are turned on throughout the experiment. For case ii, the $v'' = 1$ repump laser is rapidly shut off in $\sim$10 μs at 14 ms and rapidly switched back on at 19 ms after ablation. This leads to an abrupt decrease in the fluorescence as the YO molecules are rapidly pumped into the $v'' = 1$ state and no longer scatter light. To extract this pumping rate, we divide curve (ii) by curve (i) and fit an exponential with a constant background ratio of 0.25, resulting in a $1/e$ time constant of 620 μs. Combining this with the calculated Franck-Condon factor $q_{01} = 3.8 \times 10^{-3}$ [81] yields a photon scattering rate of 4.3×10^5 s^{-1}. This is smaller than the maximum possible scattering rate by a factor of $\sim$5 [71] which may be due to inefficient depletion due to highly Doppler detuned molecules, insufficient power in the wings of the slowing beam, or an overestimate of the q_{01} Franck-Condon factor. Curve iii shows the fluorescence when only the rotational mixing microwaves are turned off between $14 - 19$ ms. The $1/e$ decay due to pumping into rotational dark states has a 7.4 ms time constant (inset curve iii). By combining the ratio of the two loss rates and q_{01}, we estimate the branching ratio from $A^2\Pi_{1/2}$ to $A'^2\Delta_{3/2}$ to be $\sim 3 \times 10^{-4}$. This branching ratio agrees with the value derived from transition dipole moments calculated in Ref. [82] and is similar to the combined branching ratio to $v'' \geq 2$. At 19 ms after ablation, the vibration repump (curve ii) and mixing microwaves (curve iii) are turned back on and the fluorescence immediately recovers.

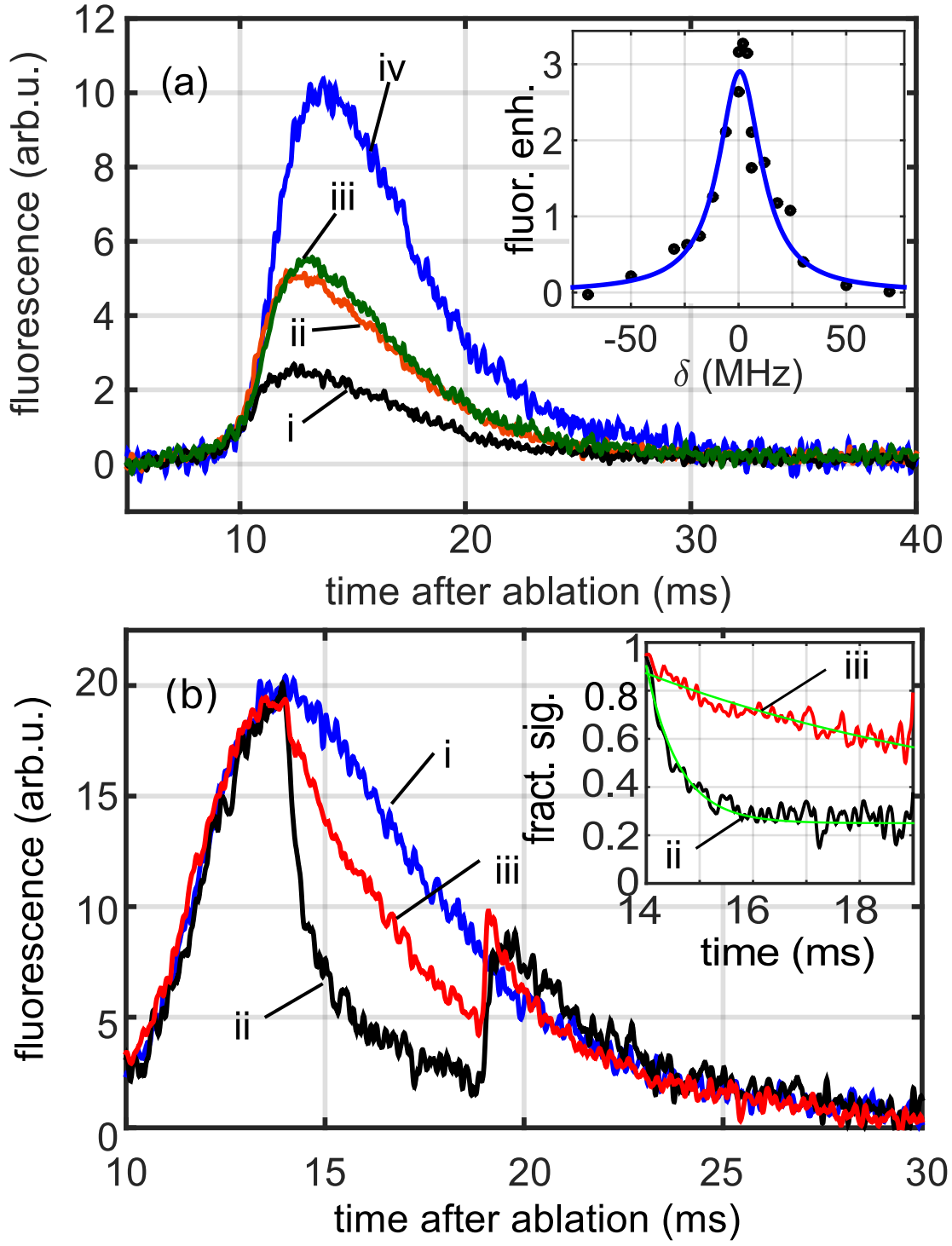

Figure 6.6: (Color online) (a) Optical cycling enhancement due to rotational mixing. The fluorescence is induced by the high power optical slowing beam and $v'' = 1$ repump: (i) No mixing; (ii) $N'' = 0 \leftrightarrow N'' = 1$ mixing only; (iii) $N'' = 2 \leftrightarrow N'' = 1$ mixing only; (iv) simultaneous $N'' = 2 \leftrightarrow N'' = 1$ and $N'' = 0 \leftrightarrow N'' = 1$ mixing. The inset shows the fractional enhancement of optical scattering vs. microwave detuning from the rotational resonance. (b) Comparison of branching losses between $v'' = 1$ and $A'^2\Delta_{3/2}$: (i) Microwaves and $v'' = 0, 1$ are on throughout; (ii) $v'' = 1$ repump is shut off from 14-19 ms after ablation; (iii) Microwave mixing is switched off from 14-19 ms. The inset shows curves (ii) and (iii) divided by curve (i). Solid green lines are exponential fits.

6.2.3 Radiation pressure slowing

We estimate the capture velocity of a 3D MOT for YO with a laser beam diameter of 1 cm to be 10 m/s. To slow some fraction of the molecules to below this capture velocity, we apply longitudinal radiation pressure slowing with protocols shown in Fig. 6.7(a). To increase the fraction of molecules addressed by the slowing beam, we spectrally broaden the light [158] via a resonant electro-optic modulator (EOM) with a modulation frequency of 10 MHz and a phase modulation index of 3.3. This spectrally broadens each laser frequency to $\pm$30 MHz, corresponding to a velocity spread of $\pm$20 m/s. Polarization switching used for destabilizing Zeeman dark states [71] further adds 5 MHz sidebands and we obtain frequency components spaced by the natural linewidth of the main cooling transition. This ensures continuous deceleration across a $\sim$ 50 m/s velocity range (Fig. 6.7(b)).

As the range of the slowing force is smaller than the velocity spread of the YO beam itself, we implement frequency chirping on the slowing light. In Fig. 6.7(c) and (d), the slowing sequence is designed to enhance the number of molecules at 30 m/s. The molecules propagate freely for the first 12 ms after ablation, then the slowing beam is turned on from 12-22 ms. During this time, the center of the broadband radiation is linearly swept from being resonant with 64 m/s to 44 m/s molecules. In panel (c), we see a molecular population enhancement between $20-40$ m/s (negligible for below 20 m/s), and depletion for velocities greater than 40 m/s. In panel (d), we maintain the probe laser's frequency to be resonant with the 30 m/s molecule and observe an enhancement in the number of molecules in this velocity class. Due to off-resonant excitations, some faster molecules (35 m/s) contribute to the detected signal at 27 ms for the unslowed case.

To produce even slower molecules, we increase the time during which the slowing laser is turned on and perform a frequency chirp to address lower velocity molecules. The slowing light is turned on 2 ms after ablation and is left on for the next 24 ms. During the first 20 ms, the center frequency of the broadband slowing laser is linearly increased from being resonant

with 64 m/s to 34 m/s molecules (Fig. 6.7(a)). Figure 6.7(e) shows the velocity distribution after the slowing sequence compared to the original velocity distribution. Slowing enhances the molecular population below 20 m/s and depletes molecules with velocities higher than 20 m/s. We tune the probe laser frequency to be resonant with the 10 m/s molecule and we see a clear enhancement in the number of molecules in this velocity class (Fig. 6.7(f)). Unslowed molecules leaving the cell with 10 m/s forward velocity will arrive 89 ms after the ablation, which is well after the detection time. Hence, we attribute the non-zero 10 m/s signal in the unslowed case to off-resonant excitations from fast molecules.

For the detection time windows shown in Fig. 6.7(d,f), we estimate the percentage of molecules in the 30 m/s and 10 m/s velocity classes with a Doppler resolution of ± 3 m/s to be 2% and 0%, respectively for the unslowed beam, based on Fig. 6.5(c). The laser slowing enhances the corresponding population fractions to be 3% and 0.1% of the total original distribution. We note that without microwave mixing, the radiation pressure slowing stops working due to the fast optical pumping to the dark states.

We demonstrate enhanced optical cycling in YO via microwave mixing of rotational states in the ground electronic state. This enabled us to slow longitudinally the YO beam via radiation pressure, producing molecules that can be loaded into a 3D MOT. Because this technique maintains rotational closure with less stringent requirements on the cycling transition, it becomes relatively straightforward to perform laser cooling of molecules on $J'' \rightarrow J' = J'' + 1$ transitions, which would avoid the complications of dark states that are present in $J'' \rightarrow J' = J'' - 1$ molecular MOTs [71, 73], as was originally proposed [68]. This opens the door to laser cooling a greater variety of molecules with more choices of cooling transitions. To further close the vibrational branching to $< 10^{-6}$, an additional $v' = 1 \leftarrow v'' = 2$ repump laser at 649 nm can be used [71, 81]. By turning off the microwave mixing for $N'' = 1 \leftrightarrow N'' = 0$ at an appropriate time, we can accumulate trapped cold YO in the ro-vibrational ground state. The $A'^2\Delta_{3/2}$ state lifetime of $\sim$1 μs opens up the possibility of a narrow line MOT [90, 159] and we will discuss this in the next chapter.

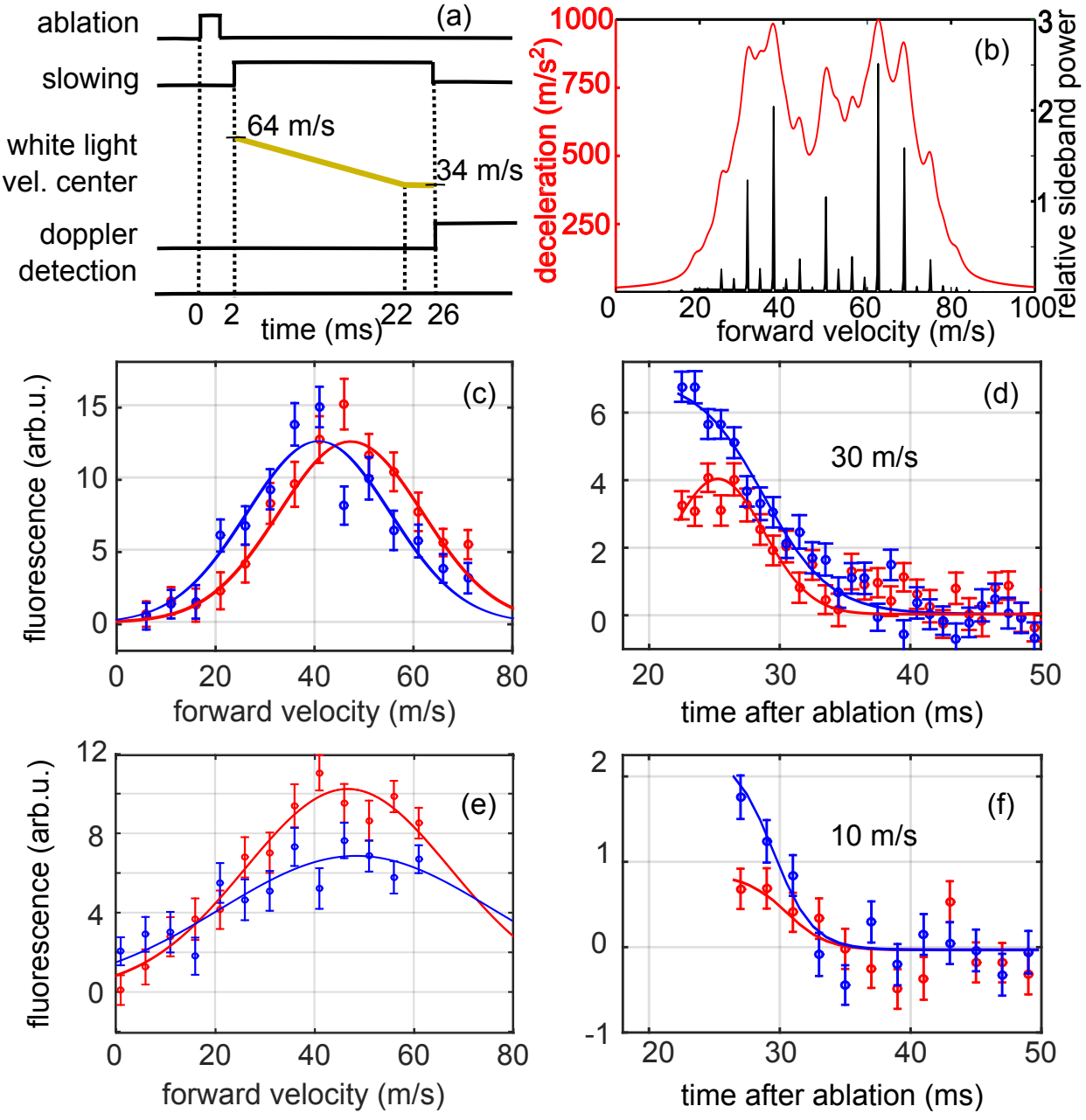

Figure 6.7: (Color online) (a) Timing sequence used to slow molecules to below 10 m/s. (b) Example of spectrally broadened slowing light with center velocity of 50 m/s. Black lines show the sidebands generated from an EOM and rapid polarization switching. The red curve shows molecular deceleration with an optical saturation parameter of 3. (c-f) Comparisons between no slowing in red and with slowing in blue. Solid lines are guides to the eye. (c) Doppler spectra for a 10 ms long slowing sequence. (d) Time of flight for 30 m/s molecules. (e) Doppler spectra for a 24 ms long slowing sequence as depicted in (a). (f) Time of flight for 10 m/s molecules.

Chapter 7

Prospects for a 3D YO MOT.

7.1 3D MOT Coils

As the interaction volume is now only limited to the intersection of the 6 MOT beams, as opposed to the 10 cm long interaction region required for the 2D MOT, the MOT coil design is somewhat simplified. Again in order to maintain sufficient field gradients with the high switching rates, we require the MOT coils to be in vacuum. The coils are made from a commercial composite laminate board designed for rf applications [160]. This consists of a 1.5 mm dielectric material, known as 6035 HTC. The laminate board has thermal conductivity of 1.44 W/(m.K) and has decent outgassing properties. We obtain vacuum pressures on the order of 10^{-8} torr, much smaller than the partial pressure due to the He buffer gas (10^{-6} torr). Rogers boards have been gaining traction as a construction material of surface ion traps (see for example reference [161]). On both sides of the dielectric material a 35 μm layer of copper is electro-deposited.

The MOT coils are set up in the standard anti-Helmholtz configuration. On both side of the Rogers Board, a spiral track is cut into the copper surface, winding 7 times from an outer diameter of 3.4 cm to an inner diameter of 1.9 cm. A 1.8 cm diameter hole is drilled through in the center of the spiral. To maximize the magnetic field gradient, each coil consists of two Roger's boards stacked on top of each other with a thin polyimide film to insulate between the two closest copper faces. The two coil stacks are mounted 2.3 cm apart. This set of coils is run in a similar LC tank configuration as the 2D MOT coils and

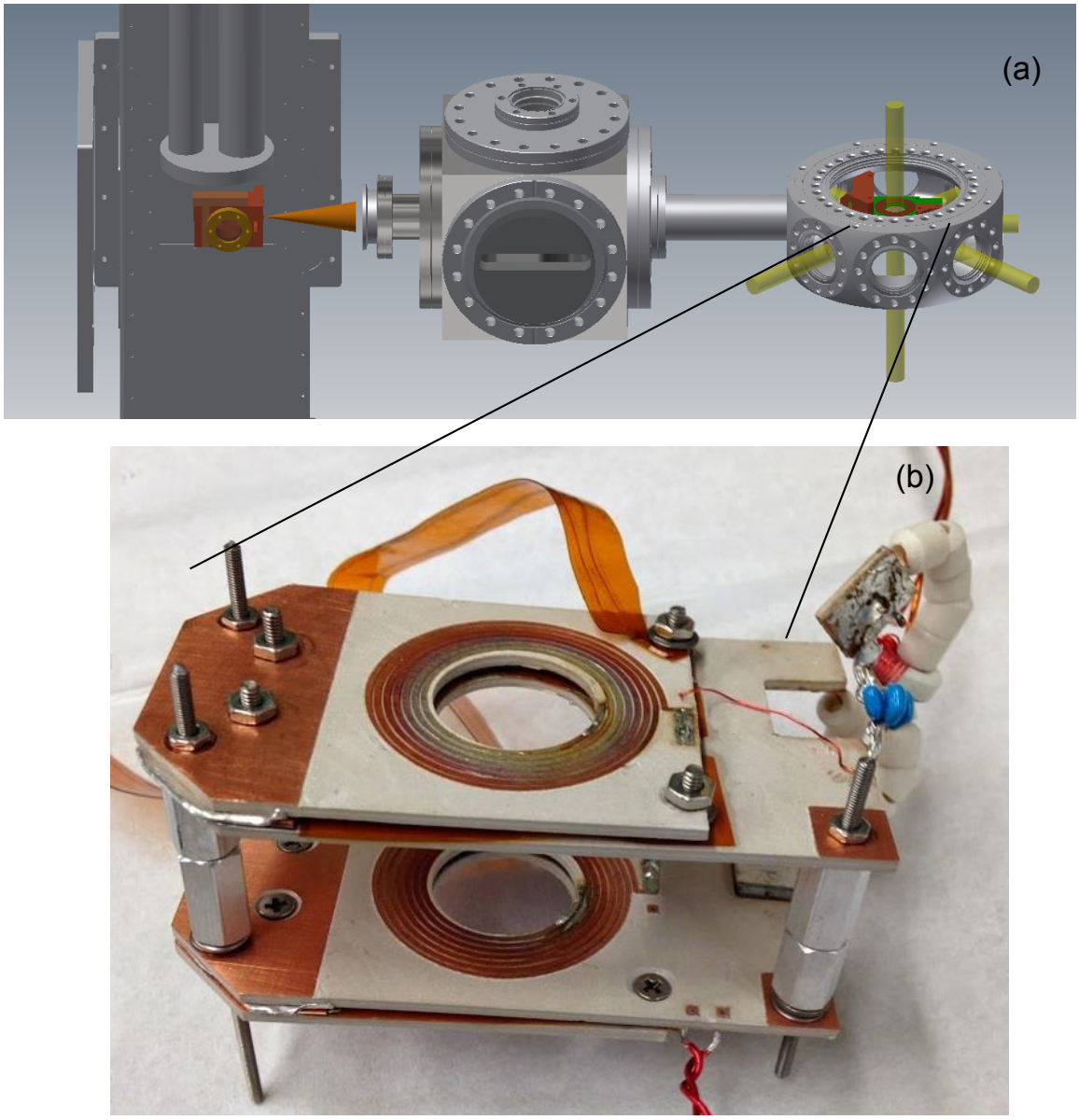

Figure 7.1: 3D MOT apparatus. (a) Machine drawing of 3D MOT apparatus. (b) Photograph of PCB MOT Coils.

we obtain a Q of 70 and a resonance frequency of 5.01 MHz. By coupling in 20 W of rf power at resonance, we expect a magnetic field gradient of 12 G/cm along the cylindrically symmetric quadrupole axis and 6 G/cm perpendicular to this axis.

We expect that the helium pressure limited lifetime to be limited to the He-YO collision rate. The helium pressure rises by 10^{-6} torr when the buffer gas is turned on. Estimating the lifetime using:

$$\tau_{MOT} = (n_{He}\sigma v_{He})^{-1} \tag{7.1}$$

where v_{He} is the thermal velocity of helium at 4 K, $\sim 18 \times 10^3$ cm/s, nHe is the number density which we estimate from the partial pressure to be $\sim 3 \times 10^{10}$ cm^{-3}, and σ is the collision cross section, which is estimated to be 10^{-14} cm^2, the collision cross section measured in previous He-polar molecule collision experiments [56]. This yields an estimated helium density limited MOT lifetime of ∼160 ms.

We have set up a new imaging system for the MOT, allowing us to capture images with a CCD camera. This is illustrated in Figure 7.2 (a). An optical band pass filter system is placed in one of the regions where the light is collimated in order for best performance of the system. An iris is placed at the first image plane to block off scattered light from the in-vacuum MOT coils. Panel (b) depicts an image of the unslowed molecules illuminated by the MOT beams. The camera was taken 10-30 ms after ablation, thus allowing us to observe almost all of the free flying YO packet. As a quick estimate of the molecule number, we estimate the photon collection efficiency η

$$\eta = \eta_q \times \eta_{BP} \times \eta_\Omega \tag{7.2}$$

where $\eta_q \sim 0.9$ is the quantum efficiency for the Apogee Alta U47 CCD camera, $\eta_{BP} \sim 0.93$ the transmission of the Edmund Optics NT84-118 bandpass filter at 614 and $\eta_\Omega \sim 0.04$ the fractional solid angle captured by the imaging system. This results in $\eta \sim 0.02$. Figure 7.2 (b) we subtract the image with molecules from one with no molecules, thus to first order subtracting the background scatter from the MOT beams. In panel (b) the image was taken

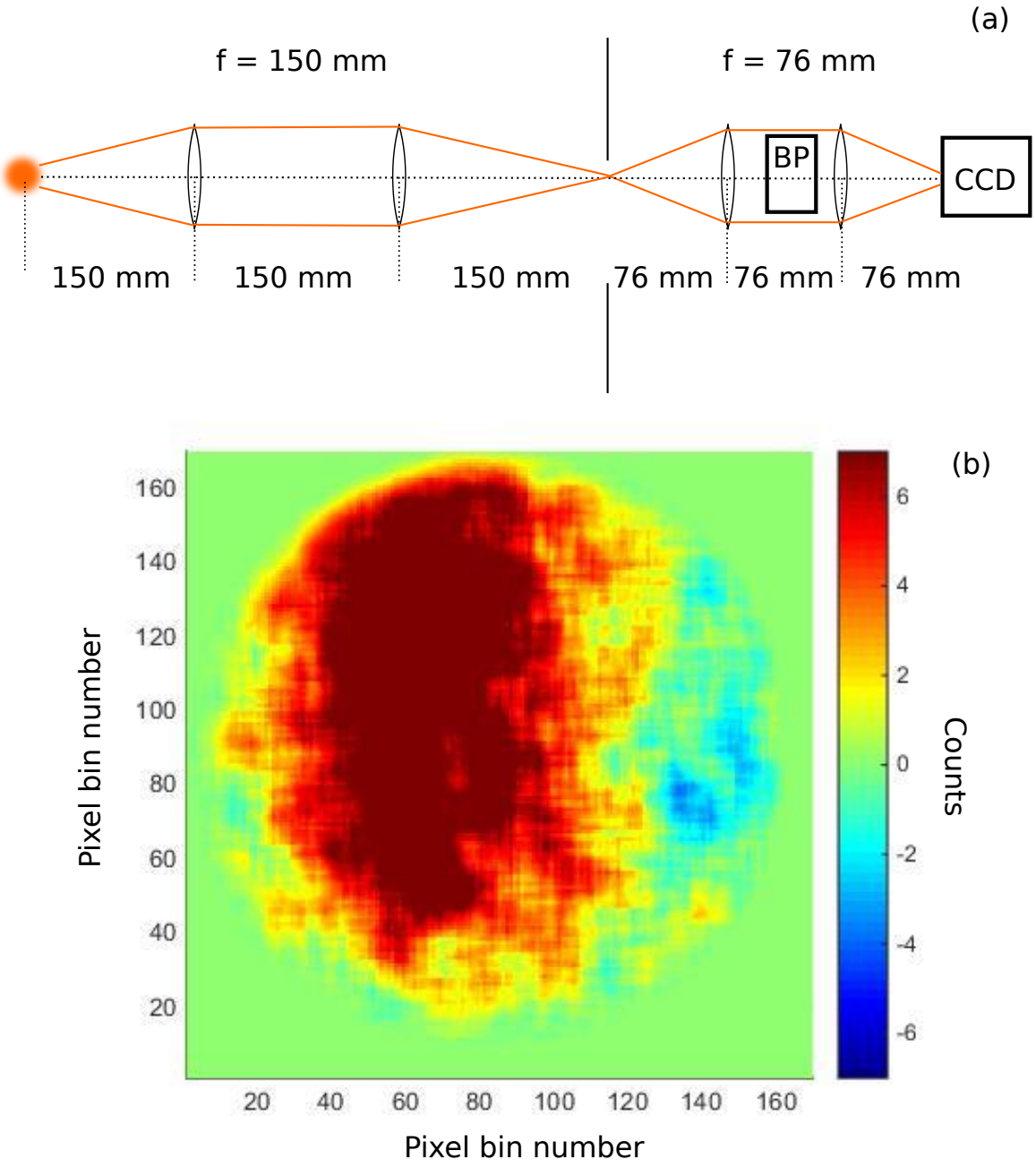

Figure 7.2: (a) Imaging set up with a CCD camera. BP stands for optical bandpass filter. (b) Image of YO molecules in the MOT detection region. The size of the image corresponds to a 1×1 cm object size.

by averaging 400 shots in each state. The total number of counts per shot was found to be 2400 counts, which corresponds to $\sim 7 \times 10^4$ emitted photons.

The conversion to a molecule number is complicated by the fact that the fluorescence is transit time limited. The average 70 m/s molecule travels through the 1 cm beam in 14 μs, giving it enough time to only scatter $\sim$10 photons. This corresponds to approximately 7000 YO molecules. Of course, absolute measurement of molecule number from light induced fluorescence is notoriously difficult [162], as such the preliminary estimate of molecule number should be used with caution.

7.2 A narrow line YO MOT

So far in this thesis, the $A'^2\Delta_{3/2}$ has been cast in a villainous light as it was shown that decays through this state turned out to be the main loss mechanism in our laser cooling scheme. However, it turns out that we can turn this state to our advantage as the much lower linewidth for this state, $2 \times \pi 160$ kHz, allows a much colder MOT with $T_{doppler} \sim 5$ μK [90].

7.2.1 The $A'^2\Delta_{3/2}$ state's linewidth

We use two methods to estimate the linewidth of the $X^2\Sigma^+ \rightarrow A'^2\Delta_{3/2}$ transitions. First as the $A^2\Pi_{1/2} \rightarrow X^2\Sigma^+$ transition linewidth is well known, we can compare the absorption in the cryogenic cell for the respective transitions. The identified transitions from the $G'' = 1$ are tabulated in Table 7.1 and was consistent with the observed transitions in reference [85].

Transition	Frequency (THz)
$N'' = 0, G'' = 1 \rightarrow A'^2\Delta_{3/2}(-)$	434.70310(3)
$N'' = 1, G'' = 1 \rightarrow A'^2\Delta_{3/2}(+)$	434.67989(3)
$N'' = 2, G'' = 1 \rightarrow A'^2\Delta_{3/2}(-)$	434.63333(3)

Table 7.1: Frequencies of $X^2\Sigma^+$ to $A'^2\Delta_{3/2}$ transitions.

To verify that rotational level assignment in the $X^2\Sigma^+$ state, the frequency difference between the $N'' = 0$ and 2 states is indeed 6 times B, the rotational constant in the $X^2\Sigma^+$ state. Therefore we identify the transition at 434.67989(3) THz as the one from the $N'' = 1$ state and compare that absorption to the absorption from the main cooling transition (which of course is from the same $N'' = 1$ state.) We thus obtain a lifetime estimate of $\tau_\Delta = 425$ ns.

The second method to estimate the lifetime involves calculating the state mixing of the $A^2\Pi_{3/2}$ into the $A'^2\Delta_{3/2}$ state. This is because the $A'^2\Delta_{3/2} \rightarrow X^2\Sigma^+$ is E1 forbidden. From the procedure outlined in [78] we can obtain the $A'^2\Delta_{3/2}$ state in terms of Born-Oppenheimer states as

$$\left|\Psi_{A'^2\Delta_{3/2},v'=0}\right\rangle \approx 0.9865\left|A'^2\Delta_{3/2}, v'=0\right\rangle - 0.1582\left|A^2\Pi_{1/2}, v'=0\right\rangle \tag{7.3}$$

$$-0.0369\left|^2\Pi_{3/2}, v'=1\right\rangle + 0.0176\left|A^2\Pi_{1/2}, v'=0\right\rangle + ... \tag{7.4}$$

$$\tag{7.5}$$

The dominant mixing term is a 2.5% mixing with the $\left|^2\Pi_{3/2}, v'=0\right\rangle$ and with the known $\sim$39 ns lifetime of the $A^2\Pi_{3/2}$ state, we estimate from this method a lifetime of 1200 ns. These two methods give similar order estimates of the lifetime, and therefore, we use an intermediate lifetime of 1 μ s for further calculations of the MOT. Table 7.2 compares the characteristic laser cooling temperatures and rms velocities [1] between the main cooling and the new narrow line transition. Most noticeably, we see that Doppler temperature is now a factor of 20 smaller compared to the main cooling transition.

Transition	v_c	T_c	$v_{Doppler}$	$T_{Doppler}$	v_r	T_r
$X^2\Sigma^+ \rightarrow A^2\Pi_{1/2}$	3 m/s	140 mK	9.5 cm/s	116 μK	6.2 mm/s	500 nK
$X^2\Sigma^+ \rightarrow A'^2\Delta_{3/2}$	10 cm/s	150 μK	2 cm/s	4 μK	5.5 mm/s	380 nK

Table 7.2: Comparison of characteristic laser cooling temperature between the main optical cycling and the narrow line transition. Here v_c and T_c are the capture velocity and temperatures respectively, $v_{doppler}$ and $T_{doppler}$ are the Doppler velocity and temperatures respectively and v_r and T_r are the recoil velocity and temperatures respectively

We may derive the vibrational branching from equation 7.3. As transitions between the leading term and the $A^2\Pi_{1/2}$ is dipole forbidden, it is the other states that provide the transition strength and hence the vibrational branching. One may perform the RKR [103] method to calculate the Franck-Condon factors for the $A^2\Pi_{1/2} \rightarrow X^2\Sigma^+$ and $A^2\Pi_{3/2} \rightarrow X^2\Sigma^+$ as described in section 2.5. This results in the branching ratios shown in Table 7.3. We note that the branching ratios from the $A'^2\Delta_{3/2}, v' = 0$ state are not as diagonal as the main cooling transition, however this is not a problem as both the scattering rate and the total photon numbers needed for the cooling are much smaller than for the main transition.

$X^2\Sigma^+, v'' =$	Branching ratio
0	0.9422
1	0.0568
2	0.011
3	$< 10^{-4}$

Table 7.3: Vibrational branching ratios form $A'^2\Delta_{3/2}, v' = 0$ to $X^2\Sigma^+$.

7.3 Narrow-line cooling on the $X^2\Sigma^+$to $A'^2\Delta_{3/2}$transition

Due to the lower scattering rate, this narrow line MOT transition can only be used after the molecules have already been trapped with the normal 614 nm (orange) MOT.

Figure 7.3 (a) shows the YO level structure in the context of a possible narrow line MOT. We choose to excite from the $N'' = 0$ transition in contrast to the orange MOT as this would be a Type-I MOT and the formation of dark Zeeman states is no longer a problem. In the main cooling transition, the $N'' = 0$ rotational is pumped to the $A'^2\Delta_{3/2}, J' = 3/2, p = -$ state and the usual angular momentum selection rules restrict decays back to the $N'' = 0$ and $N'' = 2$ states. Microwave radiation tuned to twice and four times the rotational constant B are used to mix the lowest three rotational states [89], identical to the previous chapter. In addition, the $v'' = 1$ laser used to repump the orange transition can be reused without alteration for the narrow line transition. However, as the vibrational branching in this transition is much larger than that of the $A^2\Pi_{1/2} \rightarrow X^2\Sigma^+$ transition, microwave mixing of higher vibrational also needs to be taken care of. However, as the rotational constants are known [77, 163] (and tabulated in Table 2.1) this should be fairly straightforward with additional microwave frequencies only several 100 MHz smaller than that already used for the orange MOT. The saturation intensity is expected to be $\sim 60\mu\mathrm{W/cm}^2$ and the wavelength at 690 nm is generated with commercially diode lasers.

Figure 7.3 (b) shows two possible type I MOT transitions from the $N'' = 0$ state. The first transition is between the $X^2\Sigma^+, N'' = 1, G'' = 1, F'' = 1, m''_F = -1$ and the $A'^2\Delta_{3/2}, J' = 3/2, F' = 2, m'_F = -2$ states. Here the Landé g factors are shown in the figure and leads to a differential magnetic moment between the upper and lower states of 0.4 μ_B. The other transition occurs between the $G'' = 1, F'' = 0, m''_F = 0$ and the $F' = 1, m'_F = -1$ and differential magnetic moment of $0.2\mu_B$.

7.4 Narrow-line MOT simulation

Monte-Carlo simulations were performed (predominantly by my colleague Alejandra Collopy [90] for this MOT scheme starting from 1 mK YO sample with a trap oscillation frequency of $\omega_{MOT} = 2\pi\times155$ Hz [71], to mimic the conditions of the orange MOT. In addition as v_c is much smaller than the initial root mean square velocity we put on additional frequency sidebands in order address the entire velocity distribution [159,164]. We therefore require 5 frequency sidebands each separated by $2\pi\times1$ MHz with the detuning of the bluest sideband denoted as δ_1. The counter-propagating circular polarized light have two main frequencies to drive both transitions shown in figure 7.3(b). As the hyperfine splitting between $G'' = 1$ and $G'' = 0$ is approximately 760 MHz, only optical branching from the $A'^2\Delta_{3/2}$ state may redistribute population between the two manifolds and these are simulated using the branching ratio of 1:3 into the $G'' = 0$ and $G'' = 1$. The MOT forces are calculated with the methods in Chapter 5, however, as YO is predominantly in the $N'' = 1, 2$ levels, which are not addressed optically, the calculated MOT force must be derated by a factor of 9 due to the ratio of the total number of states in $N'' = 0$ vs the number of states in $N'' = 0, 1, 2$. In addition, heating is simulated by adding a random velocity kick of v_r when a photon is spontaneously emitted. Figure 7.4 shows the results of simulations with δ_1 set at $2\pi \times 240$ kHz (1.5 times the natural linewidth) and a saturation parameter of 3. Panel (a) shows the acceleration vs velocity profile for the optical molasses, i.e. zero B field whilst (b) shows the MOT acceptation on a stationary YO molecule as a function of displacement from the quadruple center. At the low velocity limit, the damping rate is $\Gamma_D = \frac{2\beta}{m_{YO}} = 950$ Hz while the secular frequency ω_{MOT} is found to be $2\pi \times 33$ Hz for a magnetic field gradient of 3 G/cm. The characteristic trapping time then found to be $\Gamma_D/(\omega_{MOT})^2 = 20$ ms. Panel (c) and (d) shows the results of the Monte Carlo simulation. In (c) the initial phase space of the YO molecules is indicated in blue and the phase space distribution of the YO molecules after 20 ms of narrow line MOT action. We see that root mean square velocity decreases by

a factor of 10, implying a decrease in temperature of 100. The spatial distribution becomes $\sim$2 more narrow. This is because while the temperature decreases by a factor of 100, the MOT forces also decrease by a factor of 25 by going to the narrow line. The simulation indicates a photon scatter rate of 10^4 s^{-1} and cooling to the $T_{doppler}$ requires 200 photons. To extrapolate to the full 3D case, again β and ω_{MOT}^2 must be derated by a factor of three and we require 600 photons to cool, which is much less than the inverse of the $v'' \geq 3$ total branching ratio. The $v'' = 3$ lifetime is expected to be on the order of 1s and the expected MOT accelerations are 5 times earth's gravitational acceleration.

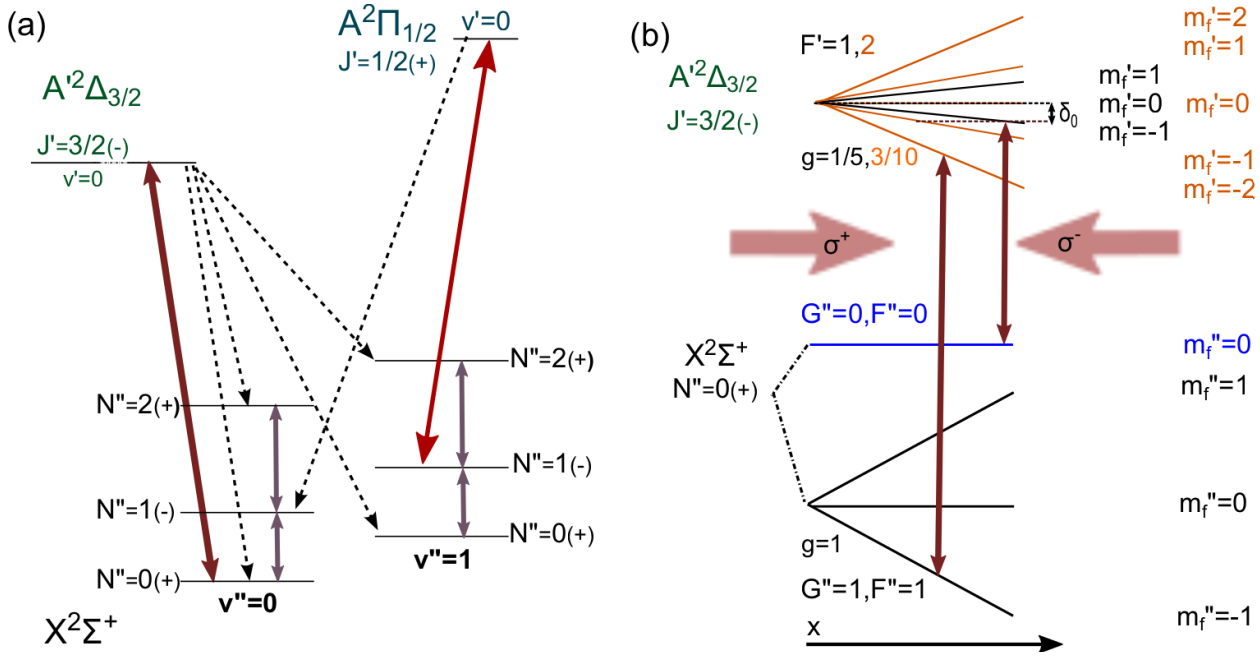

Figure 7.3: Level structure for the narrow-line MOT. (a) Rovibronic structure of the narrow line transition. The maroon arrow indicates the main transition used in the narrow line MOT. Gray lines indicate microwave mixing of rotational states and the red arrow indicates the v''=1 repump, which is the same frequency as used to repump the orange MOT. (b) Zeeman structure and MOT scheme. g represents the corresponding magnetic Landé factor. The large arrows indicate counter propagating circularly polarized laser beams. Both F''=0 $\rightarrow$ F'=1 and F''=1$\rightarrow$$F'$=2 transitions can effect a MOT action (maroon arrows).

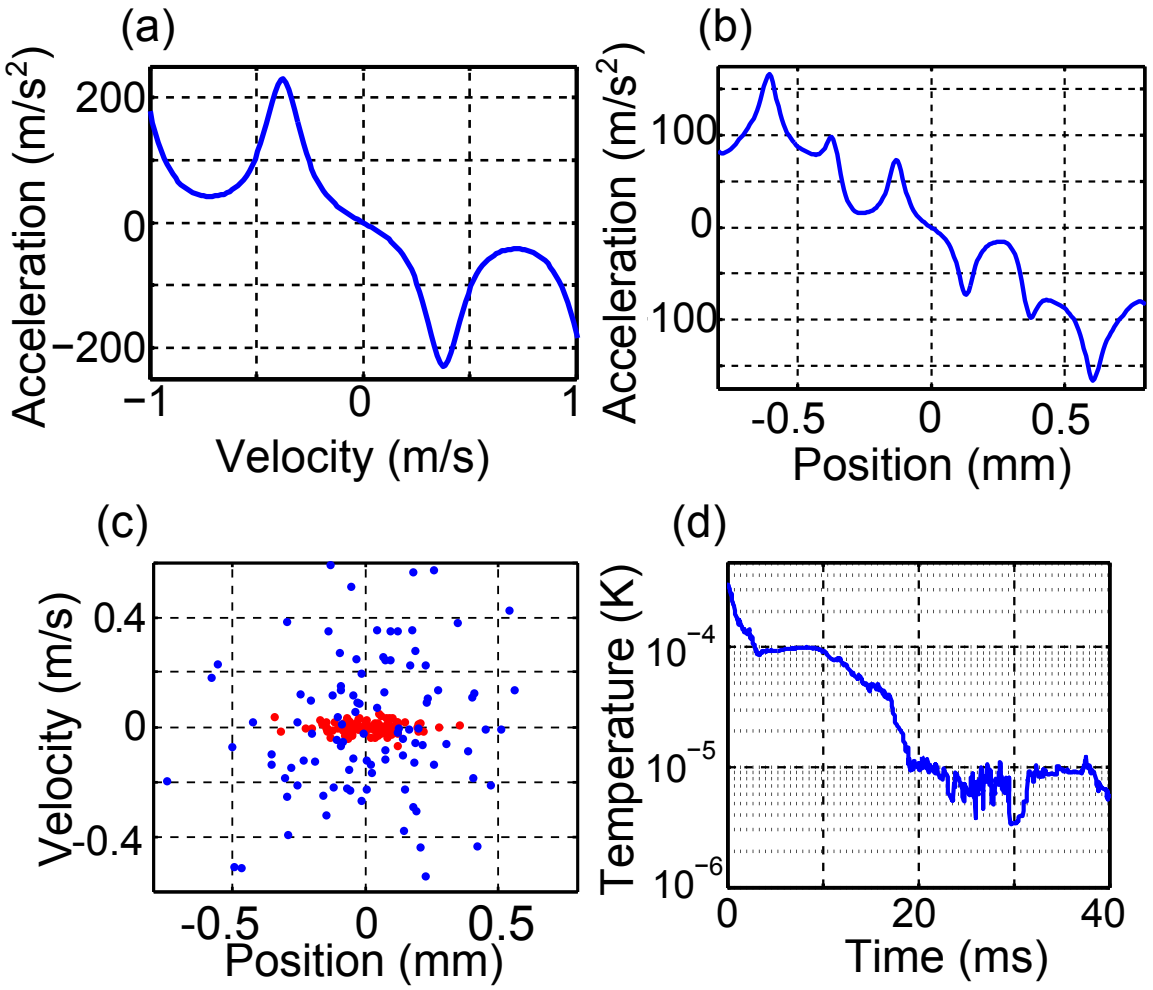

Figure 7.4: Narrow line 1D MOT simulations. (a) Damping acceleration as a function of velocity at zero magnetic field. (b) Restoring MOT acceleration as a function of displacement at zero velocity. (c) Phase space distribution of YO molecule for (blue dots) $X^2\Sigma^+ \rightarrow A^2\Pi_{1/2}$ MOT and (red) $X^2\Sigma^+ \rightarrow A'^2\Delta_{3/2}$ MOT after 20 ms of cooling of this transition. (d) Narrow line MOT temperature as a function of time.

Bibliography

[1] H. J. Metcalf and P. van der Straten, Laser Cooling and Trapping. Springer-Verlag New York, 1999.

[2] M. H. Anderson, J. R. Ensher, M. R. Matthews, C. E. Wieman, and E. A. Cornell, "Observation of Bose-Einstein Condensation in a Dilute Atomic Vapor," Science, vol. 269, no. 5221, pp. 198–201, 1995.

[3] B. DeMarco and D. S. Jin, "Onset of Fermi Degeneracy in a Trapped Atomic Gas," Science, vol. 285, no. 5434, pp. 1703–1706, 1999.

[4] J. R. Guest, N. D. Scielzo, I. Ahmad, K. Bailey, J. P. Greene, R. J. Holt, Z.-T. Lu, T. P. O'Connor, and D. H. Potterveld, "Laser Trapping of ^{225}Ra and ^{226}Ra with Repumping by Room-Temperature Blackbody Radiation," Phys. Rev. Lett., vol. 98, p. 93001, 2007.

[5] I. Bloch, J. Dalibard, and W. Zwerger, "Many-body physics with ultracold gases," Rev. Mod. Phys., vol. 80, pp. 885–964, Jul 2008.

[6] C. Monroe, D. M. Meekhof, B. E. King, W. M. Itano, and D. J. Wineland, "Demonstration of a Fundamental Quantum Logic Gate," Phys. Rev. Lett., vol. 75, pp. 4714–4717, Dec 1995.

[7] M. Saffman, T. Walker, and K. Mølmer, "Quantum information with Rydberg atoms," Rev. Mod. Phys., vol. 82, pp. 2313–2363, Aug 2010.

[8] K. Kim, M.-S. Chang, S. Korenblit, R. Islam, E. E. Edwards, J. K. Freericks, G.-D. Lin, L.-M. Duan, and C. Monroe, "Quantum simulation of frustrated Ising spins with trapped ions," Nature, vol. 465, p. 590593, March 2010.

[9] M. Greiner, O. Mandel, T. Esslinger, T. W. Hänsch, and I. Bloch, "Quantum phase transition from a superfluid to a Mott insulator in a gas of ultracold atoms.," Nature, vol. 415, no. 6867, pp. 39–44, 2002.

[10] D. Budker and M. Romalis, "Optical magnetometry," Nature Physics, vol. 3, pp. 227–234, Apr. 2007.

[11] B. J. Bloom, T. L. Nicholson, J. R. Williams, S. L. Campbell, M. Bishof, X. Zhang, W. Zhang, S. L. Bromley, and J. Ye, "An optical lattice clock with accuracy and stability at the 10^{-18} level.," Nature, vol. 506, pp. 71–5, Feb. 2014.

[12] N. Hinkley, J. A. Sherman, N. B. Phillips, M. Schioppo, N. D. Lemke, K. Beloy, M. Pizzocaro, C. W. Oates, and A. D. Ludlow, "An Atomic Clock with 10^{-18} Instability," Science, vol. 341, no. 6151, pp. 1215–1218, 2013.

[13] A. V. Avdeenkov and J. L. Bohn, "Collisional dynamics of ultracold OH molecules in an electrostatic field," Phys. Rev. A, vol. 66, p. 052718, Nov 2002.

[14] J. L. Bohn, M. Cavagnero, and C. Ticknor, "Quasi-universal dipolar scattering in cold and ultracold gases," New Journal of Physics, vol. 11, no. 5, p. 055039, 2009.

[15] R. V. Krems, "Cold controlled chemistry," Phys. Chem. Chem. Phys., vol. 10, pp. 4079–4092, 2008.

[16] N. Balakrishnan and A. Dalgarno, "Chemistry at ultracold temperatures," Chemical Physics Letters, vol. 341, no. 56, pp. 652 – 656, 2001.

[17] E. R. Hudson, C. Ticknor, B. C. Sawyer, C. A. Taatjes, H. J. Lewandowski, J. R. Bochinski, J. L. Bohn, and J. Ye, "Production of cold formaldehyde molecules for study and control of chemical reaction dynamics with hydroxyl radicals," Phys. Rev. A, vol. 73, p. 063404, Jun 2006.

[18] B. C. Sawyer, B. K. Stuhl, M. Yeo, T. V. Tscherbul, M. T. Hummon, Y. Xia, J. Klos, D. Patterson, J. M. Doyle, and J. Ye, "Cold heteromolecular dipolar collisions," Phys. Chem. Chem. Phys., vol. 13, pp. 19059–19066, 2011.

[19] B. K. Stuhl, M. Yeo, M. T. Hummon, and J. Ye, "Electric-field-induced inelastic collisions between magnetically trapped hydroxyl radicals," Molecular Physics, vol. 111, no. 12-13, pp. 1798–1804, 2013.

[20] S. Ospelkaus, K.-K. Ni, D. Wang, M. H. G. de Miranda, B. Neyenhuis, G. Qumner, P. S. Julienne, J. L. Bohn, D. S. Jin, and J. Ye, "Quantum-State Controlled Chemical Reactions of Ultracold Potassium-Rubidium Molecules," Science, vol. 327, no. 5967, pp. 853–857, 2010.

[21] M. H. G. de Miranda, A. Chotia, N. B., D. Wang, G. Quemener, S. Ospelkaus, J. Bohn J. L.and Ye, and D. S. Jin, "Controlling the quantum stereodynamics of ultracold bimolecular reactions," Nature Phys., vol. 7, no. 6, p. 507, 2011.

[22] M. G. Kozlov and L. N. Labzowsky, "Parity violation effects in diatomics," Journal of Physics B: Atomic, Molecular and Optical Physics, vol. 28, no. 10, p. 1933, 1995.

[23] E. R. Meyer, J. L. Bohn, and M. P. Deskevich, "Candidate molecular ions for an electron electric dipole moment experiment," Phys. Rev. A, vol. 73, p. 062108, Jun 2006.

[24] J. Baron, W. C. Campbell, D. Demille, J. M. Doyle, G. Gabrielse, Y. V. Gurevich, P. W. Hess, N. R. Hutzler, E. Kirilov, I. Kozyryev, B. R. O. Leary, C. D. Panda, M. F. Parsons, E. S. Petrik, B. Spaun, A. C. Vutha, and A. D. West, "Order of Magnitude Smaller Limit on the Electric Dipole Moment of the Electron," Science, vol. 343, pp. 269–273, 2014.

[25] J. J. Hudson, D. M. Kara, I. J. Smallman, B. E. Sauer, M. R. Tarbutt, and E. A. Hinds, "Improved measurement of the shape of the electron.," Nature, vol. 473, pp. 493–6, May 2011.

[26] E. R. Hudson, H. J. Lewandowski, B. C. Sawyer, and J. Ye, "Cold Molecule Spectroscopy for Constraining the Evolution of the Fine Structure Constant," Phys. Rev. Lett., vol. 96, p. 143004, Apr 2006.

[27] T. Zelevinsky, S. Kotochigova, and J. Ye, "Precision Test of Mass-Ratio Variations with Lattice-Confined Ultracold Molecules," Phys. Rev. Lett., vol. 100, p. 043201, Jan 2008.

[28] C. Chin, V. V. Flambaum, and M. G. Kozlov, "Ultracold molecules: new probes on the variation of fundamental constants," New Journal of Physics, vol. 11, no. 5, p. 055048, 2009.

[29] D. DeMille, "Quantum Computation with Trapped Polar Molecules," Phys. Rev. Lett., vol. 88, p. 067901, Jan 2002.

[30] P. Rabl, D. DeMille, J. M. Doyle, M. D. Lukin, R. J. Schoelkopf, and P. Zoller, "Hybrid Quantum Processors: Molecular Ensembles as Quantum Memory for Solid State Circuits," Phys. Rev. Lett., vol. 97, p. 033003, Jul 2006.

[31] B. L. Lev, E. R. Meyer, E. R. Hudson, B. C. Sawyer, J. L. Bohn, and J. Ye, "OH hyperfine ground state: From precision measurement to molecular qubits," Phys. Rev. A, vol. 74, p. 061402, Dec 2006.

[32] H. Büchler, E. Demler, M. Lukin, A. Micheli, N. Prokof'ev, G. Pupillo, and P. Zoller, "Strongly Correlated 2D Quantum Phases with Cold Polar Molecules: Controlling the Shape of the Interaction Potential," Phys. Rev. Lett., vol. 98, p. 060404, Feb 2007.

[33] M. A. Baranov, M. Dalmonte, G. Pupillo, and P. Zoller, "Condensed Matter Theory of Dipolar Quantum Gases," Chemical Reviews, vol. 112, no. 9, pp. 5012–5061, 2012. PMID: 22877362.

[34] J. Doyle, B. Friedrich, R. Krems, and F. Masnou-Seeuws, "Editorial: Quo vadis, cold molecules?," The European Physical Journal D - Atomic, Molecular, Optical and Plasma Physics, vol. 31, no. 2, pp. 149–164, 2004.

[35] D. Wang, J. Qi, M. F. Stone, O. Nikolayeva, H. Wang, B. Hattaway, S. D. Gensemer, P. L. Gould, E. E. Eyler, and W. C. Stwalley, "Photoassociative Production and Trapping of Ultracold KRb Molecules," Phys. Rev. Lett., vol. 93, p. 243005, Dec 2004.

[36] A. J. Kerman, J. M. Sage, S. Sainis, T. Bergeman, and D. DeMille, "Production and State-Selective Detection of Ultracold RbCs Molecules," Phys. Rev. Lett., vol. 92, p. 153001, Apr 2004.

[37] K. Ni, S. Ospelkaus, M. H. G. De Miranda, A. Pe'er, B. Neyenhuis, J. J. Zirbel, S. Kotochigova, P. S. Julienne, D. S. Jin, and J. Ye, "A High Phase-Space-Density Gas of Polar Molecules," Science, vol. 322, no. October, pp. 231–235, 2008.

[38] S. Ospelkaus, A. Pe'er, K. K. Ni, J. J. Zirbel, B. Neyenhuis, S. Kotochigova, P. S. Julienne, J. Ye, and D. S. Jin, "Ultracold dense gas of deeply bound heteronuclear molecules," Nat. Phys., vol. 4, no. August, p. 5, 2008.

[39] C. D. Bruzewicz, M. Gustavsson, T. Shimasaki, and D. DeMille, "Continuous formation of vibronic ground state RbCs molecules via photoassociation," New Journal of Physics, vol. 16, no. 2, p. 023018, 2014.

[40] P. K. Molony, P. D. Gregory, Z. Ji, B. Lu, M. P. Köppinger, C. R. Le Sueur, C. L. Blackley, J. M. Hutson, and S. L. Cornish, "Creation of Ultracold $^{87}Rb^{133}Cs$ Molecules in the Rovibrational Ground State," Phys. Rev. Lett., vol. 113, p. 255301, Dec 2014.

[41] C.-H. Wu, J. W. Park, P. Ahmadi, S. Will, and M. W. Zwierlein, "Ultracold Fermionic Feshbach Molecules of $^{23}Na^{40}K$," Phys. Rev. Lett., vol. 109, p. 085301, Aug 2012.

[42] M. Repp, R. Pires, J. Ulmanis, R. Heck, E. D. Kuhnle, M. Weidemüller, and E. Tiemann, "Observation of interspecies ^{6}Li-^{133}Cs Feshbach resonances," Phys. Rev. A, vol. 87, p. 010701, Jan 2013.

[43] W. Dowd, R. J. Roy, R. K. Shrestha, A. Petrov, C. Makrides, S. Kotochigova, and S. Gupta, "Magnetic field dependent interactions in an ultracold Li-Yb($^3P_2$) mixture," New Jour. Phys., vol. 17, no. 5, p. 055007, 2015.

[44] H. Hara, Y. Takasu, Y. Yamaoka, J. M. Doyle, and Y. Takahashi, "Quantum Degenerate Mixtures of Alkali and Alkaline-Earth-Like Atoms," Phys. Rev. Lett., vol. 106, p. 205304, May 2011.

[45] A. Wakim, P. Zabawa, M. Haruza, and N. P. Bigelow, "Luminorefrigeration: vibrational cooling of NaCs," Opt. Express, vol. 20, pp. 16083–16091, Jul 2012.

[46] S. Y. T. van de Meerakker, N. Vanhaecke, and G. Meijer, "Stark deceleration and trapping of OH radicals.," Annu. Rev. Phys. Chem., vol. 57, pp. 159–90, Jan. 2006.

[47] D. R. Miller, Atomic and Molecular Beam Methods. Oxford University Press, 1988.

[48] J. K. Messer and F. C. De Lucia, "Measurement of Pressure-Broadening Parameters for the CO-He System at 4 K," Phys. Rev. Lett., vol. 53, pp. 2555–2558, Dec 1984.

[49] N. R. Hutzler, H.-I. Lu, and J. M. Doyle, "The buffer gas beam: An intense, cold, and slow source for atoms and molecules," Chem. Rev., vol. 112, no. 9, pp. 4803–4827, 2012.

[50] B. C. Sawyer, B. K. Stuhl, D. Wang, M. Yeo, and J. Ye, "Molecular Beam Collisions with a Magnetically Trapped Target," Phys. Rev. Lett., vol. 101, p. 203203, Nov. 2008.

[51] L. Scharfenberg, K. Gubbels, M. Kirste, G. Groenenboom, A. van der Avoird, G. Meijer, and S. van de Meerakker, "Scattering of Stark-decelerated OH radicals with rare-gas atoms," The European Physical Journal D, vol. 65, no. 1-2, pp. 189–198, 2011.

[52] E. Narevicius, A. Libson, C. G. Parthey, I. Chavez, J. Narevicius, U. Even, and M. G. Raizen, "Stopping Supersonic Beams with a Series of Pulsed Electromagnetic Coils: An Atomic Coilgun," Phys. Rev. Lett., vol. 100, p. 093003, Mar. 2008.

[53] S. Hogan, A. Wiederkehr, H. Schmutz, and F. Merkt, "Magnetic Trapping of Hydrogen after Multistage Zeeman Deceleration," Phys. Rev. Lett., vol. 101, p. 143001, Sept. 2008.

[54] H.-I. Lu, I. Kozyryev, B. Hemmerling, J. Piskorski, and J. M. Doyle, "Magnetic Trapping of Molecules via Optical Loading and Magnetic Slowing," Phys. Rev. Lett., vol. 112, p. 113006, Mar. 2014.

[55] L. P. Parazzoli, N. J. Fitch, P. S. Żuchowski, J. M. Hutson, and H. J. Lewandowski, "Large Effects of Electric Fields on Atom-Molecule Collisions at Millikelvin Temperatures," Phys. Rev. Lett., vol. 106, p. 193201, May 2011.

[56] J. D. Weinstein, R. deCarvalho, T. Guillet, B. Friedrich, and J. M. Doyle, "Magnetic trapping of calcium monohydride molecules at milliKelvin temperatures," Nature, vol. 413, no. September, pp. 396–400, 2001.

[57] S. Y. T. van de Meerakker, N. Vanhaecke, M. P. J. van der Loo, G. C. Groenenboom, and G. Meijer, "Direct Measurement of the Radiative Lifetime of Vibrationally Excited OH Radicals," Phys. Rev. Lett., vol. 95, p. 013003, Jul 2005.

[58] M. Kirste, X. Wang, G. Meijer, K. B. Gubbels, A. van der Avoird, G. C. Groenenboom, and S. Y. T. van de Meerakker, "Communication: Magnetic dipole transitions in the OH A $^2\Sigma^+ \leftarrow$ X $^2\Pi$ system.," J. Chem. Phys., vol. 137, p. 101102, Sept. 2012.

[59] B. K. Stuhl, M. T. Hummon, M. Yeo, G. Quéméner, J. L. Bohn, and J. Ye, "Evaporative cooling of the dipolar hydroxyl radical.," Nature, vol. 492, pp. 396–400, Dec. 2012.

[60] B. K. Stuhl, M. Yeo, B. C. Sawyer, M. T. Hummon, and J. Ye, "Microwave state transfer and adiabatic dynamics of magnetically trapped polar molecules," Phys. Rev. A, vol. 85, p. 033427, Mar 2012.

[61] S. Chervenkov, X. Wu, J. Bayerl, A. Rohlfes, T. Gantner, M. Zeppenfeld, and G. Rempe, "Continuous Centrifuge Decelerator for Polar Molecules," Phys. Rev. Lett., vol. 112, p. 013001, Jan. 2014.

[62] M. Zeppenfeld, B. G. U. Englert, R. Glöckner, A. Prehn, M. Mielenz, C. Sommer, L. D. van Buuren, M. Motsch, and G. Rempe, "Sisyphus cooling of electrically trapped polyatomic molecules.," Nature, vol. 491, pp. 570–3, Nov. 2012.

[63] J. T. Bahns, W. C. Stwalley, and P. L. Gould, "Laser cooling of molecules: A sequential scheme for rotation, translation, and vibration," The Journal of Chemical Physics, vol. 104, no. 24, 1996.

[64] H. W. Chan, A. T. Black, and V. Vuletić, "Observation of Collective-Emission-Induced Cooling of Atoms in an Optical Cavity," Phys. Rev. Lett., vol. 90, p. 063003, Feb 2003.

[65] E. M. Purcell, "Spontaneous Emission Probabilities at Radio Frequencies," Phys. Rev., vol. 69, pp. 681–681, Jun 1946.

[66] B. L. Lev, A. Vukics, E. R. Hudson, B. C. Sawyer, P. Domokos, H. Ritsch, and J. Ye, "Prospects for the cavity-assisted laser cooling of molecules," Phys. Rev. A, vol. 77, p. 023402, Feb 2008.

[67] M. Di Rosa, "Laser-cooling molecules," Eur. Phys. J. D., vol. 31, no. 2, pp. 395–402, 2004.

[68] B. K. Stuhl, B. C. Sawyer, D. Wang, and J. Ye, "Magneto-optical Trap for Polar Molecules," Phys. Rev. Lett., vol. 101, p. 243002, Dec. 2008.

[69] E. S. Shuman, J. F. Barry, D. R. Glenn, and D. DeMille, "Radiative Force from Optical Cycling on a Diatomic Molecule," Phys. Rev. Lett., vol. 103, no. 22, p. 223001, 2009.

[70] E. S. Shuman, J. F. Barry, and D. Demille, "Laser cooling of a diatomic molecule.," Nature, vol. 467, pp. 820–823, Sept. 2010.

[71] M. T. Hummon, M. Yeo, B. K. Stuhl, A. L. Collopy, Y. Xia, and J. Ye, "2D Magneto-Optical Trapping of Diatomic Molecules," Phys. Rev. Lett., vol. 110, p. 14, 2013.

[72] J. F. Barry, D. J. McCarron, E. B. Norrgard, M. H. Steinecker, and D. DeMille, "Magneto-optical trapping of a diatomic molecule," Nature, vol. 512, pp. 286–289, Aug. 2014.

[73] M. R. Tarbutt, "Magneto-optical trapping forces for atoms and molecules with complex level structures," New J. Phys., vol. 17, no. 1, p. 015007, 2015.

[74] D. McCarron, E. Norrgard, M. H. Steinecker, and D. DeMille, "Improved magneto-optical trapping of a diatomic molecule," New Journal of Physics, vol. 17, no. 3, p. 035014, 2015.

[75] V. Zhelyazkova, A. Cournol, T. E. Wall, A. Matsushima, J. J. Hudson, E. A. Hinds, M. R. Tarbutt, and B. E. Sauer, "Laser cooling and slowing of CaF molecules," Phys. Rev. A, vol. 89, p. 053416, May 2014.

[76] W. Jevons, Band-Spectra of Diatomic Molecules. The University Press, Cambridge, 1932.

[77] P. Sriramachandran and R. Shanmugavel, "Spectroscopic parameters for certain band systems of astrophysically important molecule: Yttrium oxide," New Astronomy, vol. 16, pp. 110–113, Feb. 2011.

[78] C. L. Chalek and J. L. Gole, "Chemiluminescence spectra of ScO and YO: Observation and analysis of the $A^2\Delta$ $X\Sigma$ band system," J. Chem. Phys., vol. 65, p. 2845, 1976.

[79] C. L. Chalek and J. L. Gole, "Single collision chemiluminescence studies of scandium and yttrium oxidation with O_2, NO_2, N_2O and O_3," Chemical Physics, vol. 19, pp. 59–90, Jan. 1977.

[80] A. Bernard and R. Gravina, "Further analysis of the $B^2\Sigma^+ \rightarrow X^2\Sigma^+$ System of the YO Molecule," Astrophys. J. Supp. Ser., vol. 44, pp. 223–239, 1980.

[81] A. Bernard and R. Gravina, "The emission spectrum of yttrium monoxide-New rotational and vibrational results on the A $^2\Pi$-X $^2\Sigma^+$ system," Astrophys. J. Suppl. Ser., vol. 52, p. 443, 1983.

[82] S. R. Langhoff and C. W. Bauschlicher, "Theoretical studies of the monoxides and monosulfides of Y, Zr, and Nb," J. Chem. Phys., vol. 89, p. 2160, 1988.

[83] T. C. Steimle and J. E. Shirley, "A molecular beam-optical Stark study of the A $^2\Pi$-X $^2\Sigma$ band system of YO," J. Chem. Phys., vol. 92, p. 3292, 1990.

[84] R. D. Suenram, F. J. Lovas, G. T. Fraser, and K. Matsumura, "Pulsed-nozzle Fourier-transform microwave spectroscopy of laser-vaporized metal oxides: Rotational spectra and electric dipole moments of YO, LaO, ZrO, and HfO," The Journal of Chemical Physics, vol. 92, p. 4724, 1990.

[85] B. Simard, A. M. James, and P. A. Hackett, "On the $A'^2\Delta$-$X^2\Sigma^+$(0,0) Band of YO," Journal of Molecular Spectroscopy, vol. 154, pp. 455–457, 1992.

[86] J. Hoeft and T. Törring, "The microwave rotational spectrum of X $^2\Sigma^+$ YO," Chemical Physics Letters, vol. 215, pp. 367–370, Dec. 1993.

[87] B. Simard, J. K. G. Watson, A. J. Merer, and T. C. Steimle, "Comment on "Fine and magnetic hyperfine structure in the A Π and X Σ states of yttrium monoxide."," The Journal of Chemical Physics, vol. 111, no. 13, pp. 6148–6149, 1999.

[88] J.-H. Leung, T. Ma, and A. Cheung, "Cavity ring down absorption spectroscopy of the $B^2\Sigma$-$X^2\Sigma$+ transition of YO," Journal of Molecular Spectroscopy, vol. 229, pp. 108–114, Jan. 2005.

[89] M. Yeo, M. Hummon, A. Collopy, B. Yan, B. Hemmerling, E. Chae, J. Doyle, and J. Ye, "Rotational state microwave mixing for laser cooling of complex diatomic molecules," Phys. Rev. Lett., accepted for publication in 2015.

[90] A. L. Collopy, M. H. Hummon, M. Yeo, B. Yan, and J. Ye, "Prospects for a narrow line MOT in YO," New Journal of Physics, vol. 17, no. 5, p. 055008, 2015.

[91] F. Hund, "Allgemeine Quantenmechanik des Atom und Molekelbaues," Quantentheorie, vol. 2, pp. 561–694, 1933.

[92] J. M. Brown and A. Carrington, Rotational Spectroscopy of Diatomic Molecules. Cambridge University Press, 2003.

[93] K. Liu and J. M. Parson, "Laser fluorescence detection of nascent product state distributions in reactions of Sc and Y with O_2, NO, and SO_2," J. Chem. Phys., vol. 67, p. 1814, 1977.

[94] R. A. Frosch and H. M. Foley, "Magnetic Hyperfine Structure in Diatomic Molecules," Phys. Rev., vol. 88, pp. 1337–1349, Dec 1952.

[95] W. J. Childs, O. Poulsen, and T. C. Steimle, "Fine and magnetic hyperfine structure in the $A^2\Pi$ and $X^2\Sigma^+$ states of yttrium monoxide," J. Chem. Phys., vol. 88, p. 598, 1988.

[96] R. S. Mulliken and A. Christy Phys, Rev., vol. 38, p. 87, 1931.

[97] O. Appelblad, "Centrifugal Distortion in the Spin-Orbit Coupling in the $^2\Pi$ Ground State of CuO," Phys. Scr, vol. 25, p. 375, 1982.

[98] G. Herzberg, Molecular Spectra and Molecular Structure . D. Van Nostrand Company, 2 ed., 1950.

[99] R. F. Curl, "The relationship between electron spin rotation coupling constants and g-tensor components," Mol. Phys., vol. 9, no. 6, pp. 585–597, 1965.

[100] J. M. Brown, M. Kaise, C. M. L. Kerr, and D. J. Milton, "A determination of fundamental Zeeman parameters for the OH radical," Molecular Physics, vol. 36, no. 2, pp. 553–582, 1978.

[101] J. Rydberg Ann. Physik., vol. 13, p. 376, 1931.

[102] O. Klein Ann. Physik., vol. 76, p. 226, 1932.

[103] A. L. G. Rees, "The calculation of potential-energy curves from band-spectroscopic data," Proceedings of the Physical Society, vol. 59, no. 6, p. 998, 1947.

[104] J. F. Barry, E. S. Shuman, E. B. Norrgard, and D. DeMille, "Laser Radiation Pressure Slowing of a Molecular Beam," Phys. Rev. Lett., vol. 108, p. 103002, Mar. 2012.

[105] M. J. Thorpe, Cavity-enhanced direct frequency comb spectroscopy. PhD thesis, University of Colorado, Boulder, 2009.

[106] S. A. Diddams, "The evolving optical frequency comb," J. Opt. Soc. Am. B, vol. 27, pp. B51–B62, Nov 2010.

[107] J. Ye, H. Schnatz, and L. W. Hollberg, "Optical frequency combs: from frequency metrology to optical phase control," IEEE Journal of Selected Topics in Quantum Electronics, vol. 9, no. 4, pp. 1041–1058, 2003.

[108] S. M. Foreman, Femtosecond Frequency Combs for Optical Clocks and Timing Transfer. PhD thesis, University of Colorado, Boulder, 2007.

[109] W. Miniscalco, "Erbium-doped glasses for fiber amplifiers at 1500 nm," Journal of Lightwave Technology, vol. 9, pp. 234–250, Feb 1991.

[110] K. Tamura, H. Haus, and E. Ippen, "Self-starting additive pulse mode-locked erbium fibre ring laser," Electronics Letters, vol. 28, pp. 2226–2228(2), November 1992.

[111] H. A. Haus, K. Tamura, L. E. Nelson, and E. P. Ippen, "Stretched-pulse additive pulse mode-locking in fiber ring lasers: theory and experiment," Quantum Electronics, IEEE Journal of, vol. 31, pp. 591–598, Mar 1995.

[112] T. Okuno, M. Onishi, T. Kashiwada, S. Ishikawa, and M. Nishimura, "Silica-based functional fibers with enhanced nonlinearity and their applications," IEEE Journal on Selected Topics in Quantum Electronics, vol. 5, no. 5, pp. 1385–1391, 1999.

[113] F. Tauser, F. Adler, and A. Leitenstorfer, "Widely tunable sub-30-fs pulses from a compact erbium-doped fiber source.," Optics letters, vol. 29, no. 5, pp. 516–518, 2004.

[114] E. Desurvire, J. R. Simpson, and P. C. Becker, "High-gain erbium-doped traveling-wave fiber amplifier," Opt. Lett., vol. 12, pp. 888–890, Nov 1987.

[115] S. T. Cundiff, T. M. Fortier, D. J. Jones, and J. Ye, "Phase stabilization of modelocked lasers," Postconference Digest Quantum Electronics and Laser Science, 2003. QELS., 2003.

[116] D. J. Jones, S. A. Diddams, J. K. Ranka, A. Stentz, R. S. Windeler, J. L. Hall, and S. T. Cundiff, "Carrier-envelope phase control of femtosecond mode-locked lasers and direct optical frequency synthesis," Science, vol. 288, pp. 635–639, 2000-04 2000. JILA Pub. 6467.

[117] F. Adler, K. Moutzouris, A. Leitenstorfer, H. Schnatz, B. Lipphardt, and G. Grosche, "Phase-locked two-branch erbium-doped fiber laser system for long-term precision measurements of optical frequencies," Optics Express, vol. 12, no. 24, pp. 250–252, 2004.

[118] "Matisse User's Guide." http://www.spectra-physics.com/documents/service/user-manuals/Matisse%20Users%20Guide%20Rev.%201.8.pdf.

[119] A. L. Bloom, "Modes of a laser resonator containing tilted birefringent plates," J. Opt. Soc. Am., vol. 64, pp. 447–452, Apr 1974.

[120] "Continous Wave Visisble Fiber Lasers." http://www.mpbcommunications.com/.

[121] E. M. Dianov, "Advances in Raman fibers," Journal of Lightwave Technology, vol. 20, pp. 1457–1462, Aug. 2002.

[122] "External-cavity Diode Lasers." http://www.rp-photonics.com/external_cavity_diode_lasers.html.

[123] J. Barry, Laser cooling and slowing of a diatomic molecule. PhD thesis, Yale University, 2013.

[124] W. C. Campbell and J. M. Doyle, Cold Molecules: Theory, Experiment, Applications. CRC Press: Boca Raton, FL, 2009.

[125] N. Balakrishnan, G. C. Groenenboom, R. V. Krems, and A. Dalgarno, "The He-CaH interaction. II. Collisions at cold and ultracold temperatures," The Journal of Chemical Physics, vol. 118, no. 16, 2003.

[126] H. Le, R. Dreyfus, W. Marine, M. Sentis, and I. Movtchan, "Temperature measurements during laser ablation of Si into He, Ar and O_2. ," Applied Surface Science, vol. 9698, no. 0, pp. 164 – 169, 1996. Proceedings of Symposium F: Third International Symposium on Laser Ablation of the 1995 E-MRS Spring Conference.

[127] "Cryomech PT407 Product Page." http://www.cryomech.com/products/cryorefrigerators/pulse-tube/pt407/.

[128] J. F. Barry, E. S. Shuman, and D. DeMille, "A bright, slow cryogenic molecular beam source for free radicals," Phys. Chem. Chem. Phys., vol. 13, pp. 18936–18947, 2011.

[129] N. R. Hutzler, M. F. Parsons, Y. V. Gurevich, P. W. Hess, E. Petrik, B. Spaun, A. C. Vutha, D. DeMille, G. Gabrielse, and J. M. Doyle, "A cryogenic beam of refractory, chemically reactive molecules with expansion cooling,"

[130] J. W. Ekin, Experimental Techniques for Low-Temperature Measurements. Oxford University Press, 2006.

[131] F. Pobell, Matter and Methodds at Low Temperatures. Springer-Verlag Berlin Heidelberg New York, 2 ed., 1996.

[132] B. C. Sawyer, Cold polar molecules for novel collision experiments at low energies. PhD thesis, University of Colorado, Boulder, 2010.

[133] D. Patterson and J. M. Doyle, "Bright, guided molecular beam with hydrodynamic enhancement," The Journal of Chemical Physics, vol. 126, no. 15, pp. –, 2007.

[134] H.-I. Lu, J. Rasmussen, M. J. Wright, D. Patterson, and J. M. Doyle, "A cold and slow molecular beam," Phys. Chem. Chem. Phys., vol. 13, pp. 18986–18990, 2011.

[135] W. Campbell, Magnetic Trapping of Imidogen Molecules. PhD thesis, Harvard University, 2008.

[136] A. Roth, Vacuum Technology. North-Holland Pub. Co., 2 ed., 1990.

[137] "Turbo-V Pumps." http://www.idealvac.com/files/manualsII/Varian_V70.pdf.

[138] D. Wineland and H. Dehmelt, "Proposed 10^{14} $\Delta\nu < \nu$ laser fluorescence spectroscopy on Tl^+ mono-ion oscillator," Bull. Am. Phys. Soc., vol. 20, p. 637, 1975.

[139] T. W. Hänsch and A. L. Schawlow, "Cooling of gases by laser radiation.," Optics Communications, vol. 13, no. 1, pp. 68 – 69, 1975.

[140] D. J. Wineland, R. E. Drullinger, and F. L. Walls, "Radiation-Pressure Cooling of Bound Resonant Absorbers," Phys. Rev. Lett., vol. 40, pp. 1639–1642, Jun 1978.

[141] E. L. Raab, M. Prentiss, A. Cable, S. Chu, and D. E. Pritchard, "Trapping of Neutral Sodium Atoms with Radiation Pressure," Phys. Rev. Lett., vol. 59, no. 23, pp. 2631–2634, 1987.

[142] P. D. Lett, W. D. Phillips, S. L. Rolston, C. E. Tanner, R. N. Watts, and C. I. Westbrook, "Optical molasses," J. Opt. Soc. Am. B, vol. 6, pp. 2084–2107, Nov 1989.

[143] W. D. Phillips, "Nobel Lecture: Laser cooling and trapping of neutral atoms," Reviews of Modern Physics, vol. 70, no. 3, pp. 721–741, 1998.

[144] V. B. Tiwari, S. Singh, H. S. Rawat, and S. C. Mehendale, "Cooling and trapping of ^{85}Rb atoms in the ground hyperfine $F = 2$ state," Phys. Rev. A, vol. 78, p. 063421, Dec 2008.

[145] J. Flemming, A. Tuboy, D. Milori, L. Marcassa, S. Zilio, and V. Bagnato, "Magneto-optical trap for sodium atoms operating on the D_1 line," Optics Communications, vol. 135, no. 46, pp. 269 – 272, 1997.

[146] K. Nasyrov, V. Biancalana, A. Burchianti, R. Calabrese, C. Marinelli, E. Mariotti, and L. Moi, "Magneto-optical trap operating on a magnetically induced level-mixing effect," Phys. Rev. A, vol. 64, p. 023412, Jul 2001.

[147] M. Prentiss, E. L. Raab, D. E. Pritchard, A. Cable, J. E. Bjorkholm, and S. Chu, "Atomic-density-dependent losses in an optical trap," Opt. Lett., vol. 13, pp. 452–454, Jun 1988.

[148] M. Fox, Quantum Optics An Introduction. Oxford University Press, 2006.

[149] J. Dalibard and C. Cohen-Tannoudji, "Laser cooling below the Doppler limit by polarization gradients: simple theoretical models," Journal of the Optical Society of America B, vol. 6, no. 11, p. 2023, 1989.

[150] D. J. Berkeland and M. G. Boshier, "Destabilization of dark states and optical spectroscopy in Zeeman-degenerate atomic systems," Phys. Rev. A, vol. 65, pp. 1–13, Feb. 2002.

[151] M. Harvey and A. J. Murray, "Cold Atom Trap with Zero Residual Magnetic Field: The ac Magneto-Optical Trap," Phys. Rev. Lett., vol. 101, p. 173201, Oct 2008.

[152] J. L. Roberts, Bose-Einstein Condensates with Tunable Atom-atom Interactions. PhD thesis, University of Colorado, Boulder, 2001.

[153] B. Hemmerling, G. K. Drayna, E. Chae, A. Ravi, and J. M. Doyle, "Buffer gas loaded magneto-optical traps for Yb, Tm, Er and Ho," New Journal of Physics, vol. 16, no. 6, p. 063070, 2014.

[154] W. Phillips and H. Metcalf, "Laser Deceleration of an Atomic Beam," Phys. Rev. Lett., vol. 48, pp. 596–599, Mar 1982.

[155] N. Vanhaecke and O. Dulieu, "Precision measurements with polar molecules: the role of the black body radiation," Mol. Phys., vol. 105, pp. 1723–1731, June 2007.

[156] B. D. Brandsen and C. J. Joachain, Physics of Atoms and Molecules. Prentice Hall, 2 ed., 2003.

[157] A. R. Allouche, G. Wannous, and M. Aubert-Frécon, "A ligand-field approach for the low-lying states of Ca, Sr and Ba monohalides," Chem. Phys., vol. 170, pp. 11–22, 1993.

[158] M. Zhu, C. W. Oates, and J. L. Hall, "Continuous High-Flux Monovelocity Atomic-Beam Based on a Broad-Band Laser Cooling Technique," Phys. Rev. Lett., vol. 67, pp. 46–49, 1991.

[159] T. H. Loftus, T. Ido, A. D. Ludlow, M. M. Boyd, and J. Ye, "Narrow Line Cooling: Finite Photon Recoil Dynamics," Phys. Rev. Lett., vol. 93, p. 073003, Aug 2004.

[160] "6035HTC High Frequency Laminate." https://www.rogerscorp.com/documents/1946/acs/RT-duroid-6035HTC-High-Frequency-Laminates.pdf.

[161] R. D. Graham, S.-P. Chen, T. Sakrejda, J. Wright, Z. Zhou, and B. B. Blinov, "A system for trapping barium ions in a microfabricated surface trap," AIP Advances, vol. 4, no. 5, 2014.

[162] Y. Matsumi, M. Kono, T. Ichikawa, K. Takahashi, and Y. Kondo, "Laser-Induced Fluorescence Instrument for the Detection of Tropospheric OH Radicals," Bulletin of the Chemical Society of Japan, vol. 75, no. 4, pp. 711–717, 2002.

[163] A. Bernard, R. Bacis, and P. Luc, "Fourier Transform Spectroscopy: Extensive analysis of the $A^2\Pi \rightarrow X^2\Sigma^+$ and $B^2\Sigma^+ \rightarrow X^2\Sigma^+$ Systems of Yttrium Oxide," The Astrophysical Journal, vol. 227, pp. 338–348, 1979.

[164] T. H. Loftus, T. Ido, M. M. Boyd, A. D. Ludlow, and J. Ye, "Narrow line cooling and momentum-space crystals," Phys. Rev. A, vol. 70, p. 063413, Dec 2004.

[165] R. Michniak, Enhanced Buffer Gas Loading. PhD thesis, Harvard University, 2004.

[166] D. E. Knuth, Seminumerical Algorithms. The Art of Computer Programming, vol. 2. Addison Wesley, 1969.

[167] L. Verlet, "Computer "Experiments" on Classical Fluids. I. Thermodynamical Properties of Lennard-Jones Molecules," Phys. Rev., vol. 159, pp. 98–103, Jul 1967.

[168] J. B. Hasted, Physics of Atomic Collisions. Butterworth and Co., 1964.

[169] S. Chapman and T. Colwing, The Mathematical Theory of Non-uniform Gases. Cambridge University Press, 1952.

Appendices

Appendix 1

He-YO collisions simulations

This appendix describes the simulation technique used to model the He-YO collisions. Much of this work is inspired by Robert Michniak's thesis [165]

First, we look at elastic collisions between the buffer gas and the YO molecules. In our trap, we will tend to get a wide variety of impact parameters as well as collision energies. Since we do not know the differential cross section (DCS) a priori, we will assume an isotropic one. In this simulation, the helium atoms' trajectories are not tracked.

Since the density of YO is much smaller than the density of Helium, the elastic cross section rate is given by

$$\gamma = n_{He}\sigma_{el}v_{rel} \tag{1.1}$$

where n_{He} is the buffer gas density, σ_{el} is the elastic cross section between He and YO and v_{rel} is the relative velocity between the two species. The reciprocal of this gives a characteristic time of collisions. YO molecules are assumed to not interact with each other. The collision time is assumed to follow a Poissonian process with mean inter-collision time set to be $\tau_{col} = 1/\gamma$. The probability distribution of collision times is proportional to $e^{-t_{col}/\tau_{col}}$. To generate this we use the following prescription [166]:

$$t_{col} = \tau_{col}\ln(1 - rand) \tag{1.2}$$

where $rand$ is uniformly distributed random number between 0 and 1.

Therefore, each YO molecule will evolve for the time t_{col} according to the MOT forces. When a collision occurs, we do the following: a helium atom is generated with a random

velocity consistent with the Maxwell-Boltzmann distribution. We transform to the He-YO center of mass frame and randomize the YO velocity direction as we assume an isotropic collision cross section. We then transform back to the lab frame and generate a new collision time and repeat the process.

1.1 Simulation Results.

We perform these simulations in FORTRAN 95, using a quasi-fixed step symplectic integrator [167]. In order to correctly simulate the MOT forces, time steps are restricted to be no more than 100 ns. The time steps are reduced when the randomly generated t_{col} drops to below the 100 ns time step.

The first test is to turn off collisions and compare the analytic solution of the damped harmonic oscillator with our numerical solution. The results are shown in figure A1 and are self consistent.

The next step is to add in elastic collisions. As a consistency check, we compare our simulation with no MOT forces and at various helium densities and compare to the analytic diffusion time constant for a cylinder as given by [168]:

$$\tau = ((\frac{2.4}{R})^2 + (\frac{\pi}{L})^2)^{-1} \frac{1}{D} \tag{1.3}$$

where D is the diffusion constant for a binary gas given by the Chapman Enskog formula [169]:

$$D = \frac{3}{16 n_{He} \sigma_d} \sqrt{\frac{2\pi k_B T}{\mu}} \tag{1.4}$$

where σ_d is the momentum transfer cross which in the case of an isotropic DCS, is the same as the elastic collision cross section. We can calculate the diffusion with Equation 1.3 for a cylinder with 1.5 cm radius and 3 cm height. We obtain a diffusion time constant of 2.8(5.6) ms for a helium density of $n_{He} = 5 \times 10^{15}(10^{16})$ cm^{-3}.

We performed a simulation of the YO molecules in these two density regimes as shown in figure A2. Here a uniform density of YO molecules is initialized and allowed to collide

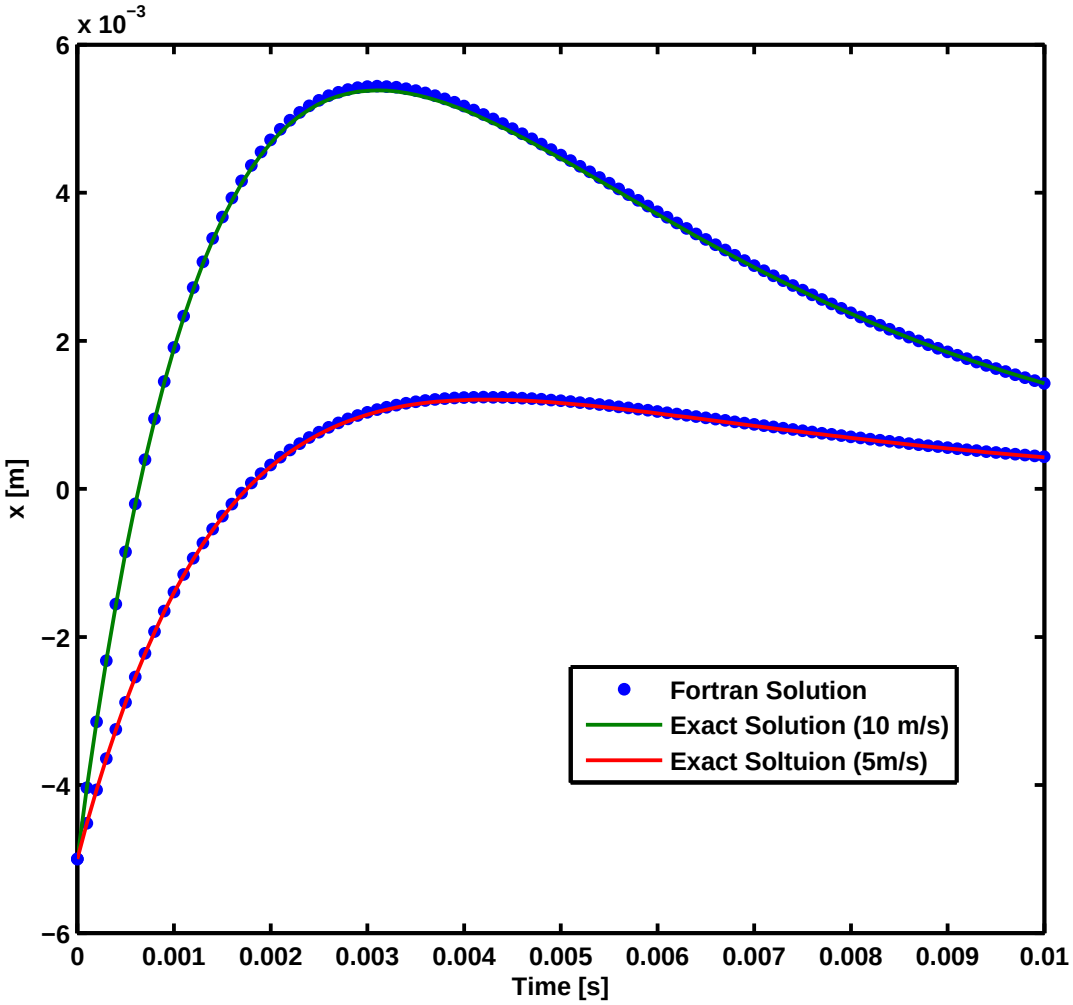

Figure A1: Simulation of YO trajectory with no helium collisions. Solid lines are analytic solution while points are calculated using the Fortran symplectic integrator.

elastically with the 4 K molecules. Upon striking the boundary of the aforementioned cylinder, the YO molecule is lost. The resultant time constants are 2.4(4.3) ms for helium density of $5 \times 10^{15}(10^{16})cm^{-3}$, consistent with the analytic prediction from Equation 1.3. Therefore we conclude that our elastic collision protocol is indeed working.

Finally, we consider rotational collisions. We assumed that the collisions may change the rotational state by $\Delta N'' = \pm 1$ or the molecule remains in the same rotational state. The algorithm proceeds as follows.

1.) Upon collision, we calculate the center of mass collision energy E_{col} given by $E_{col} = \frac{1}{2}\mu_{red} v_{rel}^2$.

2.) In order for the collision to excite the molecule to the next highest rotational state, conservation of energy dictates that $E_col > 2(N''+1)\hbar B$ where B is the rotational constant. If the equality is satisfied, we proceed to 3a, otherwise we jump to step 3b.

3a) The number of states in each rotational level is given by $8N''+4$. If there is sufficient energy for rotational excitation, we then excite to $N''+1$ with probability $(3+2N'')/(3+6N'')$, relax to $N''-1$ with probability $(-1+2N'')/(3+6N'')$ or stay put at N'' with probability $1/3$.

3b) In the case where we cannot excite, the rotational state relaxes to $N''-1$ with probability $(2N''-1)/(4N'')$ or stays put at N'' with probability $(2N''+1)/(4N'')$.

4.) The magnitude of the relative COM velocity is reduced or increased appropriately in order to conserve energy if a rotational transition does occur.

Using this crude approximation for rotational collisions, we calculate the rotational distribution and as shown in figure A3, we can still obtain good agreement with the Boltzmann rotational distribution.

Putting these pieces together we were able to calculate the expected lifetimes as discussed in section 6.1.2 for the various helium densities.

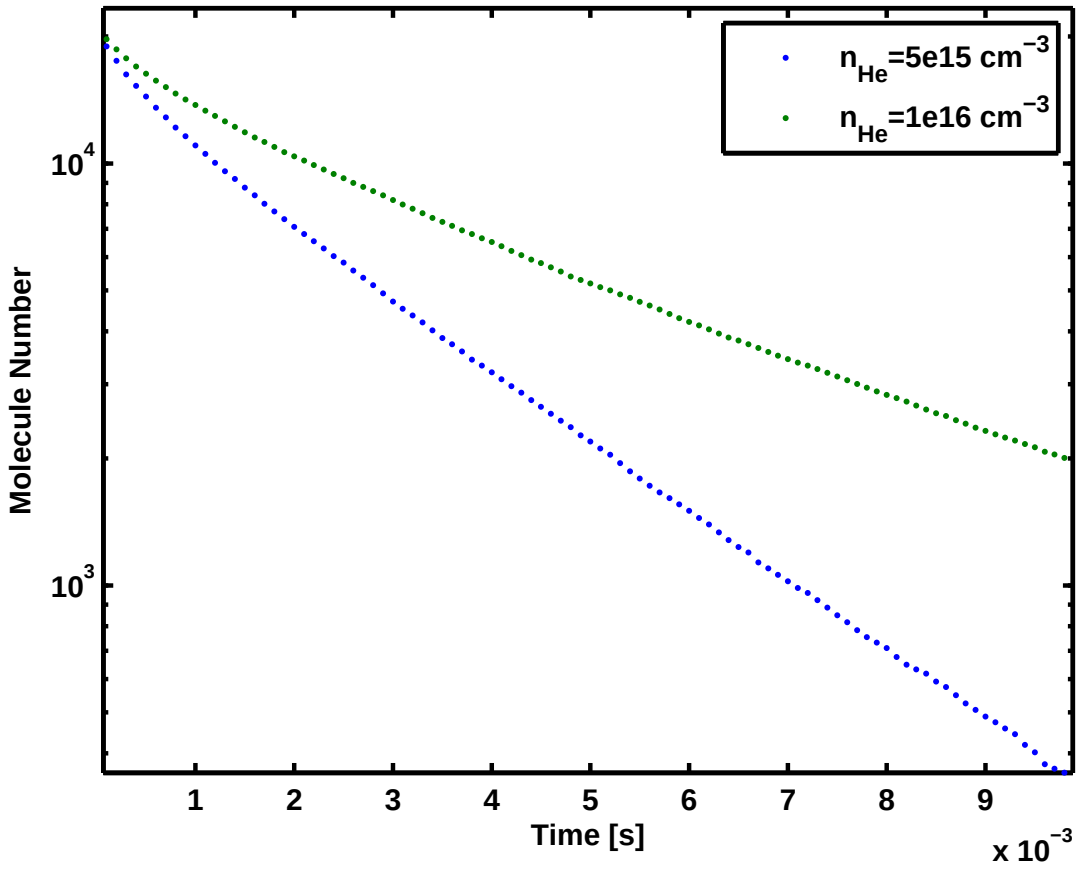

Figure A2: Simulation of YO number in a cylinder with two different densities with no MOT force and with elastic helium collisions. The extracted diffusion time constants are 2.4(4.3) ms for helium density of $5 \times 10^{15}(10^{16})$ cm^{-3}

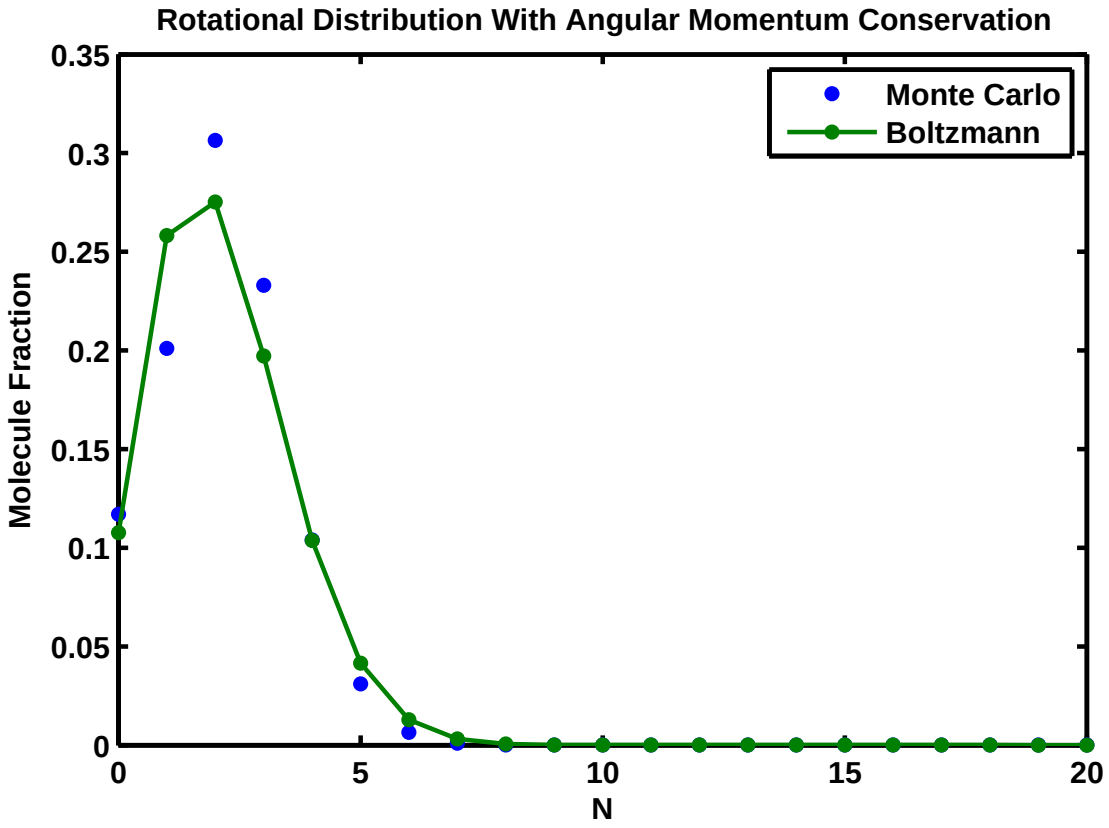

Figure A3: Simulation of rotational distribution. Blue dots are derived from simulation using density of states and conservation of to assign probabilities for changes in rotation level. Green dots indicate the Boltzmann distribution at 4 K.

Appendix 2

Beam Source Machine Drawings

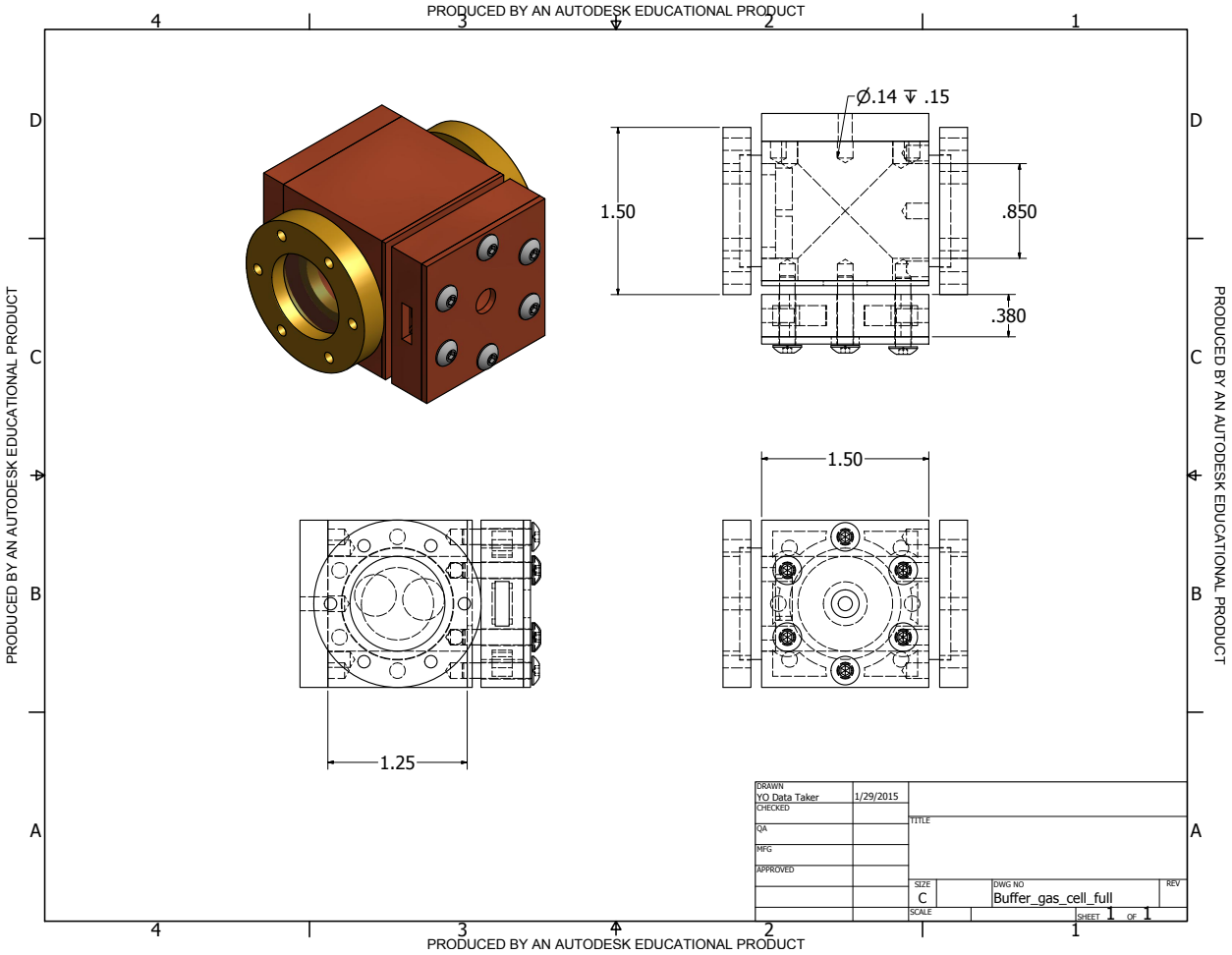

Figure A4: Machine drawing of 2 stage cell. Diameters of 1st stage aperture is 3 mm and aperture diameter of the slower stage is 9 mm.

	Area	$Transmission$	Effective Area
Aperture	$\pi \times \frac{9mm}{2}^2 = 0.64cm^2$	0.3	0.19 cm^2
Gap	4×1.25 inch×2.5 mm	1	3.81 cm^2
Side Vents	0.42 inch×0.1 inch×2	0.4	0.216 cm^2

Table A1: Table of effective leak areas of the second stage cell

Appendix 3

Electronic Schematics

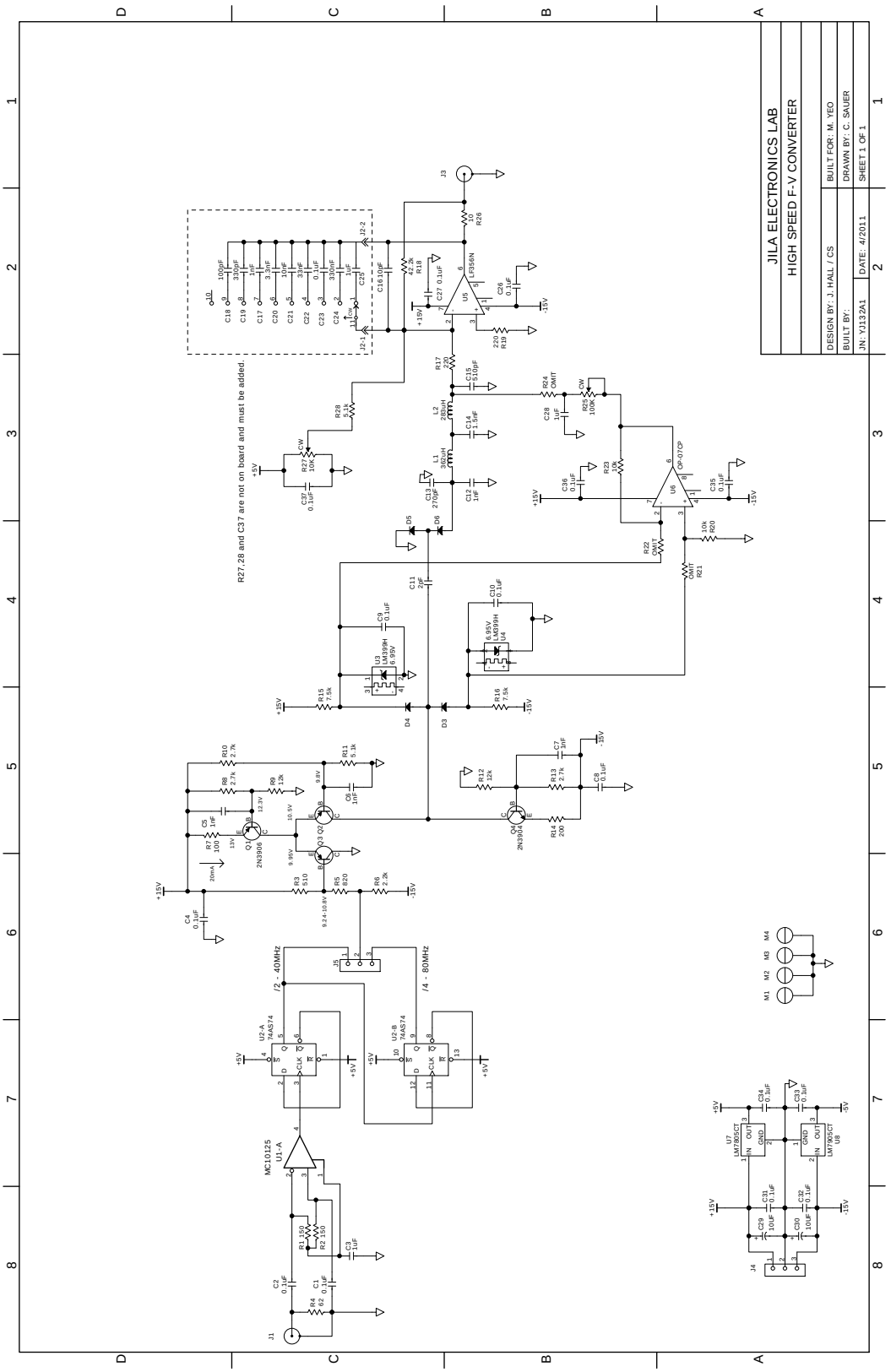

Figure A5: Electronic schematic of frequency to voltage convertor.